The effect of kite control unit mass and drag on the flight behavior of an airborne wind energy system kite

X.G. Gerrmann

Technische Universiteit Delft

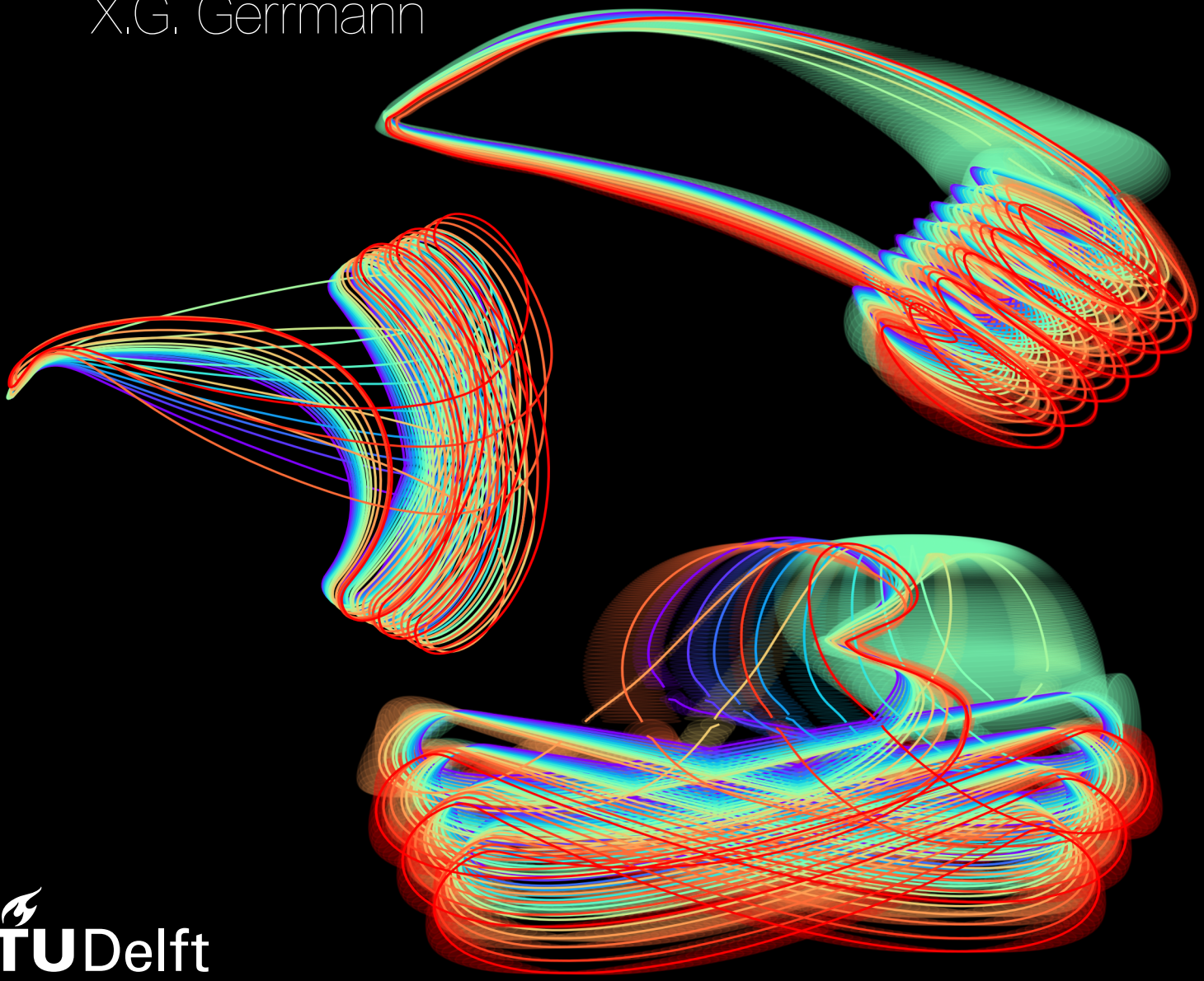

TU Delft

The effect of kite control unit mass and drag on the flight behavior of an airborne wind energy system kite

by

X.G. Gerrmann

to obtain the degree of Master of Science

at the Delft University of Technology,

to be defended publicly on Monday September 23, 2019 at 13:00 PM.

Student number:	4139186	
Project duration:	October 1, 2018 – September 23, 2019	
Thesis committee:	Prof. dr.ing. J.W. van Wingerden	Faculty of 3mE
	Dr. ing. S. Baldi,	Faculty of 3mE
	Dr. ing. R. Schmehl,	Faculty of Aerospace Engineering
	S. Rapp,	Faculty of Aerospace Engineering

This report is confidential and cannot be made public until September 23, 2021.

TU Delft

DCSC

Abstract

Airborne wind energy (AWE) is an emerging field that aims to revolutionize the wind energy sector. This work focuses on the aspects of modeling AWE kite flight behavior. Research on such models is important since new or improved models can potentially reduce development time and costs and provide insight in the role of key system parameters.

This research investigates the effects of the mass and drag of the kite control unit (KCU) on the kite's flight behavior since it is hypothesized that the mass of the KCU causes an outward swing of the KCU during turns and that KCU drag reduces the angle of attack during the retraction phase.

For this investigation, the simulation of a kite and tether system is required. Existing simulation environments could not be used due to legacy code, limited validity or unsuitable model complexity. Therefore, a suitable kite and tether model need to be selected for implementation in a simulation environment (SE). Two kite models have been found suitable: Fechner's and Ruppert's model.

In the early stages of this research the aim was to use a model that has been fitted to experimental flight data. Due to the unavailability of experimental flight data, the parameters of both models are identified using simulated flight data. This approach provides Kitepower with a method to identify the model parameters with experimental flight data in the future. Kitepower is an AWE company that facilitated on this research.

The groundstation controller and flight controller signals of Kitepower have been integrated in the SE. Two experiments have been performed in the SE. For the first experiment, flights are performed with different and increasing values for the drag coefficient of the KCU. In the second experiment the mass of the KCU and kite have been varied independently. Both experiments have been performed in a low and high wind condition.

The high wind condition experiment showed that and increasing drag results in a reduction of 7% of the average cycle power. The KCU drag force can reach up to to 5% of the kite drag force for a KCU drag coefficient of 1.5.

Increasing the combined mass of the kite and KCU results in an increase of >150% in average cycle power output for the low wind conditions and an increase of >40% for the high wind condition. The increase in power is caused by a reduction in elevation angle in combination with the assumption of a flat wind profile. Additionally an outward swing of the KCU of 4.5° has been observed.

It is recommended to compare Fechner's and Ruppert's rigid body kite models through using experimental flight data in order to investigate which model reproduces actual kite flight the best. Furthermore it is recommended to investigate the optimal altitude or elevation angle at which to operate the AWE system for maximal power output considering a non-flat wind profile, tether drag and kite and KCU dynamics. It is suggested that these findings should then be incorporated in the flight controller of Kitepower in order to increase the system power output.

Contents

List of Figures

List of Tables

1

Introduction

Airborne wind energy (AWE) is a relatively new concept from 1980 [63] for harvesting energy from a renewable energy source. One of the leading companies in AWE a start-up called Kitepower. Kitepower's ground-based AWE system consist of three components, namely a generator on the ground, a tether and a flexible kite. Through flying patterns with the kite the generator on the ground is able to convert the mechanical energy into electrical energy.

Due to their flexibility, these kites are more difficult to model than regular rigid aircraft. Research showed that the dynamics of the kite control unit (KCU) influence the roll and pitch of the kite which consequentially influences the turning behavior. The tether further complicates the modeling of these systems. Only a few models have been verified with experimental flight data.

Regarding the steering of leading edge inflatable kites (LEI) kites, the steering is thought to be caused by a warping induced yaw [84]. It is hypothesized that kite roll caused by the outward motion of the KCU due to centrifugal forces positively contribute to the steering. Additionally, it has been observed in experimental flights that added drag induced by an on-board turbine reduces the angle of attack of the kite. The aerodynamic drag of the KCU might play a role in the hypothesized outward motion as well.

Oftentimes the mass of the KCU is not taken into account when modeling these AWE systems, whereas some models include the mass, but ignore aerodynamic drag. Reports exists of models that show correspondence of the model including KCU mass with experimental flight data, but no reports exist that explicitly quantify the effects of the mass and drag of the KCU.

In this research the effects of the mass and drag of the KCU on the kite's behavior during flight will be investigated. Since the kite behavior is heavily linked with the dynamics of the tether and groundstation as well as the flight and groundstation controller, the overall system behavior is analyzed.

For a controlled investigation, simulation of a complete airborne wind energy system will be required. Existing simulation environments cannot be used for several reasons. Therefore a suitable kite and tether model need to be selected for the implementation in a real-time simulation environment, using a dynamics engine.

After a model selection and verification step, a set of experiments have been performed in the simulation environment under different wind conditions where the mass and drag of the kite were manipulated. The experiments are followed by a summary of the findings and recommendations for further research and a set of suggested actions for Kitepower.

2

Literature Review

The literature review contains a summary of all the required background knowledge for the actual thesis work. It contains an overview of the state-of-the art in the modeling of AWE systems. The literature review starts with the basics of AWE systems and gradually shifts its focus towards the modeling and simulation of these systems. It provides an extensive overview of different kite and tether models. The result of the literature review is the research question which is discussed in the following chapter.

2.1. AWE Preliminaries

In this section the AWE basics will be laid out, starting with the extractable wind energy. Different concepts and methods for converting wind energy to mechanical or electrical energy will be discussed. Finally the system of Kitepower will be discussed in detail.

2.1.1. Increasing Extractable Wind Power with Higher Altitudes

Here, the relation between extractable energy and wind speed will be discussed, followed by the effect of altitude on the amount of extractable energy.

The wind power P_w scales cubically with the wind speed. However, the extractable power P_{ex} is not equal to wind power P_w . The ratio between the extracted power and the wind power is equal to the power coefficient C_p, which has an analytical limit of:

$$C_{p,max} = \left(\frac{P_{ex}}{P_w}\right)_{max} = 16/27 \tag{2.1}$$

This limit is often referred to as the Betz limit [59] [66]. Since C_p is a scalar, the extractable power from the wind scales also with the cube of the wind speed.

$$P_{ex} = C_p \delta_w S_\perp \tag{2.2}$$

$$\delta_w = 1/2 \rho v_w^3 \tag{2.3}$$

δ_w = Wind power density
$S_\perp$ = Surface area perpendicular to the wind velocity
v_w = Wind velocity
ρ = Density of the air

The power density δ_w is a useful measure since it contains the wind speed and the air density which directly influence the power generation. Both are dependent on the atmospheric conditions which varies

greatly with altitude. Therefore the relation between altitude, air density and wind speed will now be inspected.

The Hellmann exponential law (Equation 2.4), or power law, is a commonly used expression for the relation between wind speeds at different heights [18] [10]. The relation makes use of a parameter α which depends on the site's topography (Table B.1) and can also vary between day and night [18]. For the estimation of v at height H, one wind speed measurement v_0 is required. The measurement of v_0 is generally performed at a height of $H_0 = 10$ [m].

$$\frac{v}{v_0} = \left(\frac{H}{H_0}\right)^{\alpha} \tag{2.4}$$

One could also use the logarithmic wind profile law (Equation 2.5) [49][18], which makes use of a surface roughness parameter z_0 (Table B.2). Here H is the height with respect to the height at which zero wind speed occurs. It should be noted that from 100m and up, the the power law is more accurate than the logarithmic law [25].

$$\frac{v}{v_0} = \frac{\ln(H/z_0)}{\ln(H_0/z_0)} \tag{2.5}$$

The density of air depends on pressure and temperature. Both pressure and temperature vary with altitude. Equation 2.6 shows the (near-linear) relation of the air density with the altitude [10], incorporating varying pressure and temperature.

$$\rho(z) = \frac{p_0}{RT_0}\left(\frac{T_0 - \Gamma z}{T_0}\right)^{\left(\frac{g}{\Gamma R} - 1\right)} \tag{2.6}$$

g = Gravitational constant
R = Gas constant
p_0 = Pressure at sea level
T_0 = Temperature at sea level
Γ = Lapse rate ([K/km])

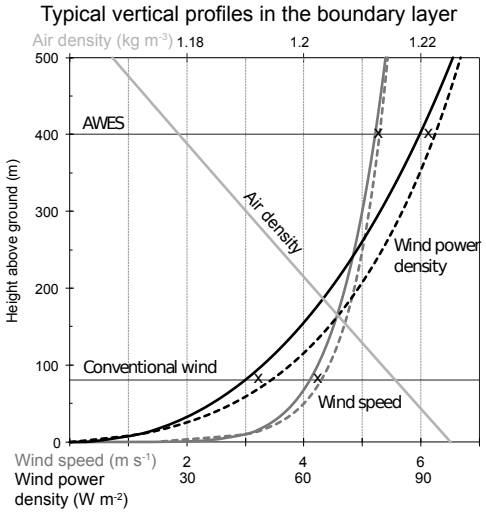

Figure 2.1: Relation between altitude, air density, wind speed and the resulting wind power density, using the poser law (solid) and the logarithmic law (dashed). Adopted from [10].

Figure 2.1 shows the combined effect of varying air density and wind speed on the wind power density. Both wind speed profile laws are shown. The typical altitude of AWE systems is also indicated (400 [m]). The increasing wind power density at greater heights is one of the biggest motivations for the development of AWE systems.

2.1.2. An Overview of Existing AWE Systems and Concepts

Here an overview will be given of several AWE concepts. The goal is not to give a complete overview, but to provide the reader several examples to build an understanding of the possibilities of AWE. Ground generation, airborne generation and vehicle propulsion applications will be discussed.

Each AWE concept consists of at least the following three components (Figure 2.2).

- An anchor point
- A tether
- An aircraft

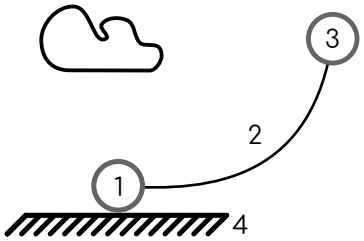

Figure 2.2: Depiction the main components of AWE systems. 1) Anchor point, 2) Tether, 3) Aircraft, 4) Earth's surface.

Ground-Based Generation Ground-based generation encompasses all systems with the generator located on or near the surface of the earth, including floating systems [24]. In general this means a generator is connected to a drum around which the tether is wound to which an aircraft provides tension. During reel out the generator provides a counter torque such that energy can be extracted, this mode of operation is called traction. Power generation is performed in pumping cycles (Figure 2.5), due to the limited length of the tether. Reeling out and in are alternated, making sure that reel out generates more energy than reel in costs. The pumping cycle operation will be discussed in subsection 2.1.3.

Throughout the traction phase the kite can either perform static or crosswind flight. During static flight, the kite faces the wind. During crosswind flight the kite flies a path transverse to the wind, this will increase the kite's airspeed to above the wind speed. Figure 2.6 shows that crosswind flight results in a higher power output.

Airborne Generation With airborne generation, the conversion from wind energy to electrical energy takes place on the aircraft. The electrical energy is then transported via the a cable to the ground. Figure 2.3 shows three examples of airborne generation systems. This category of systems is often referred to as fly-gen [88]. The leftmost aircraft in Figure 2.3, can generate power in two ways similarly

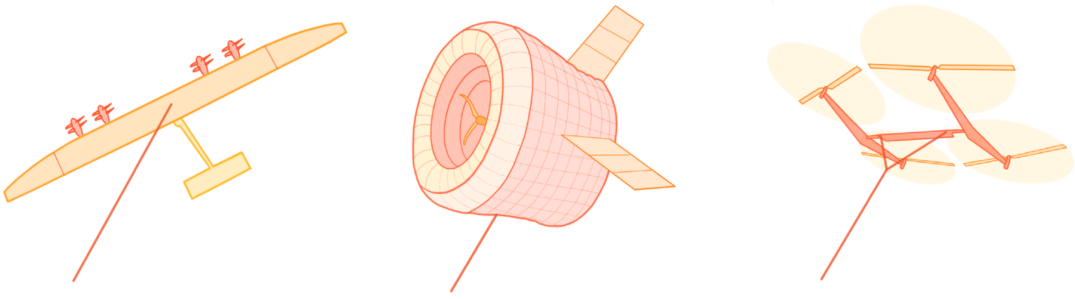

Figure 2.3: Different concepts for airbone generation [23]. Left: Plane with front-facing turbines. Middle: Lighter-than-air aircraft with a wind turbine in center. Right: A quadrotor with autorotation.

to ground-based generation, namely through static and crosswind flight.

Vehicle Propulsion In some cases like carriage (Figure 2.4a) or ship propulsion (Figure 2.4b) [71] the energy is not required to be converted to electricity, but serves to provide or assist in the motion of an object. Concepts for the propulsion of railway vehicles also exist [6].

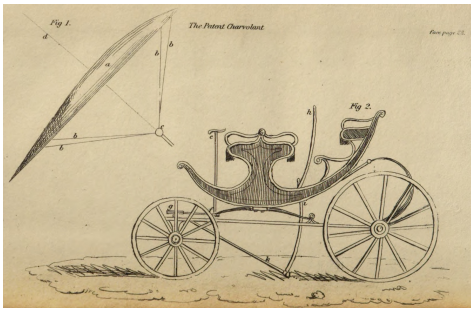

(a) Depiction of a kite propelled carriage [100]

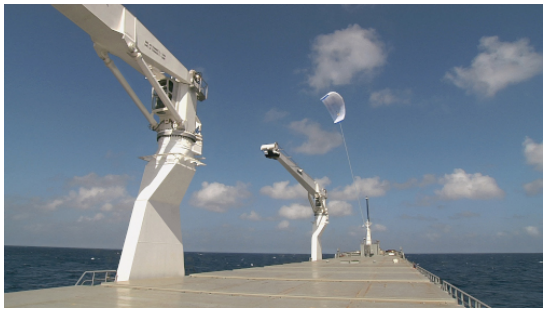

(b) Kite assisting in ship propulsion [3].

Figure 2.4: Two different uses of a kite for vehicle propulsion

2.1.3. Description of the Working Principles of Pumping Cycle AWE Systems

The basic working principles of pumping cycle AWE systems, especially the one that is employed by Kitepower, will now be explained.

Just like all other AWE systems, the pumping cycle system consists of a anchor point, a tether and an aircraft. As described in Figure 2.1.2 this system generates energy by alternating between a reel-out and a reel-in phase, alternatively named the traction and retraction phase as shown in Figure 2.5. Figure 2.6 shows that the power output is greatest when the aircraft flies in crosswind conditions, therefore the aircraft is flown in closed loops which resemble a figure of eight Figure 2.5a. The traction and retraction phases are alternated. A third phase, the transition phase, describes the transition from the retraction phase to the traction phase. The retraction phase costs energy and the traction phase produces energy (Figure 2.5b). The aircraft and the flight paths will be discussed next, the ground station falls outside the scope.

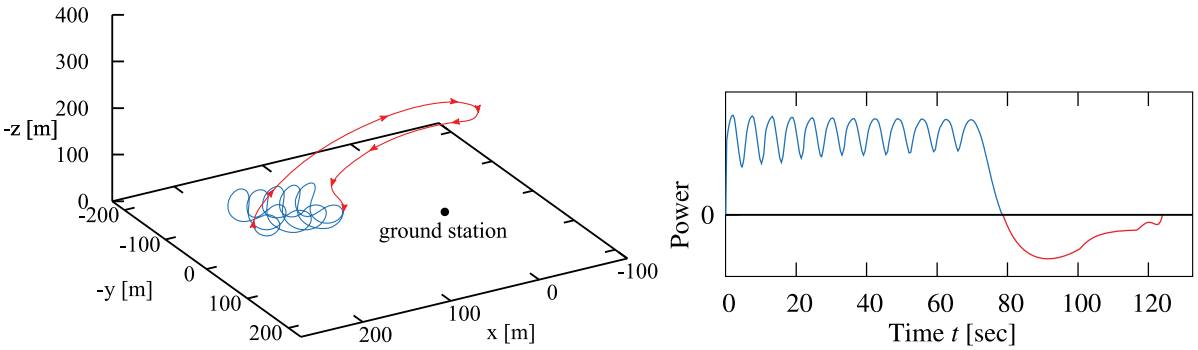

(a) The traction (blue) and retraction (red) phase as a closed path. Adapted from [35]

(b) Global system enery output. Blue = traction phase, red = retraction phase. Adapted from [35].

Figure 2.5: Distinction between the traction and retraction phases and the trajectory of an aircraft over one pumping cycle.

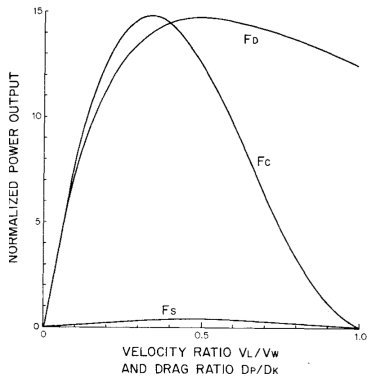

Figure 2.6: Effect of velocity and drag ratio on the system power output for $L/D_K = 10$. D_F: airborne generation with crosswind flight, F_C: ground-based generation with crosswind flight, F_S groundbased generation with static flight [63].

Aircraft Types and Control Methods Different types of aircraft can be used for the operation of such systems. Encountered aircraft are [23]:

- LEI SLE (Leading Edge Inflatable, Supported Leading Edge) kites;
- LEI C-kites;
- Foil kites;
- Glider or rigid wing;
- Swept rigid wings;
- Hybrids / Semi-rigid wings.

Since Kitepower current system is operated with LEI-SLE kites, this will be referred to as kite, or LEI kite. For this type of kite, different steering mechanisms can be used:

- Control of the bridle from the ground;
- Control of the bridle from an airborne control unit;
- Control of a cart on a rail attached to the wingtips of a kite;
- Control through the actuation of aerodynamic surfaces.

Kitepower makes use of an airborne control unit to control the kite. This control unit is called the kite control unit (KCU). The KCU is located inbetween the kite and the ground station, where the tether connects the KCU with the ground station and the bridle, steering and power lines connects it with the kite (Figure 2.7a). The KCU can reel in and reel out the steering power lines. Shortening the length of the steering lines on either side causes the kite to warp and consequently to steer. The power lines give the KCU control of the power setting of the kite (Figure 2.7b).

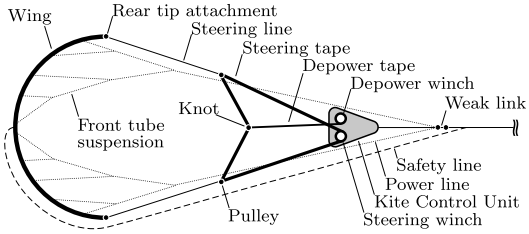

(a) Line layout of the kite and KCU.

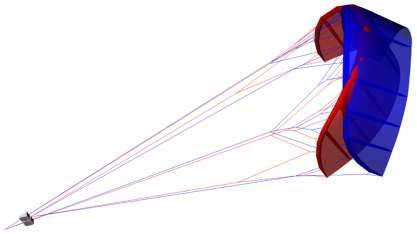

(b) Kite orientation with respect to the KCU for different power settings.

Figure 2.7: KCU kite and bridle layout and effect of power setting. Adopted from [56].

Aircraft Flight Path Shape and Definition Details regarding the flight path of the kite will be discussed here. A different view of the flight path is shown in Figure 2.8. It is the KCU's task to steer the kite in such a way that roughly the same trajectory is flown. The way Kitepower has implemented the flight path controller is through the use of attractor and turning waypoints.

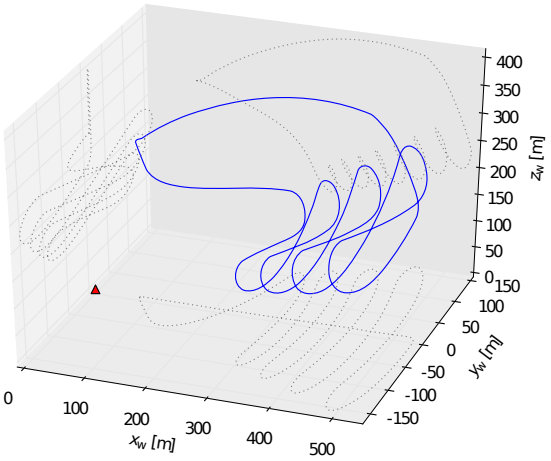

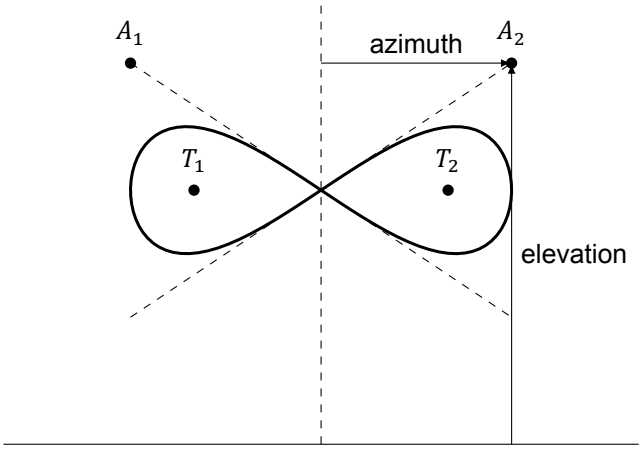

Figure 2.8: Left: Flight path in 3D, adapted from [37]. Right: projection of the flight path in 2D.

Waypoints are a way to influence the movement of the kite. The waypoints are part of the user input and correspond to a set of parameters and switching conditions. There are two types of waypoints, each with a different set of parameters: "Attractor" (A_*), and " Turn" (T_*). When flying the figure-of-eights, the aircraft intermittently switches between the "Attractor" and "Turn" waypoint types. The lying eight can be constructed by two small and two large circle segments. The "turn" waypoint causes the aircraft to execute a turn either up or downward. The "attractor" causes the aircraft to fly towards a specific point,

resulting in a straight trajectory. The attractor waypoint knows two parameters that define its location, the turn waypoint knows only a steering value; together these determine the flight path as can be seen in Figure 2.8. As mentioned, a switch occurs between different waypoints (which are not necessarily of a different type). A switch is determined by a conditions on e.g. altitude and azimuth. This causes the aircraft to fly from turn 1 → attractor 1 → turn 2 → attractor 1 → turn 1 → and so on.

2.2. Modeling and Simulation Practices in AWE

This section inspects the modeling aspects of AWE systems, starting with the use cases. An extensive model overview for kite and tether models will be given. The final section will provide an overview of existing and possible future software for the simulation of AWE systems.

2.2.1. The Use of Modeling and Simulation for AWE

Reasons for modeling AWE systems can be (among others):

- Estimation of the LCOE[1] [80]
- Flight controller design and trajectory optimization [50] [32]
- Kite design [21] and structural optimization [11]
- System component design
- Model validation [98] [14] [45]
- Serve as a substitute for direct measurement and experimentation

Depending on the use, models with different levels of detail exists. For example, for the estimation of the LCOE, the actual flight path is irrelevant and a kite position is used which is representative for the 'average' location in a figure-of-eight during reel out. In this case the level of detail is quite low. In the following two sections, different kite and tether models will be discussed. Ground station models are excluded.

2.2.2. The Different Types of Kite Models

Below, the reader is provided a list of different kite models that are being/ have been used. The models will be discussed roughly in the order of model complexity. Dynamical, aerodynamic and structural models are discussed intermixedly since they rely on shared assumptions.

The following model types will be discussed:

- Black box models
- Point mass models
- Rigid body models (+ reduced and extended versions)
- Multibody models
- Multi-plate models
- Lumped-mass / particle models
- Finite element method (FEM) models

The model types can be ranked by their degrees of freedom and the computational effort, resulting in Figure 2.9.

Black-/Gray-Box Kite Models In black-box or gray-box models a direct mapping between input and output is constructed. Black-box models do not assume any knowledge about the system, whereas grey-box models knowledge is included. In [34], [55] and [84] a relation is used between the steering input and the yaw rate which agrees very well with experimental data. This relation is often referred to as the turn-rate law.

[1] Levelized Cost of Energy: the net present value of the unit cost of electricity over the lifetime of a generating asset.

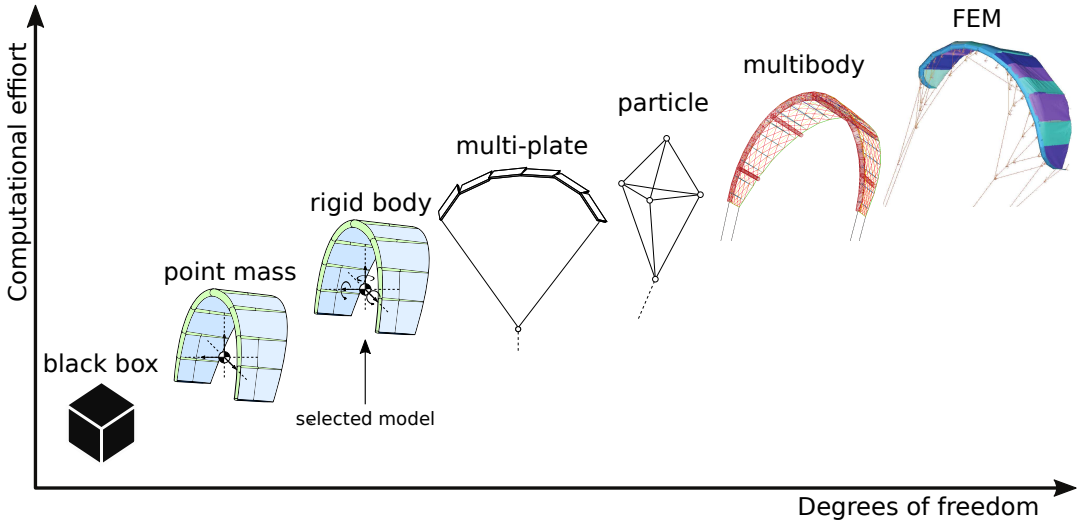

Figure 2.9: Qualitatively increasing computational effort with degrees of freedom / model complexity. The model type that is eventually selected and used is indicated with an arrow.

Point Mass Kite Models Point mass models have translational dynamics (thus translational inertial effects), but ignore rotational dynamics and therefore have instant attitude changes. Flexibility is ignored. During flight, in general it is assumed that the kite is always aligned with the apparent wind, however in [14] the sideslip is virtually imposed by a control variable.

Gravitational, aerodynamic and tether forces act on the kite. Depending on the tether model, the tether gravity and drag is incorporated in the equations of motion. Steering is achieved by an aerodynamic side-force or prescribing a roll angle to the lift vector. Both the roll and aerodynamic side force depend linearly on the steering input. See Table 2.1 for an overview of different implementations.

Besides the different steering methods, different implementation of the aerodynamic forces are used. More about this in section 2.3.

This model (depending on the implementation) can become unstable when the mass hanging underneath the kite is too low [14], or when the tether force are low [38]. The absence of rotational inertia causes sign changes of the apparent wind and consequentyl jumping of the yaw angle, which is non-physical behavior. Also, it is less accurate than the four-point model [38], which will be discussed in Figure 2.2.2.

Besides information regarding the kite model, [15] contains information regarding the simulation of multiple models. Two options are explained: 1) Model exchange, and 2) Co-simulation. Model exchange results in an extended state vector containing states of both models and thus a quadratically growing system matrix with the number of states. Co-simulation separates the simulation of both models and ensures interaction at specified time-intervals.

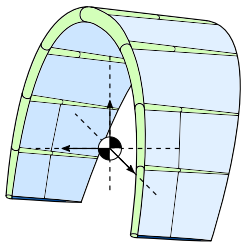

Figure 2.10: A point mass kite model with 3 translational DOF

The point mass model is often used in analytical analyses of AWE systems. In the analytical case quasi-steady motion of the kite is assumed through an equilibrium between the aerodynamic forces and the tether force.

Table 2.1: An overview of the encountered variations of the point mass model.α = angle of attack; β= sideslip or an arbitrary control variable; ψ = roll; C_L, C_D, and C_S are the respective lift, drag and steering coefficients; k is a constant.

Source	Aerodynamic	Control
[36]	$C_L(\alpha)$, $C_D(\alpha)$	ψ
[31], [32], [52]	$C_L = k_L$, $C_D = k_D$	ψ
[107],[108]	$C_L = k_L$, $C_D = k_D$	α, ψ
[109]	$C_L(\alpha) = k\alpha$, $C_D = C_{D_0} + kC_L{}^2$	α, ψ
[13]	$C_L(\alpha)$, $C_D = C_{D_0} + kC_L^2$, $C_s(\beta) = C_L(\beta)$	α, β
[53],[50],[54]	C_L, $C_D = C_{D,0} + kC_L^2$	ψ, C_L
[14]	$C_L(\alpha)$, $C_D = C_{D,0} + kC_L^2$, $C_S(\beta)$	α, β
[101]	$C_L = C_{L_0} + C_{L_\alpha}\alpha$,$C_D = C_{D,0} + kC_L^2$	α, ψ
[38]	$C_L(\alpha)$, $C_D(\alpha)$, $C_s(\beta)$	α, β
[16]	$C_L(\alpha)$, $C_D(\alpha)$, $C_s(u)$	α, u

For a basic quasi-steady analysis, the following assumptions are made:

- Quasi-steady flight: the flight manoeuvre can be approximated as a sequence of steady state changes.
- No gravitational and inertial forces
- The aerodynamic coefficients (C_L and C_D) are fixed.
- The tether is straight →The reel-out velocity is aligned with the tether
- Tether weight and (aero)dynamics are neglected

Using an analytic model, in his paper [63], Loyd performs a 2D analysis for different flight scenarios of a kite, including non-manoeuvring (simple-kite) and crosswind flight. The optimal reel-out velocity for maximum power generation during reel-out has been determined analytically and is found to be $v_L/v_w = 1/3$. Furthermore, it is shown that the L/D ratio has a significant influence on the power output of the system. Additionally an advanced analysis has been performed, which makes use of a point-mass model (Figure 2.2.2).

The two dimensional analytic analysis can be extended to three dimensions by using a spherical coordinate system ([5, p.28] [73] [97]), using coordinates r, θ and ϕ for the position and ϕ for the heading of the kite. Since the apparent wind velocity cannot be negative, this approach leads to a constraint on the reeling factor: $f \leq S_\theta C_\phi$. Furthermore, a direct relation is found between the aircraft flight velocity and the wind velocity, captured by the tangential velocity factor λ. Due to the nature of λ, it cannot be negative which results in set of ϕ_{max} and θ_{max} that together define a subset of the flight envelope. For the flight envelope the following definition will be held: "The set of possible positions in space of a kite, attached to a tow line with length r, is described by a quarter sphere with radius r, which is called the flight envelope (FE)" [71].

More detailed versions of the analytic model include gravitational and inertial forces. Nevertheless, inertial forces are deemed relevant only for situations with high angular velocities which occur when the tether is short. During nominal flight the tether length is significant and therefore the inertia can be ignored [97]. Figure 2.11 shows the relevant forces and velocities for the scenario where the gravitational force is included and inertia is ignored.

As stated before, the model depends on a force equilibrium. The resulting set of equations are nonlinear in the unknown parameters. An algebraic solution cannot be found even though there are six equations and six unknowns.

Two numerical methods exist for solving the set of equations. One makes use of the discrepancy between the the lift-over-drag ratio and the kinematic ratio [97]. The other method makes use of Newton's iterative method, which takes roughly 5 iterations to converge Figure 2.12. The number of iterations required for the method of [97] is not analyzed.

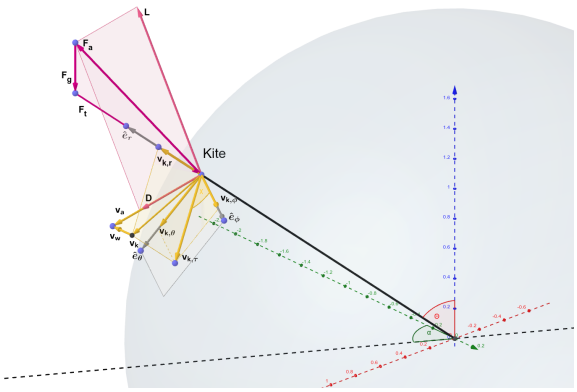

Figure 2.11: Kite force and velocity diagrams in 3D. Forces are shown in pink, velocities in yellow.

$$-f_t + 1/2\rho S|\mathbf{v}_a|^2(C_L e_{L,1} + C_D v_{a,1}|\mathbf{v}_a|^{-1}) - C_\theta mg = 0 \tag{2.7}$$

$$1/2\rho S|\mathbf{v}_a|^2(C_L e_{L,2} + C_D v_{a,2}|\mathbf{v}_a|^{-1}) + S_\theta mg = 0 \tag{2.8}$$

$$1/2\rho S|\mathbf{v}_a|^2(C_L e_{L,3} + C_D v_{a,3}|\mathbf{v}_a|^{-1}) = 0 \tag{2.9}$$

$$\mathbf{e}_L \cdot \mathbf{e}_a = 0 \tag{2.10}$$

$$|\mathbf{e}_L| = 1 \tag{2.11}$$

$$v_{k,\theta} = v_{k,\phi} \tan^{-1}(\chi) \tag{2.12}$$

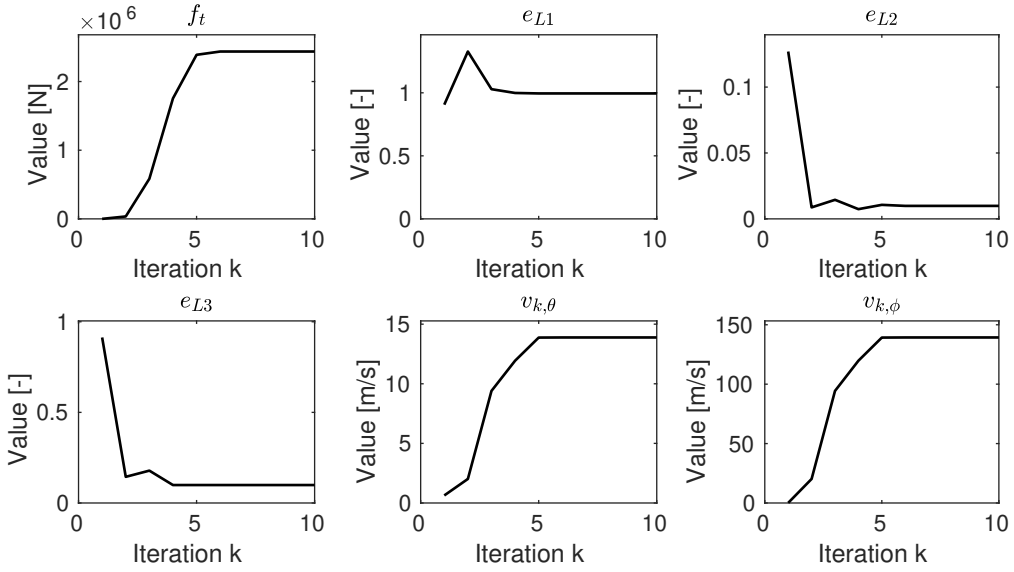

Figure 2.12: Convergence of the solution estimates via the Newton approach

For simulation, the analytic point mass model can be used in two ways: 1) The position of the kite is updated with each time step by using the resulting velocities from the equilibrium for a given heading and location, 2) At each time step the kite is moved only in the radial direction. A representative kite location and heading are chosen such that the output power corresponds to the average power of that in the first method. Steering occurs by either prescribing the heading or the roll angle.

Rigid Body Kite Models This is the model that is eventually selectect in the following chapters. Just like the previous two models (generally) rigid body models neglects deformations. Whereas the orientation has been neglected previously, the attitude dynamics for this type of models are now taken

into account through rotational inertia and torques. Rigid body models are often used for modeling aircrafts [69] [58]. A flexible aircraft has also been modeled as a rigid body [95]. For rigid body models, results rely heavily on the correct modeling of the aerodynamic forces.

[15] uses a rigid body model in combination with a panel method for determining the aerodynamic forces. [60] uses an aerodynamic model by using non-dimensional aerodynamic coefficients. Quaternions are used to prevent singularities.

Reduced rigid-body kite models, or semi-rigid body kite models [84], fix certain degrees of freedom or prescribe an analytical constraint (possibly controlled). Extended rigid body models, in general, try to capture the flexibility or deformability of a kite.

In [84] a reduced rigid body model is used, this model will be referred to as Ruppert's model from here on. The motivation for this is that the kite is largely constrained in two degrees of freedom, namely roll and pitch, this will result in stiff differential equations. Therefore the roll is constrained such that the kite is always perpendicular to the tether. The kite's pitch (angle with respect to the tether) is controlled by the power setting P_s, which is used as a control variable. For steering two methods are used: 1) A direct coupling between the steering input and the yaw rate (thus ignoring rotational inertia), and 2) a yaw rate depending on the aerodynamic torques. A comparison between both steering methods has not been performed.

[45] extends the rigid body model with variable mean chord length, wing span, surface area and inertia properties, all depending on the control inputs. The relations are all quasi-static, so no additional dynamics are introduced.

[95] Uses rigid body dynamics for modeling in order to inspect the stability of a non-controlled kiteplane. The aerodynamic elements are discretized and offset from the center of mass (Figure 2.21).

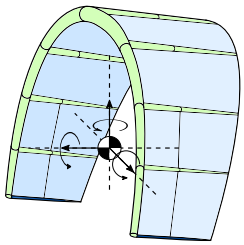

Figure 2.13: A rigid body model with 6 DOF: 3 translational and 3 rotational

Particle Kite Models Particle, lumped-mass or multi-point models are characterized by multiple interconnected point masses. The connections can either be flexible or fixed. One motivation for using a particle-based method is to allow for different kite designs, as well as to be able to anticipate specific defects. A particle model representation has also been used for modeling a flexible aircraft in [57]. In [39] the kite is modeled by two semicircular arcs containing 5 particles each (Figure 2.14, left). Infinitely stiff springs are used for the connections. Additional connections are placed between the particles on the front side to force the kite shape. All constraints are forced one-way. A velocity-free Verlet [99] integration method is used for simulation and an iteration is used for handling the constraints. The Verlet integration method is fast and more stable then the Euler integration scheme [99]. By limiting the number of iterations on the constraints, still some flexibility is allowed which allows more flexibility in the trailing edge. The aerodynamic coefficients are determined by slicing the canopy midway of the particles and determining the angle of attack of each slice. The aerodynamic coefficients are then used to obtain the aerodynamical forces which are distributed equally over the surrounding particles.

The particle model developed in [62] consists of five particles (but is called the 'four-point kite model') and will be referred to as Fechner's model from here on. Besides gravity and constraint (spring) forces, particles 0,1 and 2 experience aerodynamic forces based on a common $C_L(\alpha)$ and $C_D(\alpha)$ curve. The model is shown in Figure 2.14 on the right, note that this image is a projection and that the particles do not actually lie in the same plane.

Table 2.2: An overview of the encountered variations of the rigid body mass model. P_p, P_s are the power and steering inputs respectively, u is an input that causes a mesh deformation, x_{ba_L}, x_{ba_R} are the displacements of the left and right control carts respectively, the same goes for δ_L, δ_R.

Source	Aerodynamic	Control
[84]	$C_X = C_D(\alpha)$ $C_Y = \frac{A_{side}}{A_{kite}} C_\beta \beta$ $C_Z = C_L(\alpha)$ $C_n = C_{n_{\alpha(P_s)}} \alpha(P_s) + C_{n_\beta}\beta + C_{n_r}\frac{br}{\lvert V_{app}\rvert} + C_{n_d}\frac{2F_{g,y}}{\rho_{air}A_{kite}b\lvert V_{app}\rvert^2}$	P_p, P_s
[15]	Panel method	u
[45]	$C_X = C_{X_0} + C_{X_\alpha}\alpha + C_{X_X}\frac{\hat{x}_{ba}}{\bar{c}}$ $C_Y = C_{Y_\beta}\beta + C_{Y_{\dot\beta}}\dot\beta + C_{Y_r}\frac{rb}{2V_a} + C_{Y_{x_L}}\frac{\hat{x}_{baL}}{b} + C_{Y_{x_R}}\frac{\hat{x}_{baR}}{b}$ $C_Z = C_{Z_0} + C_{Z_\alpha}\alpha + C_{Z_q}\frac{q\bar{c}}{V_a} + C_{Z_x}\frac{\hat{x}_{ba}}{\bar{c}}$ $C_l = C_{l_\beta}\beta + C_{l_r}\frac{rb}{2V_a} + C_{l_{x_L}}\frac{\hat{x}_{baL}}{b} + C_{l_{x_R}}\frac{\hat{x}_{baR}}{b}$ $C_m = C_{m_0} + C_{m_\alpha}\alpha + C_{m_q}\frac{q\bar{c}}{V_a} + C_{m_x}\frac{\hat{x}_{ba}}{\bar{c}}$ $C_n = C_{n_\beta}\beta + C_{n_r}\frac{rb}{2V_a} + C_{n_{x_L}}\frac{\hat{x}_{baL}}{b} + C_{n_{x_R}}\frac{\hat{x}_{baR}}{b}$ Structural model: $\bar{c} = f_{\bar{c}}(x_{ba}), b = f_b(x_{ba}), S = f_S(x_{ba})$	x_{ba_L}, x_{ba_R}
[60]	$C_X = C_D\cos\alpha - C_L\sin\alpha$ $C_Z = C_L\cos\alpha + C_D\sin\alpha$ $C_Y = 0$ $C_l = C_{l_0} + C_{l_\beta}\beta + C_{l_p}\frac{w_x b}{2\lvert v_{rel}\rvert} + C_{l_r}\frac{w_z b}{2\lvert v_{rel}\rvert} + C_{l_\delta}(\delta_R - \delta_L)$ $C_m = C_{m_0} + C_{m_\alpha}\alpha + C_{m_q}\frac{w_y\bar{c}}{2\lvert v_{rel}\rvert} + C_{m_\delta}(0.5(\delta_L + \delta_R) - \delta_{ac})$ $C_n = C_{n_0} + C_{n_\beta}\beta + C_{n_p}\frac{w_x b}{2\lvert v_{rel}\rvert} + C_{n_r}\frac{w_z b}{2\lvert v_{rel}\rvert} + C_{n_\delta}(\delta_R - \delta_L)$	δ_L, δ_R
[95]	Aerodynamic element discretization, per element: $C_X = C_D(\alpha)$ $C_Y = 0$ $C_Z = C_L(\alpha)$ $C_l = 0$ $C_m = f(\alpha)$ $C_n = 0$	-

A similar particle model consisting of 4 particles is used in [38]. A model with four particles is the most simple particle-system model that includes rotational inertia in all axes. Kite mass is distributed over the particles. A fifth particle represents the kite control unit. Particles are interconnected with spring-damper elements (Figure 2.14, right). The virtual kite center is midway between points C and D. The kite shape is parametrized by three values hk, hb and wk. Only steering sensitivity parameters need to be identified. The aerodynamic forces are applied to surfaces that are attached to the kite particles **B**, **C** and **D** in the same way as [62]. No surface is attached to point A, this point only serves the correct placement of the COG and contributes to the rotational inertia.

A Multibody Kite Model Whereas particle models consist of a set of point masses, multibody models consist of a collection of rigid bodies connected by constraints. A multibody approach is used in [21] in order to model a kite. The kite is build up from two 'building blocks': 1) Inflatable tubes consisting of series of rigid bodies connected by spherical joints with rotational stiffness in all three directions, and 2) foils consisting of cord-wise wires, trailing wires and cross wires. desktop.

Multi-Plate Kite Models Multi-plate models consist of multiple plates connected by hinges. The multi-plate models can be considered very elementary multibody models Figure 2.2.2. The hinges can either

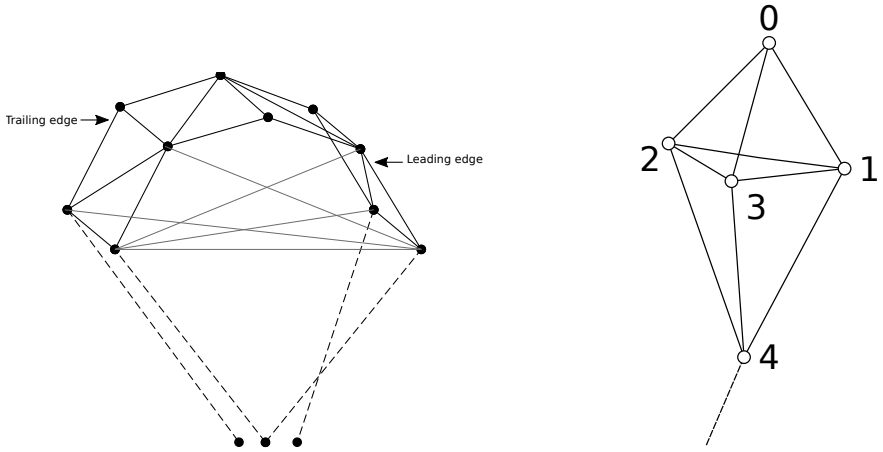

Figure 2.14: Different particle model implementations of a kite. [39] (left), [38] and [62] (right)

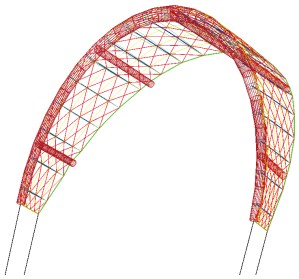

Figure 2.15: Wireframe of the multibody model [21].

be frictionless [105] or consist of spring and damper elements[98] to provide stiffness and damping. Two types of models exist in the literature, namely a multi-plate model starting with 2 plates [105] [60] and a 3-plate modell [98]. Steering is achieved by changing the bridle length [98], or the attachment points [105] of the bridle. In both cases the aerodynamic forces act on the center of the plates. The aerodynamic forces are calculated via a linear approximation: $C_L(\alpha) = c_L\alpha$, $C_D = c_D + k_D C_L^2(\alpha)$ [105] of via lookup tables for the aerodynamic coefficients ($C_L(\alpha) = f_L(\alpha)$,$C_D(\alpha) = f_D(\alpha)$) [98].

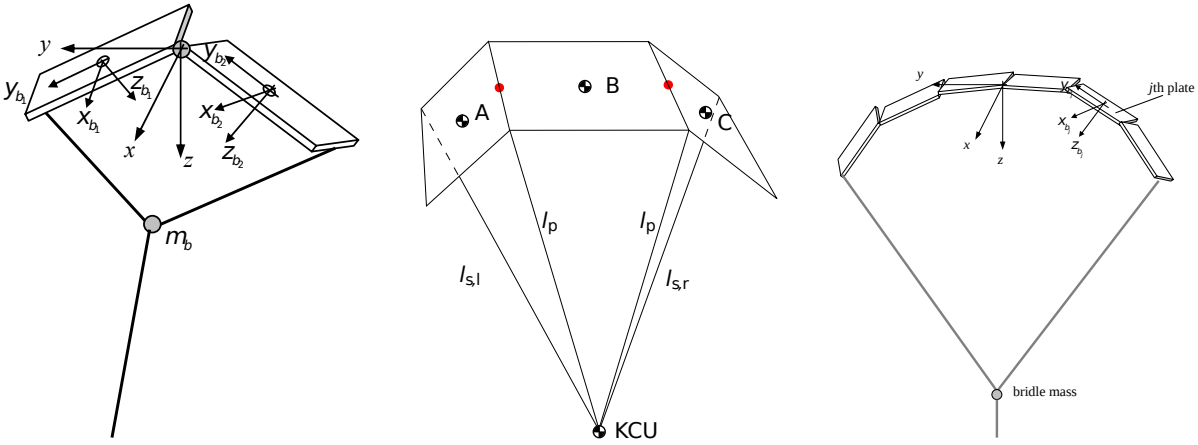

Figure 2.16: Several multi-plate models [105] [98] [60]

FEM Kite Models Besides the dynamical behavior, a finite element kite model tries to capture the flexible modes of the kite. Local and global deformation behavior can be inspected with FEM. In the work of [90], a FEM model is implemented in Madymo, which is a general purpose FEM, CFD and

multibody solver, however the model is not coupled with an aerodynamic model.

[20] can be considered a continuation on the work of [90]. The goal is to make the FEM model faster and not bound to a certain program/implementation while maintaining realisticness. In order to reduce the number of finite elements proper orthogonal decomposition (POD) is applied. Three different options are discussed for applying FEM to the tether + bridle + kite problem: 1) Modeling all three elements with FEM, 2) Modeling the kite + tether with FEM, and 3) only model the kite with FEM. Two types of coupling are discussed which resembles the options discussed in [15] (point mass model). Option 1 is coupling the dynamic equations of the FEM kite model with the dynamic equations of the tether and bridle elements (model exchange); option 2 is assuming the kite fem model to be a quasi-static force generator that exerts force at the bridle and tether(co-simulation). Finally the option is chosen where the rigid body modes and deformation modes are decoupled, the FEM model handles the deformation where the dynamical model handles the rigid body modes. The same aerodynamical model is used as in [21]. The model runs with a real time factor of 27.5.

[40] the flexibility of the kite is not captured by FEM, but by a prescribed deformation of a reference mesh. The aerodynamic forces are determined throught CFD.

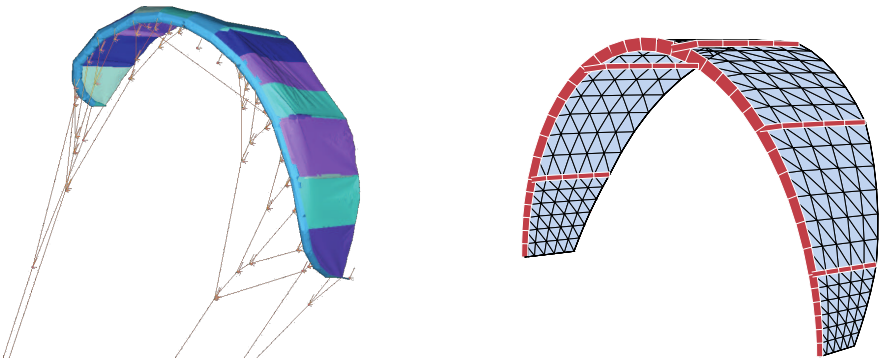

Figure 2.17: Two FEM kite models. Left [90], right [20].

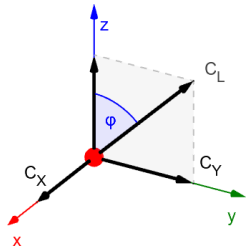

Figure 2.18: Equivalence of the rolling lift vector and a side force. Resolving C_L into C_Y and C_Z.

2.3. Definition and Parameter Identification of Aerodynamic Models for Kites

In the previous sections it became apparent that multiple methods can be used order to model the aerodynamic lift and drag forces. Many models make use of aerodynamic coefficients in order to determine the aerodynamic forces, these will be discussed first. Secondly all other encountered methods will be discussed.

Aerodynamic Models Using Non-Dimensional Coefficients For aerodynamic models that use non-dimensional coefficients, a closed-form expression exist for the aerodynamic forces and torques. The following equations are dimensionless expressions for the forces and torques:

$$\begin{aligned} &\mathbf{F}_a = \left[F_x, F_y, F_z\right]^T \quad \mathbf{M}_a = \left[M_l, M_m, M_n\right]^T \\ &C_x = \frac{F_X}{1/2\rho\|\mathbf{v}_a\|^2 S} \quad C_Y = \frac{F_Y}{1/2\rho\|\mathbf{v}_a\|^2 S} \quad C_Z = \frac{F_Z}{1/2\rho\|\mathbf{v}_a\|^2 S} \\ &C_l = \frac{M_l}{1/2\rho\|\mathbf{v}_a\|^2 Sb} \quad C_m = \frac{M_m}{1/2\rho\|\mathbf{v}_a\|^2 Sc} \quad C_n = \frac{M_n}{1/2\rho\|\mathbf{v}_a\|^2 Sb} \end{aligned} \tag{2.13}$$

With:

C_*	= A dimensionles coefficient
$\mathbf{F}_a$	= The aerodynamic force
F_X, F_Y, F_Z	= The force along the local x-, y-, or z-axis, $F_{\|x}$,$F_{\|y}$,$F_{\|z}$
$\mathbf{M}_a$	= The aerodynamic torque
M_l, M_m, M_N	= The torque around the local x-axis, $M_{\circlearrowleft x}$,$M_{\circlearrowleft y}$,$M_{\circlearrowleft z}$
ρ	= Density of air
$\mathbf{v}_a$	= Apparent velocity
S	= Kite surface area
c	= Kite chord
b	= Kite wing span.

The rotational dynamics for the point-mass model are ignored, thus $C_l = C_m = C_n = 0$. The steering for point mass models is either performed via a side force or a rolled lift vector. From Figure 2.18 it can be observed that a rolled lift vector can be resolved into components along the x and y axis. In that case we obtain $C_Y = \sin(\phi)C_L$ and $C_Z = \cos(\phi)C_L$. In other cases we have, $C_Y = C_S$ and $C_Z = C_L$. Drag is always aligned with the x-axis, thus for both cases $C_X = C_D$.

Different model structures for the non-dimensional aerodynamic coefficients exist. The following models are a summary of the ones found in Tables 2.1 and 2.2:

$$C_* = k_* \tag{2.14}$$
$$C_*(\alpha) = k_{*,0} + k_{*,\alpha}\alpha \tag{2.15}$$
$$C_*(\alpha) = k_{*,0} + k_{*,\dagger}C_\dagger^2(\alpha) \tag{2.16}$$
$$C_*(\alpha) = f_*(\alpha) \tag{2.17}$$
$$C_*(\alpha_1, \dots, \alpha_n) = f_*(\alpha_1, \dots, \alpha_n) \tag{2.18}$$

$k_*, k_{*,0}$ = Constants
$f_*(\alpha)$ = Nonlinear function varying with a state or control variable α.
$f_*(\alpha_1, \dots, \alpha_n)$ = Linear dependent function on state or control variables $\alpha_1, \dots, \alpha_n$.

In Equation 2.14 the coefficient is constant. Equation 2.15 shows a model where C_* is an affine function of α. Equation 2.16 shows a quadratic function with a dependency on another coefficient $C_\dagger$. In Equation 2.17 the coefficient depends nonlinearly on α. Examples of nonlinear functions of Equation 2.17 are shown in Figure 2.19. Equation 2.18 shows a function where linear combinations of the control or state variables contribute to the aerodynamic coefficient.

Alternatively, different aerodynamic coefficients can be chosen for different phases e.g. for reel-out and reel-in as has been done in [97].

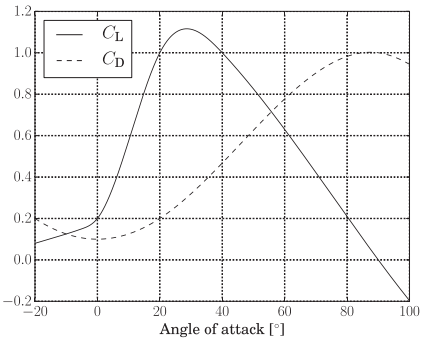

Figure 2.19: Values of the non-dimensional aerodynamic coefficients for varying angle of attack α [38].

Alternative Aerodynamic Models In [15] a panel method uses the shape of a three-dimensional mesh to determine the aerodynamic forces. The control input u prescribes the deformation of the mesh. The mesh is shown in its original and deformed state in Figures 2.20a and 2.20b.

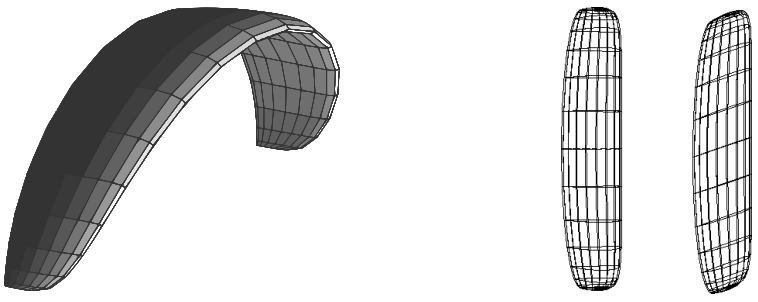

(a) A 3D depiction of the mesh.

(b) A top view of the undeformed and deformed mesh.

Figure 2.20: A deformable mesh that is used for determining the aerodynamic forces with a panel method [15].

[95] makes use of discrete airfoils (Figure 2.21). Each airfoil has a lift and drag force as well as pitching torque through the use of the already discussed non-dimensional coefficients.

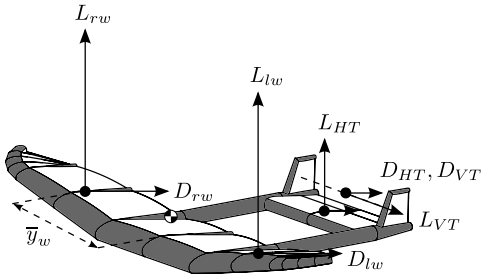

Figure 2.21: A rigid body model of a kiteplane [95]

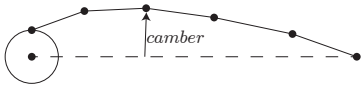

Figure 2.22: A section of the multibody kite airfoil.

[21] uses pre-calculated CFD data to determine the aerodynamic force and torque coefficients. For multiple cord wise sections (Figure 2.22) the aerodynamic lift, drag and torques are determined through the coefficients as a function of airfoil camber and angle of attack. The lift forces are then distributed over the nodes of the airfoil for the modeling of structural deformation. In order to include 3D aerodynamic effects, vortex-lattice method is used to determine a corrected lift distribution (the Prandtl-lifting line theory does not hold for an arc-shaped wing).

Parameter Estimation Methods for the Aerodynamic Models Here, different methods will be discussed that are used for estimating the aerodynamic model coefficients as tabulated in Tables 2.1 and 2.2. First the different methods of obtaining flight data and fitting the coefficients will be discussed. Afterward a remark is being made on the difficulties encountered in the estimation of the coefficients.

The previous sections showed several definitions for the non-dimensional aerodynamic coefficients. In the case where nonlinear curves are used in order to look up $C_L(\alpha)$ and $C_D(\alpha)$, the curves are precomputed. The coefficient values or curves can be based on: 1) Simulation of higher-fidelity models, and 2) experimental data from measurements.

[45] uses a higher-fidelity model to for the estimation of aerodynamic model parameters. By simulating reference flight manouevres with a multibody model of a kite and performing linear regression, the coefficients for the non-dimensional forces and torques are estimated in [45] . The method is identical to the methods used for aircraft system identification [58]. Another example of the use of a computational approach for the aerodynamic parameter estimation can be found in [60]. A zero thickness 3D mesh is used in combination with Vortex-Lattice software to estimate the aerodynamic parameters. Details are not provided.

In [82] and [96] several methods are discussed for the estimation/ determination of the aerodynamic parameters/curves through experiments. The most common of these methods are:

- Wind tunnel testing;
- (car) tow testing;
- circular testing;
- dynamical testing;
- static flight testing.

Wind tunnel tests allow the experiments to be performed in a controlled environment. However, costs increase with increasing kite size [96]. Making use of scale models is impossible due to material constraints.

With (car) tow testing, the kite is towed while forces and positions are being measured. Tow tests have been performed on multiple occasions [82] [27]. However, this method is plagued by the difficulty of obtaining accurate data [93]. Furthermore, the apparent wind speed was often not available as a

measurement, therefore in [82] a remark is made on the importance of the apparent wind speed data for tow testing.

For circular testing the kite is connected to an arm which rotates around an axis perpendicular to the horizontal plane. This method is also limited to smaller kites.

Dynamical testing requires the kite to be flown outdoors in specific patterns, e.g. crosswind or specific turns. There is no limit to the kite size. Disturbances in the wind might influence the results. In [60] flight data is obtained by physically flying a kite using a specific control algorithm. No details are provided about the identification techniques used.

A linear least squares method is applied to flight data to estimate the aerodynamical coefficients in [84]. $C_L(\alpha), C_D(\alpha)$ are based on combining data for $C_R(\alpha)$ and the glide ratio (L/D). The glide ratio is not based on measurements, but based on an analytical relation between the wind speed and the kite's tangential speed via $v_{k,\tau} = \frac{L}{D} v_w$, $\frac{L}{D} = G$. The aerodynamic force coefficient $C_R(\alpha)$ is determined from the experimentally obtained resultant aerodynamic force F_a and then smoothed.

In [36] two experimental sessions were performed in order to provide data for comparison with the simulated model. During these sessions a kite has been flown in figures of eight through manual control of the kite. The estimation of model parameters is not discussed.

In [38] two types of maneuvers were performed in order to obtain data for the estimation of model parameters for a point-model and a 4-point particle model. The data from a parking maneuver is used for the estimation of aerodynamic and wind field coefficients; turn maneuver data is used for the estimation of steering sensitivity parameters. The Pearson correlation coefficient is used as a measure to indicate the correctness of the estimated parameters. The measured power output has been compared with the output from the simulated models and a two dimensional projection of flight trajectory is used as a means of comparison of different flights. Parking maneuvres are also performed in [28].

Various attempts have been made in order to find a relation between the angle of attack (or power setting) and the aerodynamic coefficients ([84][82][78]). From Figure 2.23 it can be observed that the spread of measurement data is very large, the fitted polynomial model required manual adjustments to get realistic simulation results.

In Figure 2.24 the glide ratio is shown with respect to the power ratio, the spread is smaller, however inconsistencies exist between static and dynamic flight tests. Additionally since the relation between the power setting and the angle of attack is not deterministic [82], an expression in terms of glide ratio increases the spread. Finally, Figure 2.25 also shows quite a large spread of the data except for the relation between the glide ratio and the apparent wind velocity.

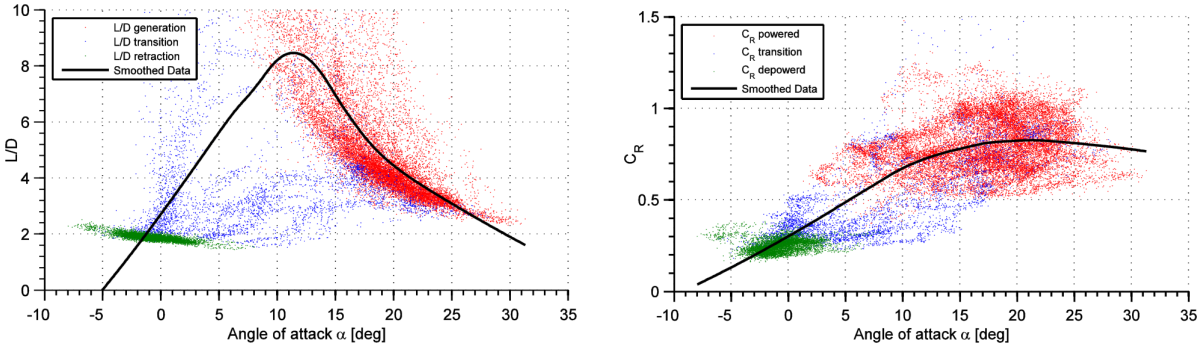

Figure 2.23: Glide ratio and resultant force coefficient versus the angle of attack [84].

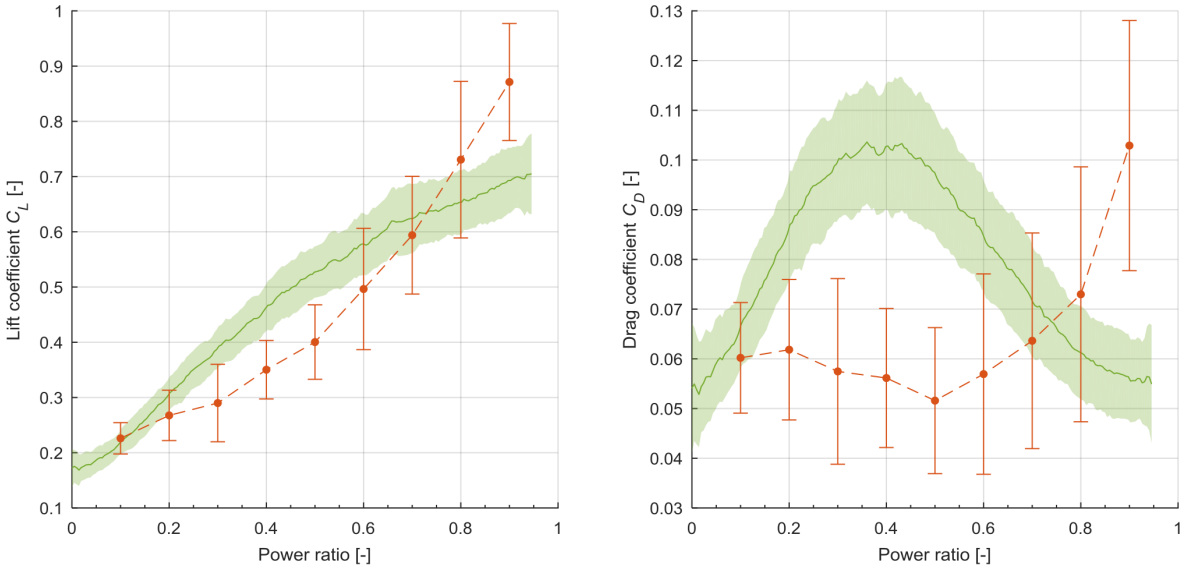

Figure 2.24: Lift and drag coefficients versus power ratio for static (red) and dynamic (green) tests [82].

2.3.1. The Different Types of Tether Models

Similar to the section about kite models, an overview of different tether models will be provided. In [41] five tether models are identified:

1. Straight-line, approximates the tether as a straight line between the kite and the attachment point;
2. Catenary, includes weight effects leading to a curved tether.
3. Constant velocity, assumes a constant wind velocity at each altitude.
4. Variable velocity, assumes a variable wind velocity at each altitude.
5. Maximum stress, assumes maximal stress at each location in the tether.

The straight tether models are treated separately and all flexible tether models (2-5) are grouped and treated afterward.

During the traction phase, when the tether tensions is high compared to the aerodynamic drag and gravity, a straight tether model is accurate enough. However, during launch, landing, retraction and transition, tether sag cannot be neglected [97], and therefore tether flexibility needs to be taken into account.

Straight Tether Models The straight tether assumption is justified for the traction phase in [21] . There it is derived that the drag of the tether only contributes roughly 2% of the tether tension. The additional tension due to tether mass is said to be even smaller (for a $10m^2$ kite on a tether of 100m length).

The encountered straight tether models in the literature have been tabulated in Table 2.3. Besides the type (elastic or inelastic) several other aspects are included. The columns stating: 'Gravitational', 'Inertial' and 'Aerodynamical', consider physical contributions of the tether. The column 'Reeling' indicates whether the tether is of a fixed or variable length. The 'Implementation' columns contains one of the two entries: 'Newtonian', 'Lagrangian', or 'Analytical', this says something about the method used for obtaining the motion from the forces.

Gravity and inertia are, in many cases, handeled quite similarly. The tether mass (m_t) is combined with the kite mass (m_k) and together form the 'effective gravitational mass' $\tilde{m} = m_k + \frac{m_t}{2}$ and the 'effective inertial mass' $\underline{m} = m_k + \frac{m_t}{3}$ [53]. For Newtonian mechanics this directly affects the total gravitational and apparent accelerational forces. In Lagrangian mechanics this increases the potential and kinetic energy, aditionally the generalized gravitational force is altered. [109] does not use the effective gravitational and inertial mass, but directly includes the tether mass in the kinetic and potential

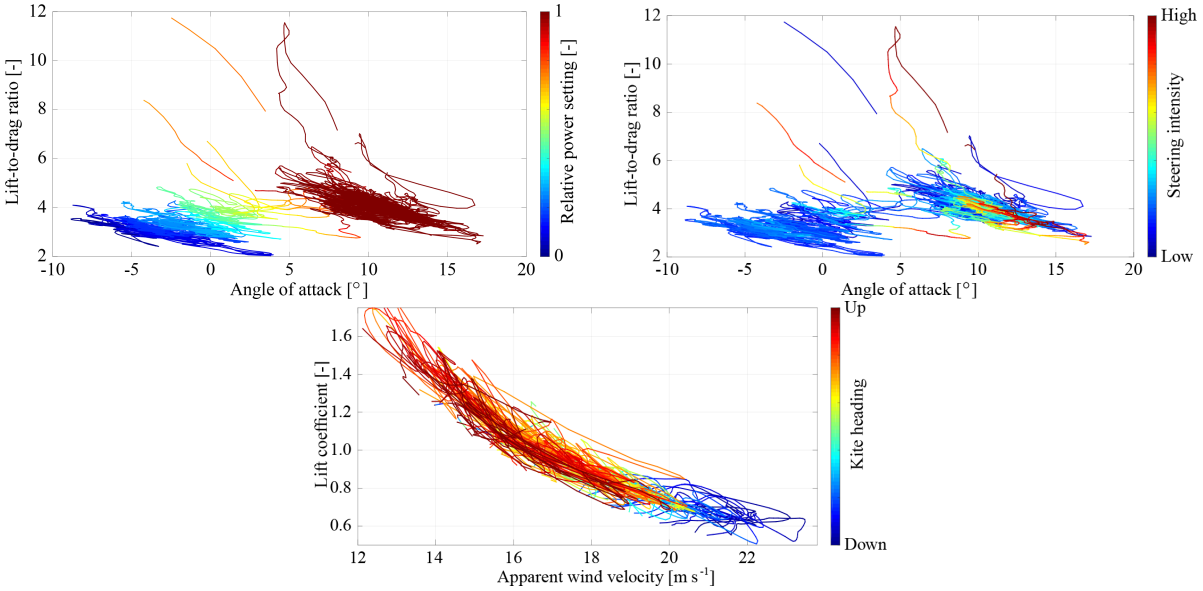

Figure 2.25: Relation of lift and lift-to-drag with respect to measured variables[78].

energy terms, the resulting potential and kinetic energy contributions by the tether are identical. For the gravitational contribution, [36] lumps the full tether mass at the kite. In [68] the full tether mass is lumped at the kite for the gravitational contribution, for the inertial contribution the tether mass is projected in the direction of the tether rope.

Analytical models generally ignore tether mass in the inertia terms. Regarding the gravitational contribution of tether mass,[97] presents an alternative method to include the tether mass for straight tether models. Tether sagging is taken into account. The tether sagging introduces an internal tether tension which results in a tangential force component at the kite.

Two different types of straight tether models have been encountered, namely the elastic and inelastic type. When included, elasticity is often combined with damping. The force in the tether depends on its elongation $r - r_0$ and the error in the radial velocity $\dot{r} - \dot{r}_0$. The reference radial velocity $\dot{r}_0$ is zero for fixed-length tethers. E and A are the materials elasticity and cross-sectional surface are respectively. The tether constraint force is as follows ([53]):

$$F = \frac{EA}{r_0}(r - r_0) + b(\dot{r} - \dot{r}_0) \tag{2.19}$$

For Lagrangian dynamics, the tether constraint force is one of the generalized forces. [53] includes the stored energy of the spring-like tether in the potential energy term of the Lagrangian. Oftentimes it is omitted due to the negligible effect.

For inelastic tether, a set of coordinates is chosen such that the tether length is either constrained or directly controlled. In [20] spring-damper bridle elements in combination with a straight inelastic tether are used.

Tether drag is lumped at the kite (or bridle) by several tether models. The corresponding drag force is determined by integrating the angular momentum caused by tether drag. In [53] a pessimistic drag is derived, since the effective wind vector $\mathbf{w}_e$ is not perpendicular to the tether. A correction given in [36]. The drag ($\mathbf{F}_f$) as derived in Appendix A, [63] and more clearly in [53], depends on the effective wind

speed $\mathbf{w}_e$, air density ρ, drag C_D and the cross wind area A_c:

$$\mathbf{M}_f = \int_0^1 (sr\mathbf{e}_r) \times \frac{\rho C_D d}{2} (s\|\mathbf{w}_e\|)^2 \frac{\mathbf{w}_e}{\|\mathbf{w}_e\|} ds \tag{2.20}$$

$$= (r\mathbf{e}_r) \times \frac{\rho C_D A_c}{8} \|\mathbf{w}_e\| \mathbf{w}_e \tag{2.21}$$

$$\mathbf{F}_f = \frac{\rho C_D A_c}{8} \|\mathbf{w}_e\| \mathbf{w}_e \tag{2.22}$$

Some kites are controlled by 2 lines [31] [36], so mass and drag are counted double. The drag in [101] has been calculated differently. There the tether is discretized into n elements. The total drag consists of the sum of the individual element contributions. Results for different n are shown, and it is said that the difference between $n = 20$ and $n = 2000$ is negligible. This results in two (generalized) forces:

$$Q_\phi = -\sum_{j=1}^{n_e} \frac{1}{2} \rho C_d A_{c,j} \mathbf{v}_j |\mathbf{v}_j| \frac{\partial \mathbf{r}_j}{\partial \phi}, \quad Q_\theta = -\sum_{j=1}^{n_e} \frac{1}{2} \rho C_d A_{c,j} \mathbf{v}_j |\mathbf{v}_j| \frac{\partial \mathbf{r}_j}{\partial \theta} \tag{2.23}$$

n_e is the number of tether elements, $A_{c,j}$ is the element's cross wind area, $\mathbf{v}_j$ is the apparent wind velocity normal to the cable, $\mathbf{r}_j$ is the element's location, ϕ and θ are generalized coordinates.

Reeling in indicates wether the tether has a fixed or variable (unstrained) length. The way reeling is implemented depends on the elasticity of the tether. In the inelastic case, the radial coordinate $\dot{r}$ is manipulated directly. In the elastic case, the tether reference length $\dot{r}_r$ is controlled.

The tether models in the analytical approach are inelastic by nature. The analytic approach assumes a force equilibrium at every flight state, the position of the kite is prescribed by the tether length and orientation. Reeling velocity can be prescribed.

Table 2.3: An overview of the encountered variations of straight tether models. A hyphen indicates that a certain aspect is ignored in the tether model. $\bar{m}$ is the effective gravitational mass. k indicates spring stiffness, c damping.

Source	Type	Gravity	Inertial	Aerodynamical	Reeling	Implementation
[36]	Inelastic	$\bar{m}$	-	Drag lumped at kite	Yes	Newtonian
[31],[76],[32]	Inelastic	-	-	-	No	Newtonian
[63]	Inelastic	-	-	-	Yes	Analytical
[63]	Inelastic	$\bar{m}$	-	Drag lumped at kite	No	Newtonian
[45]	Elastic (k+c)	-	-	-	No	Newtonian
[29],[21]	Elastic (k+c)	-	-	-	No	Newtonian
[95]	Elastic (k+c)	-	-	-	Yes	Lagrangian
[105],[106]	Elastic (k)	-	-	-	No	Lagrangian
[20]	Inelastic	-	-	Drag lumped at bridle	No	Newtonian, TMT [89]
[28]	Inelastic	-	-	-	No	Analytical
[101]	Inelastic	Potential energy + generalized force	Kinetic energy	Discretized in $n \approx 20$ elements to calculate the drag	No	Lagrangian
[109]	Inelastic	Potential energy + generalized force	Kinetic energy	Discretized in $n \approx 20$ elements to calculate the drag	Yes	Lagrangian
[52]	Inelastic	$\bar{m}$	$\underline{m}$	Drag lumped at kite	No	Newtonian
[68]	Elastic (k+c)	$\bar{m}$	Projection of tether inertial contribution	Discretized in n elements to calculate the drag	Yes	Newtonian
[97]	Inelastic	Sagging-induced force	-	Drag lumped at kite	Yes	Analytical
[51],[50]	Inelastic	$\bar{m}$	$\underline{m}$	Drag lumped at kite	Yes	Lagrangian
[21]	Inelastic	-	-	-	Yes	Lagrangian
[84]	Inelastic	$\bar{m}$	$\underline{m}$	Drag lumped at kite	Yes	Lagrangian
[53],[84]	Elastic (k+c)	$\bar{m}$	$\underline{m}$	Drag lumped at kite	Yes	Lagrangian

Flexible Tether Models Besides tethers models for AWE, research into flexible cables is also performed for underwater, space [102], and civil applications. Here we will focus on the AWE application. The literature shows the following main approaches for the modeling of a flexible tether: (1) continuum models and (2) lumped mass models. Both model types are able to capture the flexibility of the tether. The importance of incorporating tether flexibility will be discussed first, followed by a brief discussion of continuum models. The lumped mass models are covered more in-depth including some implementation specifics. Differences in aerodynamic models are highlighted. Tether reeling and tether elasticity of flexible tethers are discussed in separate paragraphs.

[14] shows that for an increase of 5% of the catenary curve, the angle at point B changes with 50% (Figure 2.26, left). What this says is that when a flexible tether assumes the shape of the catenary curve is and the total length is 5% longer than a straight tether, the angle of the tether force at the kite changes by 50%. Tether sag also greatly influences the relation between force and distance between the attachment points of the tether (Figure 2.26, right).

Tethers often made of Dyneema. Due to its high tensile stiffness, compression, transverse shear, bending and torsional stiffness are often neglected [19] [104] [51]. Commonly used material stiffnesses can be found in Table C.3. The curve that describes the shape of a free hanging cable without bending stiffness between two attachment points (including gravity effects) is called the catenary curve. The catenary curve is often used to validate flexible tether models. The following equation show the catenary curve where the lowest attachment point is located at $x = 0$:

$$z = a \cosh\left(\frac{x}{a}\right) \tag{2.24}$$

$$a = \frac{F_t}{g \rho_t A_t} \tag{2.25}$$

z = Vertical displacement
w = Horizontal distance between attachment points
x = Horizontal distance from leftmost attachment point
F_t = Horizontal tension
g = Gravitational constant
ρ_t = Tether material density
A_t = Tether cross sectional area

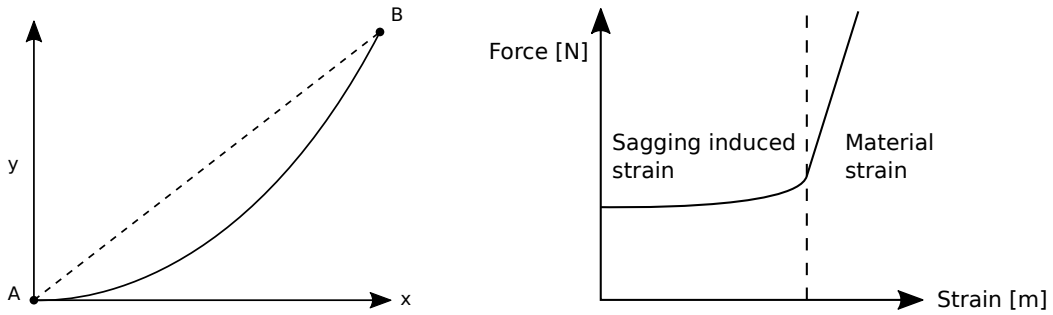

Figure 2.26: Particle tether. Adapted from [30] (left), and [14] (right).

The importance of tether flexibility is further stressed in [86]. There it is shown that a increasing the number of tether segments, the resulting flight path converges.

This brings us to the different flexible tether models. The flexible tether models vary in implementation. Newtonian, Lagrangian and Hamiltonian approaches have been encounteres Table 2.4. Continuum models are formulated via partial differential equations which are typically solved by using an analytical approach or a finite difference method, but alternative methods exist [103] [102].[41] mentions that

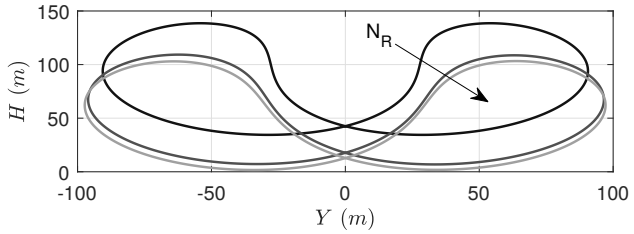

Figure 2.27: Kite flight path convergence with increasing number of elements ($N_R = 1, 2, 3$), adapted from [86]

for continuum methods in the case where one of the boundary conditions is unknown, trial-and-error methods must be applied in order to satisfy the boundary conditions. [103] Proposes a flexible tether model which is based on a quasi-steady assumption of the tether. An iterative multiple shooting method is applied to find the tether shape (and tension), depending on the prescribed reel-out velocity (or tether tension) and the cable tip velocity. The most important fact to note is the achieved speedup (1000x) compared to the other lumped-mass models.

Lumped mass models know a much coarser discretization of the tether in comparison to continuum models. Lumped mass models represent the tether as a series of discretized (connected) masses. Lumped mass models describe the cable dynamics through the motion of several or many masses. A schematic of a lumped mass tether model is shown in Figure 2.29. Figure 2.28 shows the different level of discretizations. A coarse discretization (with large segment lengths) is used for the lumped mass approach, whereas much smaller segment lengths are used for the continuum approaches (infinitesimal of finite difference).

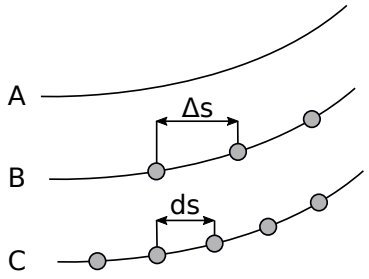

Figure 2.28: Different levels of discretization: A) The real tether, B) a coarse discretization, C) a finer discretization. Adapted from [30].

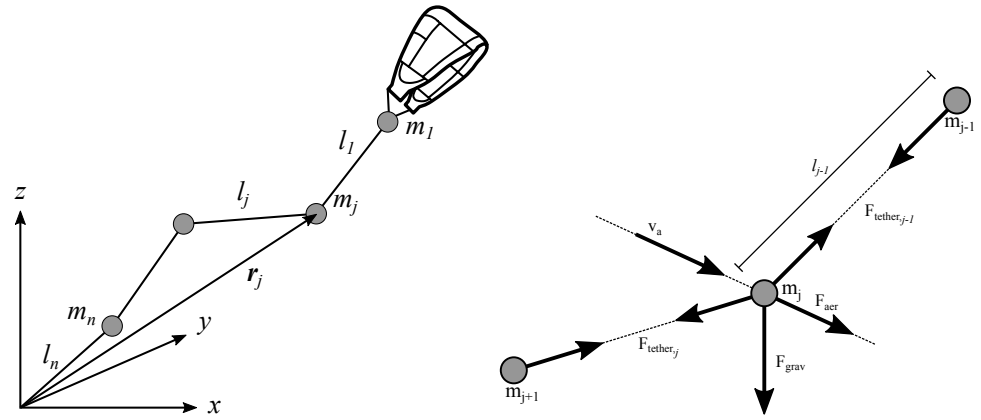

Figure 2.29: Left: a lumped-mass tether model, adapted from [107]. Right: forces acting on the j^{th} point mass, adapted from [84].

The mass of each lumped-mass is generally equal to the average adjacent tether segment mass, with exceptions for the first and final mass. The amount of tether segments varies between different publications and reports (Table C.3), depending on the required accuracy and computational performance. Generally, the accuracy increases with increasing amount of elements. The model in [21] requires no more than 10 elements to obtain an cable equilibrium error smaller than 5% (Figure 2.30).

Lumped-mass tether models have been verified on multiple occasions. [104] Compares a lumped mass model with experimental results and shows good agreement. [84] uses three methods to validate the implementation of the tether model: 1) A comparison is made with the catenary curve, 2) The effect of wind shear is evaluated which shows identical results as [107], and 3) An experiment has been performed where a mass of 10 kg is added to the tether and the linear responses of the real tether and model are compared.

In [22] a 32m cable has been hung from a building and a large number of experiment has been performed. In these experiments, the tether was exited at the top and the time it took for the wave to

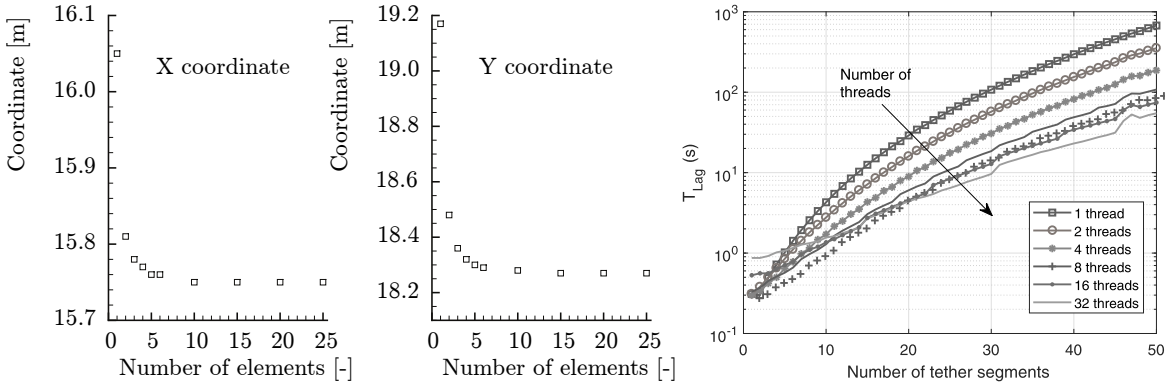

Figure 2.30: Left: Convergence of endpoint coordinates of numerical experiment [21]. Right: Computational time versus number of tether segments. Adapted from [86]

propagate to the end of the tether has been measured. The results of the experiment have then been compared with simulation results and showed good agreement. Additionally the influence of the number of tether elements of the model convergence is inspected, convergence is shown from around 5 segmentsFigure 2.27, left.

The effect of the number of elements on the computational speed has been investigated for a Lagrangian implementation in Fortran, additionally the effect of parallelization has been investigated (Figure 2.30, right).

Table 2.4: * most likely. LM = lumped-mass, RB = Rigid Body. k = stiffness, c = damping. This table is constructed through a query, rows are not combined.

Source	Type	Gravity	Inertial	Reeling	Implementation
[38]	LM (k+c)	Y	Y	Y	Newtonian
[68]	LM (k+c)	Y	Y	Y	Newtonian
[68]	LM (k+c)	Y	Y	Y	Newtonian
[21]	RB	Y			
[86]	LM, inelastic	Y	Y	Y	Lagrangian and Hamiltonian
[30]	LM (k)	Y	Y	Y	Newtonian
[62]	LM(k+c)	Y			Newtonian
[103]	LM, inelastic	Y	N	Y	
[22]	RB	Y	Y	N	MSC ADAMS
[101]	LM, inelastic	Y	Y	Y	Kane
[81]	Continuum (k)	Y	Y	N	Newtonian
[41]	Continuum	Y	Y	N	Analytical
[19]	Continuum	Y	N	N	Analytical
[57]	LM (k)	Y			
[42]	LM (k)	Y			
[104]	LM(k+c)	Y	Y	N	
[4]	Continuum	Y			
[107]	LM, inelastic	Y	Y	Y	Newtonian
[14]	LM (k+c)	Y	Y	Y	Newtonian
[103]	LM (k+c)	Y	Y	Y	
[72]	LM (k+c)	Y	Y	Y	
[13]	LM (k+c)	Y	Y	Y	Newtonian
[109]	LM, inelastic	Y	Y	N	
[84]	LM (k+c)	Y	Y	Y	Newtonian

Table 2.4 shows an overview of the encountered flexible tethers in literature. It is not the goal to give a complete overview, the table serves the purpose of listing the different variations that can exist for flexible tether models. Other information required so much space such that it was deemed necessary to place this into separate tables which can be found in the appendices (Table C.2, Table C.3, Table C.1).

Finally, several implementation details will be mentioned. Firstly, in [22] [21], elements available of MSC ADAMS® are used to construct the tether. Two Hooke's joints are used to couple the elements. It is said that by using two Hook joints instead of spherical coordinates, the axial vibrations are disregarded and the whole simulation is sped up. Secondly a simplified 2D model is used in [101]. Lastly, [87] includes ground reaction forces in the tether model. If any lumped-mass is below the ground level, the ground reaction force is determined according to a spring-damper relation. Additionally a friction force is introduced which is linearly dependent on the ground reaction force.

Tether Segment Aerodynamics in Lumped-Mass Tether Models Different methods are used in order to determine the aerodynamic forces. This section describes some of the encountered methods as summarized in Table C.2. The aerodynamic models differ mainly on the following points:

- The location for the determination of the apparent wind speed;
- The resolution of the wind field;
- Lumped or distributed aerodynamic load;
- Orientation of the aerodynamic loads: perpendicular and tangential to the element, or, the apparent wind speed;
- Variable or fixed aerodynamic coefficients;
- The inclusion of friction +/ lift.

The aerodynamic forces are either determined at the location of the lumped mass, or at the segment locations. In the segment-wise case, the forces are distributed equally over the adjacent lumped masses.

The wind field can be assumed constant or varying with altitude. Often a reference altitude is determined per segment (or lumped-mass), but also the inter-segment varying wind field can be into account.

Instead of a point-wise determination of the aerodynamic load on a tether segments, the aerodynamic forces and torques can be integrated over the segment length taking the local apparent wind speed (and optionally the wind field) into consideration. The forces and torques are then distributed accordingly over the adjacent lumped-masses.

Expressions exist for determining the aerodynamic forces with respect to the aerodynamic frame, or the local tether segment frame. Transformations exist, more about this later on.

Whereas some models determine the aerodynamic load by only a drag component, two and even three component aerodynamic force. Two components are generally lift and drag, or tangential and perpendicular drag. A third component is identified as a sideways lift force [104] occurring on cables with helix-grooves, this is generally disregarded. All tether drag models are based on treating each tether element as a cylinder.

Three methods can be used to determine the aerodynamic force of which the first method (Equation 2.26)[48] is the most commonly used and describes the force for each individual aerodynamic force component. In [104] an alternative method to determine the aerodynamical force on the tether is proposed, using the Nordell-Meggit equation [79] Equation 2.27 which combines tangential and normal aerodynamic forces. The angle of attack (η) is used in [33] (Equations 2.28 - 2.31), also to determine normal and tangential aerodynamic forces. The superscripts 'n' and 't' indicate normal and tangential

components respectively.

$$\mathbf{F}' = \frac{1}{2}\rho dlC|\mathbf{v}'|\mathbf{v}' \tag{2.26}$$

$$\mathbf{F} = -\frac{1}{2}\rho\pi dl(A|\mathbf{v}| + B|\mathbf{v}^t|)\mathbf{v}^t + \frac{1}{2}\rho C^n dl|\mathbf{v}^n|\mathbf{v}^n \tag{2.27}$$

$$\mathbf{F} = -\frac{1}{2}\rho C dl|\mathbf{v}|^2\left(f^n\frac{\mathbf{v^n}}{|\mathbf{v^n}|} + f^t\frac{\mathbf{v^t}}{|\mathbf{v^t}|}\right) \tag{2.28}$$

$$f^n = 0.5 - 0.1\cos\eta + 0.1\sin\eta - 0.4\cos 2\eta - 0.011\sin 2\eta \tag{2.29}$$

$$f^t = 0.01(2.008 - 0.3858\eta + 1.9159\eta^2 - 4.16147\eta^3 + 3.5064\eta^4 - 1.187299\eta^5) \tag{2.30}$$

$$0 \leq \eta \leq \frac{1}{2} \tag{2.31}$$

$\mathbf{F}$ = Aerodynamic force
$*'$ = Individual component, e.g. drag or lift
$*^n$ = Normal component
$*^t$ = Tangential component
ρ = Density of air
d = Diameter
l = Length
$\mathbf{v}$ = Apparent wind speed
A, B, C, f = Aerodynamic coefficients
η = Angle with respect to the apparent wind flow

The aerodynamic coefficient in Equation 2.26 can be fixed, or depend on (non)linear function of the angle of attack and the Reynolds number. The lift-drag and normal-tangential coefficients are related throught the following transformation [104]:

$$\begin{bmatrix} C_L \\ C_D \end{bmatrix} = \begin{bmatrix} \cos\eta & -\sin\eta \\ \sin\eta & \cos\eta \end{bmatrix}\begin{bmatrix} C_n \\ C_t \end{bmatrix} \tag{2.32}$$

Tether Elasticity in Lumped-Mass Tether Models Tethers often made of Dyneema [5, p. 410] [68] [45]. The tensile stiffness of tethers is in the order of 50-100 GPa (see Table C.3). Due to its high tensile stiffness, other material properties such as compression, transverse shear, bending and torsional stiffness are often neglected [19] [104]. Some models exclude tether elasticity (and damping) as well. Here a look will be taken at the motivations for (not) including tether elasticity and the consequences of it. Table 2.5 shows a summary of the pro's and con's.

[38] states that using inelastic elements is not sufficient for modeling the tether force and implementing the force control loop. Inelastic tether models do not give information of the internal tether force.

Incorporating tether elasticity [107] (in combination with the Newtonian approach) eliminates the need for constraint stabilization and the calculation of the derivatives of the constraint equations.

In order to cope with cable slack (zero tension or compression), in [14] the aerodynamic and the spring-damper forces are set to zero. [57] sets the stiffness for compression 10 times smaller than that for tension.

In lumped-mass models, the tether shows fast longitudinal waves due to high stiffness of the tether. The combination of the fast longitudinal waves and the slower transversal waves cause the problem to be stiff, which requires implicit integrators [86]. For this reason an implict Euler integrator scheme is used in [62] for the simulation of a lumped-mass tether model.

The fast vibrations have low amplitudes [22]. Assuming the tether to be inelastic removes the fast longitudinal oscillations. Since the transversal motion of the kite is of much lower frequency, removing the fast oscillations results in a less stiff numerical problem. It is said that the reliability is not significantly

influenced by this assumption [86]. Ignoring the fast longitudinal oscillations allows for larger time steps [22].

The following equations describe the spring-damper forces acting on the i-th particle [38]:

$$\mathbf{F}_i = \mathbf{F}_{s,i-1} + \mathbf{F}_{s,i} \tag{2.33}$$

$$\mathbf{F}_{s,i} = \left(k\|\mathbf{s}_i\| - l_s) + c\left(\frac{\mathbf{s}_i}{\|\mathbf{s}_i\| \cdot \mathbf{s}_{v,i}}\right)\right)\frac{\mathbf{s}_i}{\|\mathbf{s}_i\|} \tag{2.34}$$

$$\mathbf{s}_i = \mathbf{p}_{i+1} - \mathbf{p}_i \tag{2.35}$$

$$\mathbf{s}_{v,i} = \mathbf{v}_{i+1} - \mathbf{v}_i \tag{2.36}$$

$$\mathbf{v}_{s,i} = 1/2(\mathbf{v}_{i+1} + \mathbf{v}_i) \tag{2.37}$$

$\mathbf{F}_i$ = The sum of spring-damper forces acting on the i-th particle
$\mathbf{F}_{s,i}$ = Spring-damper forces
$\mathbf{s}_i$ = Displacement between adjacent particles i and $i+1$
$\mathbf{s}_{v,i}$ = Relative velocity between particles i and $i+1$
$\mathbf{v}_{s,i}$ = Average segment velocity
k = Stiffness
c = Damping
l_s = Reference segment length

Table 2.5: Pro's and con's of tether elasticity in lumped-mass tether models [107].

Elastic	Inelastic
+ Internal tether tension as an explicit function of the lumped mass positions	+ Removes high frequency longitudinal oscillations, generally leading to a dramatic reduction in simulation time
+ Inertial decoupling of EOM resulting in efficient computation state derivatives	- Requires a complex set of equations (Lagrtane/Kanes) or an additional set of (stabilized) constraint equations (Newton) (besides the EOM).
- Small integration steps or the use of stiff solvers in combination with numerical calculation of the Jacobians leads to long simulation times	

Tether Reeling in Lumped-Mass Models Several methods have been encountered to incorporate varying tether lengths. These methods are tabulated in Table C.1. Zooming in to the most encountered flexible tether models, the lumped-mass model, the following methods have been encountered:

- Simultaneous change of length of all tether segments.
- Simultaneous change of the reference length of all tether segments.
- Control of the length of the element closest to the ground, fixed amount of segments.
- Control of the length of the element closest to the ground, introduction and removal of tether segments with fixed length.

In models without spring-damper elements, directly varying the individual segment lengths leads to incorrect velocities [103], therefore the element lengths should be fixed. For models with spring-damper elements, an alternative method is to change the reference length of the tether segments (see Equation 2.34). Alternatively, only the length of the first tether segment could changed.

The fourth method will be discussed in detail. This method is shown in Figure 2.31. All elements except the first element have a constant (reference) length. The length of of the first element is controlled [38] . When the length of the first element increases past a certain threshold length ($k^* l_n$), a new element gets

introduced in between the last point mass and the tether source. Conversely, when the length of the first element is reduce below a (different) threshold length ($k^{**}l_n$), the first element is removed.

In [72] it is shown (Figure 2.32) that a variable spring stiffness of the final element (the one closest to the winch), causes a relatively high fluctuation in tether force. The cause of this could not be found, therefore the spring constant constant has been kept constant.

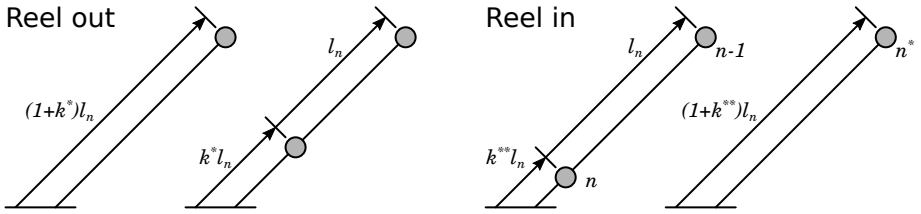

Figure 2.31: Element generation and elimination for reeling out and in respectively. Adapted from [107].

$$l_s = \frac{l_{t,i}}{n} + \frac{v_{t,o}(t - t_i)}{n} \tag{2.38}$$

$$k = k_0 \frac{l_0}{l_s} \tag{2.39}$$

$$c = c_0 \frac{l_0}{l_s} \tag{2.40}$$

Numerical difficulties arise on the introduction and removal of elements. Shockwaves observed in [30] when new tether elements were added. Especially when the cable is elastic, it is of great importance to not introduce unnecessary cable oscillations resulting from the introduction of new elements[107]. Exactly this problem is encountered in [38], resulting in artificial discontinuities hindering force control. During reeling in and out at each time step, the stiffness and damping of the first element are updated. For inelastic cables it suffices to place the new mass exactly in line with the existing element.

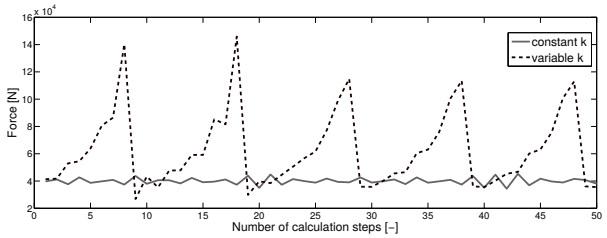

Figure 2.32: Internal force in the spring element attached to the winch for a constant and varying spring constant. Adapted from [72].

Previously, the threshold for reeling in and out was set to be exactly equal to the (fixed) segment reference lenghts. This caused singularities. [68] Solves the singular length by setting a small initial nonzero length to the first element δl_l. To overcome the zero mass problem (causing large accelerations of the first element), a larger initial length is chosen $\delta l_m > \delta l_l$. To work around the stiffness calculation singularity, the stiffness coefficient c_k is determined by δl_m. δl_l and δl_m are used until the segment length and mass are large enough to avoid singularities.

A positive aspect of the above mentioned methods is that they are the easiest to implement due to the constant amount of elements. The downside is the lower physical fidelity. In order to maintain a constant length state vector (since the simulation tools do not allow for a variable state vector) in combination with the above mentioned reeling method, in [87] the tether elements are 'fixed' to the winch when reeled in.

2.3.2. Overview of Software Suitable for the Simulation of Kite and Tether Models

Existing kite simulation software will be provided first Table 2.6, after which several multibody dynamics software tools are tabulated (Table 2.7) that can also be used to implement a kite + tether model .

Table 2.6: An overview of available kite simulation tools. Languages: C++=C++, F=FORTRAN, J=Java, M=Matlab,P=Python. * = modified by a master student in 2016.

Name/ author	Language	Implementation	Latest release	Source
LAKSA/KiteAcrobat	M	Lagrangian	2018-04	[85]
LAKSA/KiteElastic	M	Lagrangian	2018-04	[86]
LAKSA/KiteFlex	F, M	Lagrangian	2018-04	[86]
LAKSA/KiteSurf	M	Newtonian	2018-04	[86]
FreeKiteSim	P	Newtonian	2015-05*	[38] [57]
AWE-box	P	Lagrangian 2019-04-26	[83]	
KiteSim	J	Newtonian	2014-02	[62] [72] [30]
S. Rapp	M	Newtonian	2017-10**	[38]
Kitepower	P	Newtonian	2018	[-]

LAKSA stands for *LA*grangian *K*ite *S*imul*A*tor. It's *KiteAcrobat* module simulates two-line kites and aims at kite traction applications. The *KiteElastic* module allows the user to link several tethered vehicles by elastic and flexible tethers. *KiteFlex* is a module for a tethered vehicle for ground and flight generation. Attached to the ground by an inelastic and flexible tether, implemented as a series of infinitely thin and stiff rods. Control via a 3-line bridle and/or aerodynamic surface deflections. Reel-in and reel-out by a control variable, influencing the lenght of all tether elements simultaneously. The *KiteSurf* module is set-up around four-line kites. It combines inelastic (two front) and elastic tethers (two back). Its applications are kite-surf related and/or parameter identification. The tether length is fixed, so no reel-in or reel-out is possible. The kite is modeled as a rigid-body, located at the end of the tether. The same aerodynamic kite model is used for all four LAKSA modules. Aerodynamic forces and torques are calculated through superposition of the individual aerodynamic contributions such as lift, drag, torques, and the aerodynamic effects of elevator deflections.

FreeKiteSim is a simulation framework written which simulates all system components, i.e. kite, tether and ground-station. It is built around Newtonian mechanics. Two different solvers can be used: RADAU5 [46] and Sundials's IDA [47]. Both solvers are interfaced through Assimulo [7], which is a simulation package for solving ordinary differential equations in Python . By default the (stiff) RADAU5 solver is used in combination with just-in-time compilation in order to allow the simulation to achieve real-time performance. Tether reel-in and out are performed by updating the length of all tether elements, and updating the stiffness and damping accordingly. The latest work using FreeKitesim has been performed in 2016 [57], where a rigid wing is modeled by a particle system. Currently this simulator does not work out-of-the box.

Kitesim is a kite simulator in Java. Work on this simulator started in 2010 [30] and is based on an existing particle-system library which uses implicit-euler integration [44] for the integration of the Newtonian mechanics. The kite is implemented as a point mass and the tether is implemented as a set of particles. In 2011 varying tether length has been added [72] and in 2012 rotational inertia is added to the kite by using a three-point model of the kite [62]. The ground station dynamics are also taken into account. A Matlab [67] implementation of kitesim has been made by S. Rapp.

AWE-box is a tool written for solving optimal control problems for multi-kite AWE systems. It uses a Lagrangian formalism in combination with the CASADI software [9] to solve optimal control problems. The software has been recently released. CASADI has bindings to solvers such as Sundials' CVodes [8][47], and formulates the necessary Jacobian information through algorithmic differentiation (AD). AWE-box does not make use of these integrators but uses a integration method where physicality and optimality are solved simultaneously. For this reason AWE-box is not usable for our purpose, since controls are prescribed.

Table 2.7: An overview of available multibody dynamics toolboxes. * = particle dynamics toolbox. CLI = command line interface, IF = input file, F = Fortran, P = Python.

Name	Language	Latest release	Open source	Source
MSC Adams	F, C++		Proprietary	[92]
MBDYN	CLI, IF	2017-10-15	yes	[65]
Project Chrono	C++, P	2019-02-22	yes	[94]
PhysX	C++	2018-12-20	yes	[75]
Flex*	C++	2018-07-20	yes	[74]
Open Dynamics Engine	C++, P	2019-02-23	yes	[91]
Bullet	C++, P	2019-02-19	yes	[26]
Dart	C++, P	2019-02-19	yes	[61]

Kitepower makes use of the quasi-steady model for it's simulations. At every time step, the solving the quasi-steady equilibrium results in a tether force and a set of velocities. Then, Euler integration is applied to determine the next position from its current position in combination with the found velocities. The simulation is written in Python and includes the dynamics of the ground station.

Nvidia FleX is a particle based real-time simulation technique [64] developed by NVIDIA. It uses the semi-implicit Euler method for integration in combination with position-based dynamics [70].

MBDyn is a multibody dynamics simulation software tool. It provides it's software as packages (pre-compiled), however it's source is public as well. The software allows the user to construct a dynamical system via an input file, specifying (among other things) dimensions, degrees of freedom and inertias. Additionally it allows the user to provide integrator settings such as time step and tolerance.

MSC Adams, MBDYN, Project Chrono, Nvidia Physx, Bullet, Dart, ODE are are all multibody dynamics engines. Some more sophisticated than others, even with finite element tools included. Of all the simulation tools tabulated in Table 2.7, MSC Adams is the only proprietary (non-free) software.

2.4. Thesis Goal and Approach

2.4.1. Goal

The goal of the master thesis is as follows:

"*What are the effects of mass and drag of the kite control unit on the flight behavior of a flexible airborne wind energy system kite during flight?*"

With the additional goal:

"*To provide Kitepower with a model and method that allows the use of experimental flight data for system identification*"

2.4.2. Motivation

For many reasons such as system power output estimation, controller design and software testing, the dynamical behavior of airborne wind energy (AWE) systems such as deployed by Kitepower require system modeling and simulation. Different approaches exist to model kite flight behavior, ranging from black-box models such as the turning rate law, to point mass models with rolling lift vectors and models relying on fluid-structure interactions.

Regarding the steering of leading edge inflatable kites (LEI) kites, the steering is thought to be caused by a warping induced yaw [84]. It is hypothesized that kite roll caused by the outward motion of the KCU due to centrifugal forces positively contribute to the steering. Additionally, it has been observed in experimental flights that added drag induced by an on-board turbine reduces the angle of attack of the kite. The aerodynamic drag of the KCU might play a role in the hypothesized outward motion as well.

Oftentimes the mass of the KCU is not taken into account when modeling these AWE systems, whereas some models include the mass, but ignore aerodynamic drag. Reports exists of models that show correspondence of the model including KCU mass with experimental flight data, but no reports exist that explicitly quantify the effects of the mass and drag of the KCU. Therefore the effect of mass and aerodynamic drag of the KCU on the flight behavior of the kites requires investigation.

2.4.3. Approach

It is assumed that answering the research questions requires performing simulations on computers, since flight experiments can be expensive and no control exists over the environment. Existing simulation environments cannot be used due to legacy code, limited validity or unsuitable model complexity. A rigid body kite model with a flexible variable length tether is to be used since this provides the most realistic flight behavior given the real-time requirement following from the controller integration step. Of the two suitable rigid body kite models, one is implemented in the simulation environment which is described in chapter 3. Additionally a tether and ground station model are implemented in the simulation environment as well.

After the model implementation, the Kitepower ground station controller and flight controller are integrated. The use of the controllers provided by Kitepower is required to be able to more easily extrapolate the findings from the simulations to reality. The kite, tether and groundstation models as well as the groundstation controller are discussed in chapter 4.

For the experiments the goal is to use a model that has been fitted to experimental (real) flight data in order to provide more validity to any conclusion coming from the research. Since the experimental flight data required to perform system identification is unavailable the parameters of the two rigid body kite models have been identified through the use of simulated flight data in chapter 5. This provides

Kitepower with a method to identify the parameters of the two models with experimental flight data in the future.

After the system identification several experiments will be be performed where the mass and drag of the KCU as well as the mass of the kite will be increased independently under two different wind conditions. Once the experiments have been performed an analysis will be held followed by a discussion of the findings. A description of the experiments and intermediate conclusions can be found in chapter 6.

Finally, in chapter 6, an overview will be given of the most important conclusions from the experiments and recommendations will be made based on the experiments and other findings during the research.

3

Simulation Framework

This chapter provides a top-level description of the implemented simulation framework without going into the details of the individual component dynamics. First, a selection of a suitable multibody dynamics engine will be performed. Afterward the software architecture will be discussed.

3.1. Multibody Dynamics Simulation Engine Selection

This section will discuss the selection of a suitable multibody physics engine (as discussed in subsection 2.3.2), starting with the reason for using such an engine, followed by a list of criteria and finally listing the reasons for selecting Nvidia PhysX [75].

Several kite simulation packages exist (subsection 2.3.2). Some of them are outdated, use an inappropriate kite and tether model or do not meet the requirements below. Therefore it was deemed necessary to build an AWE kite simulation that does meet the requirements. Furthermore, keeping in mind limited time, performance and possible continuation of this work, a multibody physics simulation engine will be used that performs all calculations that describe all motions and interactions of the system components.

In order to be able to use the flight controller provided by Kitepower, the simulation needs to be able to run as fast or faster than real-time. Whether real-time performance is achievable cannot be known beforehand, however this requirements serves as a crude filter. Since the author has experience with Python and C++ this is made a requirement due to the limited available time and the knowledge that this requirement will very likely not be a limiting factor. Kitepower required the whole project to be open source, this includes the dynamics engine. In order to be able to simulate a flexible reelable tether according to the model described in Table 2.3.1, it is required to be able to add and remove elements during the simulation [1]. Inbuilt visualization is a plus since this will accelerate error identification and debugging. The above requirements are summarized in the following list:

- Real time capable;
- Language: Python or C++;
- Open source;
- Addition and removal of elements during simulation.
- [+]Visualization possible;

Of the multibody dynamics simulation engines listed in Table 2.7 , Nvidia PhysX [75] has been selected based on the fact that is meets all criteria and that an example [110] has been encountered which showed the possibility of the addition and removal of elements of a flexible cable. An added benefit was be that if the real-time performance was below the requirement, hardware acceleration (through the use of the graphics card) could possibly improve the simulation speed.

[1] Due to issues encountered during implementation it has been decided not to add or remove elements, but to vary the length of the first element as discussed in section 4.2

In order to built trust in the physical correctness of the Nvidia PhysX, an experiment has been performed in Appendix J. In this experiment a compound pendulum is swung with a low amplitude. The measured frequency shows an error of (0.1007%) from the expected frequency, which is though to be sufficiently small to trust the physical correctness of the physics simulation engine.

3.2. Description of Total Simulation Framework

The structure of the total simulation framework, including physics simulation, flight path control, visualization and aerodynamics will be laid out in this section. Details of the winch, kite, KCU and tether models can be found in their respective sections in chapter 4. The software architecture will be explained using Figure 3.1. Table 3.1 shows several key characteristics of the simulation framework.

Table 3.1: Key characteristics of the simulation framework.

Language	C++
Linear solver	Temporal Gauss-Seidel
Integration method	semi-implicit Euler
Simulation time step	0.001 [s]
Data output and visualization frequency	20 [Hz]

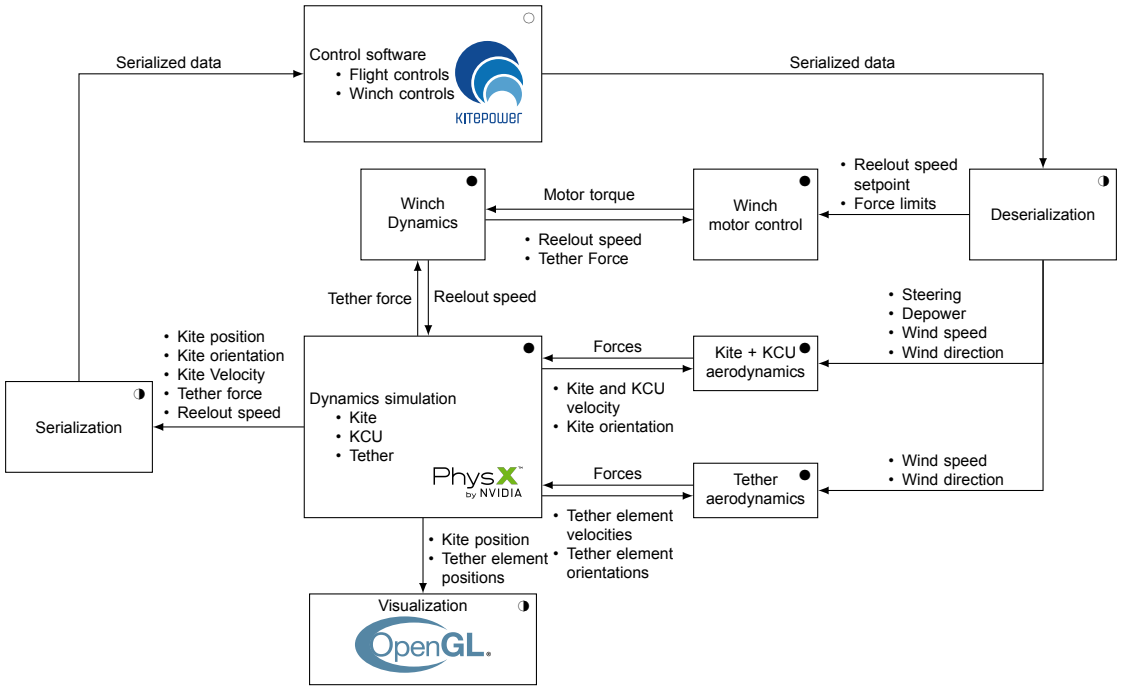

Figure 3.1: Software architecture for the total simulation framework. Blocks show functionalities, lines are directional and indicate information flows. Text above or next to lines show what information is transported. The symbols ●, ◑ and ○ indicate the different execution frequencies.

The uppermost block consists of software provided by Kitepower. It consists of a suite of software that together determines the control commands for the kite and groundstation. Their software sends and receives serialized data over socket connections. The serialization and deserialization blocks take care of the packing, unpacking, sending and receiving of messages. Google protocol buffers [1] are used for the serialization of messages and ZeroMQ [2] is used for the socket connections. All blocks except the Kitepower software block is compiled to one executable.

The unpacked reeling velocity setpoint and force limits are sent to the winch motor controller. The winch motor controller translates the setpoints to motor torques, depending on the current tether force and reelout speed. The motor torques are then applied in the dynamical winch model which in combination

with the winch dynamics and the tether force results in a reelout speed. The reelout speed is in turn returned to the dynamics simulation block.

The steering and depower setpoints are used in combination with the wind, kite velocity and kite orientation to determine the aerodynamic forces. The state of the kite which is retrieved from the dynamic simulation block. Tether aerodynamics are not influenced by any control signal and depend only on the tether element velocities and the wind.

The dynamic simulation block takes the external aerodynamic forces for the kite, KCU and tether. Additionally it receives the reelout speed from the winch dynamics block. It calculates the resulting positions, orientations and velocities of the kite, KCU and tether elements at the next timestep, including the tether force. The required information is then forwarded to the visualization and serialization blocks.

Real time implementation The different blocks in Figure 3.1 have different execution frequencies. The different levels are indicated by the symbols ●, ◑ and ○. The software provided by Kitepower (○) sends control signals at a rate of 20 [Hz]. The serialization, deserialization and visualization also operate at 20 [Hz] (◑). The Kitepower software is a separate process, therefore synchronization cannot be guaranteed (and therefore they are assigned different symbols). Finally all other processes (●) run at 1000 [Hz]. The way in which real-time performance and synchronization is ensured is by performing the following sequence at a rate of 20 [Hz]:

$$50 \times \bullet$$
$$1 \times ◑$$
$$1 \times \text{Pause}$$

The duration of the pause is determined by the difference between the total simulated time and the total process run time.

4

Description of the Implemented AWE System Component Models

In this chapter the details of the used component models will be discussed, starting with the kite models including a aerodynamic verification of the implementation and model adjustments for system identification. After the kite models, the tether, groundstation and KCU models will be discussed.

4.1. Kite Model

Four types of rigid body models have been identified in literature: Ruppert's, Knappskog's, Williams' and Breukels'. A side-by-side comparison can be found in Table G.1. A fifth rigid body model can be derived from Fechner's four point model. This section briefly discusses the rigid body model structure, followed by the specifics for Ruppert's and Fechner's model. Kite model parameters can be found in Table F.1.

The kite rigid body linear and angular accelerations are functions of the aerodynamic, tether and gravitational forces and torques. Two sets of equations can be constructed, one for the linear and one for the angular accelerations (Equation 4.1). Subscripts $*_G$ (global/inertial) and $*_K$ (local/kite) indicate the frame of a vector. An overview of all subscript, superscript and other notations amongst several frame definitions can be found in Appendix F.

$$\begin{aligned} m\mathrm{I}\ddot{\mathbf{x}}_G &= \mathbf{F}_G^a + \mathbf{F}_G^t + \mathbf{F}_G^g \\ \mathrm{J}_k\dot{\boldsymbol{\omega}}_k + \boldsymbol{\omega}_k \times \mathrm{J}_k \cdot \boldsymbol{\omega}_k &= \mathbf{T}_G^a \\ \ddot{\mathbf{x}}_G &= \left[\ddot{x}_G, \ddot{y}_G, \ddot{z}_G\right]^T \\ \dot{\boldsymbol{\omega}}_k &= \left[\dot{p}_k, \dot{q}_k, \dot{r}_k\right]^T \end{aligned} \tag{4.1}$$

Here $\mathbf{x}$ is the position vector consisting of the x, y and z coordinates in the global frame. The angular velocity vector $\boldsymbol{\omega}$ consists of the individual angular velocity components p, q and r in the kite frame. $\mathbf{F}$ and $\mathbf{T}$ represent forces and torques respectively.

The translational inertia matrix is obtained by multiplying the kite mass (m) with an identity matrix (I). The mass of the kite is a known quantity, it can be measured with minimal means. The inertia tensor (J) has been determined through 3D drawings and material properties of the kite in Appendix H and is shown in Equation 4.2:

$$\mathrm{J}_k = \begin{bmatrix} 84.79 & 0.00 & 0.66 \\ 0.00 & 13.23 & 0.00 \\ 0.66 & 0.00 & 83.01 \end{bmatrix} \tag{4.2}$$

In Equation 4.1 the tether force ($\mathbf{F}_G^a$) and gravitational force ($\mathbf{F}_G^g$) are assumed to be known. This assumption is valid, since in practice these can be determined or derived with relative ease and accuracy. In order to solve for the linear and angular accelerations ($\ddot{\mathbf{x}}$, $\dot{\boldsymbol{\omega}}$), a model is required for the aerodynamic forces ($\mathbf{F}_G^a$) and torques ($\mathbf{T}_G^a$).

Unlike Ruppert's and Knappskog's aerodynamic models, Williams' and Breukels' models' steering input depend on the displacement of the bridle attachment points on the tips of the kite. This steering method is very different from the steering method used by Kitepower, therefore these two aerodynamic models are not suitable.

Ruppert's and Knappskog's models show many similarities. In terms of the aerodynamic parameters C_L, C_D and C_S, Ruppert's model is more flexible. Due to the similarities and added flexibility, only Rupperts model will be considered of the two. Fechner's four point particle model can be cast into a rigid body representation. In the following sections, Ruppert's and Fechner's aerodynamic models will be discussed in more detail.

4.1.1. Ruppert's Kite Model

In this section a variation of Ruppert's model will be discussed. It is identical to Ruppert's model, but without the gravity induced torque (since no parameter estimate is given in Ruppert's report). For this model (Equation 4.3), the aerodynamic force is the sum of the aerodynamic lift, drag and side force components. The total aerodynamic torque is the sum of the individual components around the kite's local axes.

$$\begin{aligned} \mathbf{F}_G^a &= \mathbf{F}_G^{a,L} + \mathbf{F}_G^{a,D} + \mathbf{F}_G^{a,S} \\ \mathbf{T}_k^a &= \mathbf{T}_k^{a,x} + \mathbf{T}_k^{a,y} + \mathbf{T}_k^{a,z} \end{aligned} \tag{4.3}$$

With:

$$\mathbf{F}_G^{a,L} = 0.5\rho \mathbf{v}_a^2 A_{k,t} C_a^{L,F} \mathbf{e}_G^L \qquad \mathbf{F}_G^{a,D} = 0.5\rho \mathbf{v}_a^2 A_{k,t} C_a^{D,F} \mathbf{e}_G^D \qquad \mathbf{F}_G^{a,S} = 0.5\rho \mathbf{v}_a^2 A_{k,t} C_a^{S,F} \mathbf{e}_G^S$$

$$\mathbf{T}_k^{a,x} = 0.5\rho \mathbf{v}_a^2 A_{k,t} C_k^{x,T} b \mathbf{e}_k^z \qquad \mathbf{T}_k^{a,y} = 0.5\rho \mathbf{v}_a^2 A_{k,t} C_k^{y,T} \bar{c} \mathbf{e}_k^y \qquad \mathbf{T}_k^{a,z} = 0.5\rho \mathbf{v}_a^2 A_{k,t} C_k^{z,T} b \mathbf{e}_k^z$$

Note that in the literature often the superscripts (or subscripts) l, m and n are used for the torques around the x, y and z-axes respectively. In this report x, y, and z will be used, resulting in a more consistent notation throughout this report. Figure 4.1 shows the definition of the kite axes. The above forces and torques depend on the following nondimensional aerodynamic coefficients:

$$C_a^{L,F} = C_L(\alpha) \qquad C_a^{D,F} = C_D(\alpha) \qquad C_a^{S,F} = \text{sgn}(\beta)\frac{A_{k,s}}{A_{k,p}} C_S(|\beta|) \tag{4.4}$$

$$C_k^{x,T} = 0 \qquad C_k^{y,T} = 0 \qquad C_k^{z,T} = C_{z,\delta_s}\delta_s + C_{z,\beta}\beta + C_{z,r}\frac{br}{|\mathbf{v}_a|} \tag{4.5}$$

Forces and torques in the aerodynamic and local kite frame can be converted to the global frame through a transformation of coordinates (Appendix F). $A_{k,t}$ is the projected surface area of the kite on the local xy plane, where 't' stands for top. $A_{s,t}$ is the projected surface area of the kite on the local xz plane and 's' stands for side. For this model the side force coefficient is identical to the lift force coefficient ($C_S(x) = C_L(x)$). The aerodynamic coefficients depend on the angle of attack (α) and sideslip angle (β) which are defined in Appendix D. $C_L(\alpha)$ is shown on the left in Figure 4.2, whereas $C_D(\beta)$ is shown on the right. The coefficient of the yaw torque consists of three components of which the coefficients are listed in Table 4.1.

The kite model has two control inputs: steer (δ_s) and depower (δ_d). The steering input provided by Kitepower lies in the range [-100,100] and is scaled linearly such that $\delta_s \in$ [-1,1]. The depower lies in the range $[0, \delta_d^{max}]$ and is scaled to a depower offset α_d such that $0 \leq \delta_d \leq \delta_d^{max} \rightarrow \alpha_d^{min} \leq \alpha_d \leq \alpha_d^{max}$. Where α_d^{min} and α_d^{max} are the minimal and maximal pitch offset caused by the depower. Values for δ_d^{max}, α_d^{min} and α_d^{max} can be found in Table F.1. For nominal flight, $40 < \delta_d < 45$. The pitch is reflected in the angle of attack used for the calculation of the aerodynamic coefficients such that $\alpha = \alpha^* - \alpha_d$, where α^* is the angle of attack determined in the kite frame. The depower-pitch parameters have been

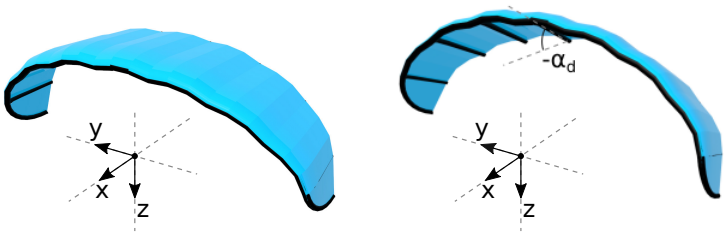

Figure 4.1: Definition of the kite frame left). Negative kite pitch with respect to the kite frame (right).

Table 4.1: C_{z,δ_s} is different from the one in [84] to allow for steering in low wind conditions. $C_{z,\beta}$ and $C_{z,r}$ are identical to [84].

Coefficient	Value [-]	Description
C_{z,δ_s}	0.080	Steering sensitivity
$C_{z,\beta}$	0.091	Sideslip restorative torque
$C_{z,r}$	-0.018	Yaw rate damping

tuned manually. The identification of the relation between depower and the effect on the aerodynamic coefficients is part of the recommendations. Figure 4.1 shows the definition of the kite frame and kite depower pitch offset. The angle of attack and sideslip generally take on the following values: $5° < \alpha < 25°$, $-15° < \beta < 15°$ (Figure 5.4).

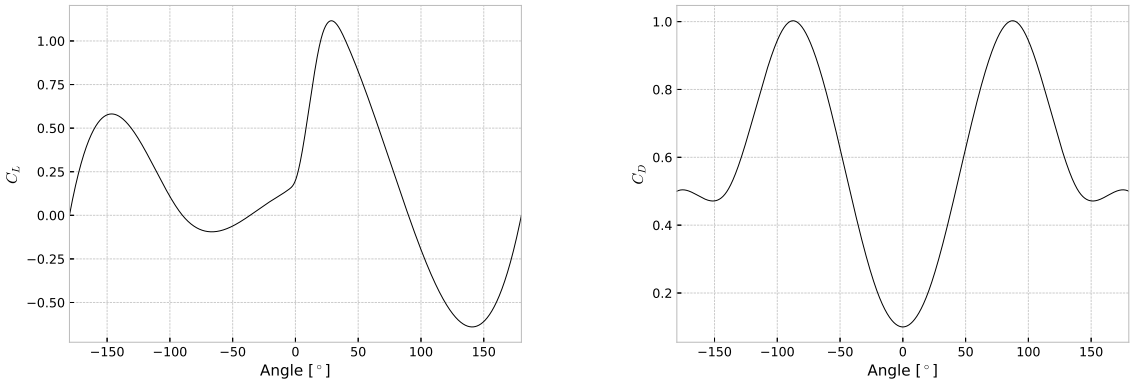

Figure 4.2: Lift (left) and drag (right) curve.

Where Ruppert's model is chosen for its more advanced and flexible aerodynamic model, this model now need to be simplified in order to later be able identify the aerodynamic lift, drag and side force coefficient curves during system identification. Therefore a parametrization is required such that the parameters can be identified through linear regression. This parametrization will be used in chapter 5. For the simulation of the kite, the curves from Figure 4.2 will be used for the aerodynamic coefficients. The equations below show Ruppert's reparametrized aerodynamic model.

$$
\begin{aligned}
C_L^\alpha &= C_{L,0}^\alpha + C_{L,1}^\alpha \alpha + C_{L,2}^\alpha \alpha^2 + C_{L,3}^\alpha \alpha^3 \\
C_D^\alpha &= C_{D,0}^\alpha + C_{D,1}^\alpha \alpha + C_{D,2}^\alpha \alpha^2 + C_{D,3}^\alpha \alpha^3 \\
C_S^\beta &= \frac{A_{k,s}}{A_{k,p}} \left(\text{sgn}(\beta) C_{S,0}^\beta + C_{S,1}^\beta \beta + \text{sgn}(\beta) C_{S,2}^\beta \beta^2 + C_{S,3}^\beta \beta^3 \right) \\
C_k^{z,T} &= C_z^{\delta_s} \delta_s + C_z^\beta \beta + C_z^r \frac{br}{\|\mathbf{v}_a\|}
\end{aligned}
\tag{4.6}
$$

4.1.2. Fechner's Kite Model

In this section the results for the derivation of Fechner's model in a rigid body model description are discussed. The complete derivation can be found in Appendix K. The model consists of five points (Figure 4.3) with a predetermined mass distribution. A lift and drag force acts on three of these points (0, 1 and 2). The connection between the particles is rigid, therefore the kite behaves like a rigid body. The rigid body model is derived via the underlying principle that the total aerodynamic force is the sum of the individual contributions of the forces at the sides and top, and the total aerodynamic torque is the sum of the cross products of these forces with their respective position with respect to the center of mass.

The three points with a lift and drag force appear as six column vectors in Equation 4.7 (and six rows in $\mathbf{C}$). The B, C and D subscripts in the angle of attack α_* stand for locations 0, 1 and 2 respectively (Figure 4.3).

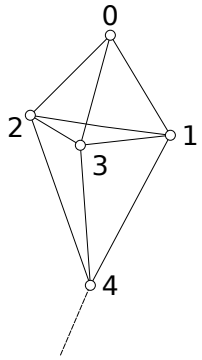

Figure 4.3: 5 point kite model [38]. Aerodynamic forces act on points 0, 1 and 2.

$$
\begin{aligned}
F_G^a &= \frac{1}{2}\rho \begin{bmatrix} \mathbf{v}_{00} & \mathbf{v}_{01} & \mathbf{v}_{02} & \mathbf{v}_{03} & \mathbf{v}_{04} & \mathbf{v}_{05} \end{bmatrix} \cdot \mathbf{C} \\
T_G^a &= \frac{1}{2}\rho \begin{bmatrix} \mathbf{v}_{06} & \mathbf{v}_{07} & \mathbf{v}_{08} & \mathbf{v}_{09} & \mathbf{v}_{10} & \mathbf{v}_{11} \end{bmatrix} \cdot \mathbf{C} \\
\mathbf{C} &= \begin{bmatrix} C_L(\alpha_B, \delta_D) \\ C_L(\alpha_C, \delta_D) \\ C_L(\alpha_D, \delta_s, \delta_D) \\ C_D(\alpha_B, \delta_s, \delta_D) \\ C_D(\alpha_C, \delta_s, \delta_D) \\ C_D(\alpha_D, \delta_s, \delta_D) \end{bmatrix}
\end{aligned}
\tag{4.7}
$$

The vectors $\mathbf{v}_{00}$ through $\mathbf{v}_{11}$ take on the shapes as shown in Equation 4.8. In the example below, $\mathbf{v}^2$ is a squared velocity vector, A is an area, $\mathbf{e}_G$ is a unit direction vector, $\mathbf{r}$ is a vector that describes the position of the applied force with respect to the center of mass of the kite.

$$
\begin{aligned}
\mathbf{v}_{00-05} &= \mathbf{v}_G^2 A \mathbf{e}_G \\
\mathbf{v}_{06-11} &= \mathbf{r}_G \times \mathbf{v}_{00-05}
\end{aligned}
\tag{4.8}
$$

The three position vectors $\mathbf{r}_G^0$, $\mathbf{r}_G^1$ and $\mathbf{r}_G^2$ are fixed, however they need to be determined beforehand based on the location of the center of mass. Therefore the location of center of mass needs to be identified. The width (distance between points 1 and 2) and height (shortest distance between point 0 and the line connecting points 1 and 2) of the kite are fixed. In [38] a mass distribution has been proposed, however this mass distribution results in an inertia tensor that does not correspond to the one determined in Appendix H. The mass distribution and relative positions of points 0,1 and 2 have been determined through solving a set of equations in Appendix L. The results are shown below in Equation 4.9.

$$\begin{aligned}\mathbf{r}_B &= \begin{bmatrix}-0.9107 & 0.0000 & -2.4626\end{bmatrix}^T \\ \mathbf{r}_C &= \begin{bmatrix}-0.6564 & 4.1150 & 0.6571\end{bmatrix}^T \\ \mathbf{r}_D &= \begin{bmatrix}-0.6564 & -4.1150 & 0.6571\end{bmatrix}^T\end{aligned} \tag{4.9}$$

The vector elements of $\mathbf{C}$ in Equation 4.8 map a resultant angle of attack α to a nondimensional aerodynamic coefficient. Each resultant angle of attack is constructed from the local angle of attack (α_*), the steering input (δ_s) and the depower input (δ_D). The same lift and drag curves are used for this model as Figure 4.2. The relation between the resultant angle of attack (α), local angle of attack, depower and steering input is partly nonlinear and made the model structure unsuitable for system identification through linear regression. Therefore an alternative aerodynamic model structure for this model is proposed, where each aerodynamic coefficients depends up to the second order on the local angle of attack, depower and steering input (Equation 4.10).

$$\begin{aligned}C_L^B(\alpha_B, \delta_D) &= C_0^{L,t} + C_1^{L,t}\alpha_B + C_2^{L,t}\alpha_B^2 + C_3^{L,t}\delta_D + C_4^{L,t}\delta_D^2 \\ C_D^B(\alpha_B, \delta_D) &= C_0^{D,t} + C_1^{D,t}\alpha_B + C_2^{D,t}\alpha_B^2 + C_3^{D,t}\delta_D + C_4^{D,t}\delta_D^2 \\ C_L^C(\alpha_C, \delta_s, \delta_D) &= C_0^{L,s} + C_1^{L,s}\alpha_C + C_2^{L,s}\alpha_C^2 + C_3^{L,s}\delta_s + C_4^{L,s}\delta_s^2 + C_5^{L,s}\delta_D \\ C_D^C(\alpha_C, \delta_s, \delta_D) &= C_0^{D,s} + C_1^{D,s}\alpha_C + C_2^{D,s}\alpha_C^2 + C_3^{D,s}\delta_s + C_4^{D,s}\delta_s^2 + C_5^{D,s}\delta_D \\ C_L^D(\alpha_D, \delta_s, \delta_D) &= C_0^{L,s} + C_1^{L,s}\alpha_D + C_2^{L,s}\alpha_D^2 - C_3^{L,s}\delta_s + C_4^{L,s}\delta_s^2 + C_5^{L,s}\delta_D \\ C_D^D(\alpha_D, \delta_s, \delta_D) &= C_0^{D,s} + C_1^{D,s}\alpha_D + C_2^{D,s}\alpha_D^2 - C_3^{D,s}\delta_s + C_4^{D,s}\delta_s^2 + C_5^{D,s}\delta_D\end{aligned} \tag{4.10}$$

4.1.3. Aerodynamic Model Verification

In this section two experiments have been performed in order to check the correct implementation of the aerodynamic lift and drag force. In the first experiment the lift-over-drag ratio is varied while the angle of attack is kept constant. In the second experiment the depower pitch (α_d) is slowly increased in order to test a wide range of angles of attack. For both experiments, the resulting elevation angle is compared with the expected elevation angle. The wind profile in the simulation environment is flat, meaning that the wind speed is the same at every altitude.

In the first experiment a point mass kite is rigidly attached to a straight tether. The kite has no angle of attack, C_L/C_D is fixed. For each C_L/C_D, the kite is given 30 seconds to settle. The expected elevation angle is determined through Equation 4.11. The results are shown in Figure 4.4 on the left.

$$\begin{aligned}\beta &= \text{atan}\sum F_z / \sum F_x \\ \sum F_x &= 0.5\rho C_l v_a^2 A \\ \sum F_z &= 0.5\rho C_d v_a^2 A - mg \\ C_D &= (C_l/C_d)^2 + 1 \\ C_l &= \sqrt{C_r - C_d^2} \\ C_r &= 1\end{aligned} \tag{4.11}$$

In the second experiment the kite is again rigidly attached to a straight tether. The orientation of the kite now does contribute to the angle of attack, therefore influencing the lift and drag coefficients. Throughout the experiment, the depower pitch α_d is slowly increased in 30 second intervals to allow the kite to settle. The results for experiment 2 are shown Figure 4.4 on the right. The expected elevation angle is determined recursively as follows:

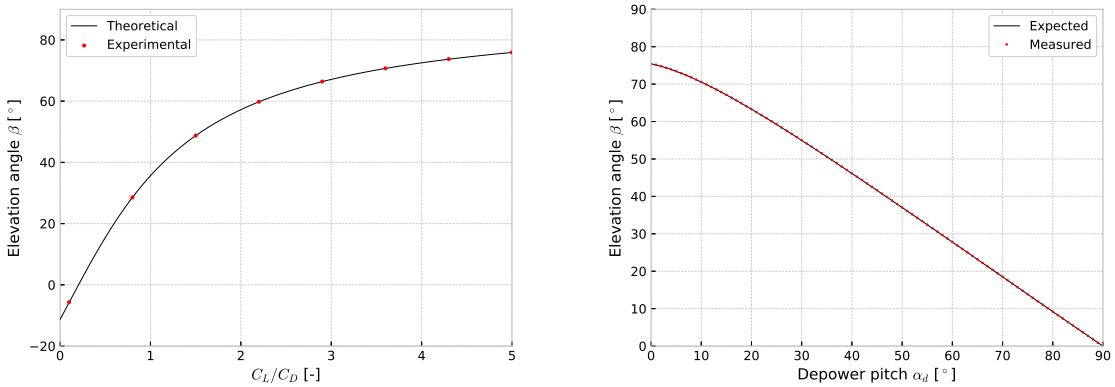

Figure 4.4: Left: Resulting elevation angle for several fixed L/D values from experiment 1. Right: results for experiment 2.

1. Assume the initial elevation angle: $\beta[k=0]=90$
2. Determine the corresponding angle of attack: $\beta[k] \rightarrow \alpha[k]$
3. Lookup the corresponding aerodynamic coefficients $C_L(\alpha[k]), C_D(\alpha[k])$
4. Determine the expected aerodynamic forces: F_L, F_D.
5. Evaluate the expected elevation angle: $F_L, F_D \rightarrow \beta[k+1]$.
6. If $\beta[k]-\beta[k-1]<\epsilon$: stop, else: return to step 2.

4.1.4. Model Alterations for System Identification

Several model alterations are discussed in this section which enable the system identification at a later stage. The model alterations are based on the assumption that the KCU is rigidly connected to the center of mass of the kite. This assumption is based on the observation that during flight, the bridle is always under tension and therefore the location of the KCU is constrained to the kite which has already been assumed to be rigid. Figure 4.5 shows how the kite, KCU and tether are connected.

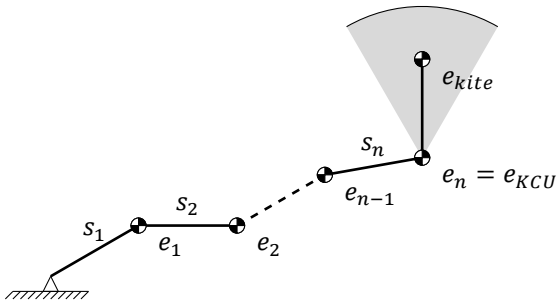

Figure 4.5: Schematic of the connections between the system components, including kite and KCU.

Equation 4.12 shows the updated equation for the kite forces and torques acting on the kite (based on Equation 4.1). $\mathbf{F}_G^T$ is now measured through the constraint that connects the kite to the KCU, which is located at the origin of the KCU. In addition to the tether forces it also measures the forces resulting from the KCU accelerations acting on the kite. Two additional torque terms are incorporated: $\mathbf{T}_G^T$ which is the constraint torque, and $\mathbf{r} \times \mathbf{F}_G^T$ which is the torque resulting from the tether force $\mathbf{F}_G^t$ which is not aligned with the center of mass of the kite. $\mathbf{r}$ is the vector pointing from the center of mass of the kite towards the KCU and is defined as a unit vector along the local z-axis of the kite, multiplied with the bridle length $\mathbf{r} = r_b \mathbf{e}_z^k$ (Figure L.1).

$$
\begin{aligned}
m\mathrm{I}\ddot{\mathbf{x}} &= \mathbf{F}_G^a + \mathbf{F}_G^t + \mathbf{F}_G^g \\
\mathrm{J}_k\dot{\boldsymbol{\omega}}_k + \boldsymbol{\omega}_k \times \mathrm{J}_k \cdot \boldsymbol{\omega}_k &= \mathbf{T}_G^a + \mathbf{T}_G^t + \mathbf{r} \times \mathbf{F}_G^t
\end{aligned}
\tag{4.12}
$$

4.2. Tether Model

This section describes the tether model that has been implemented in the simulation framework. First, a global description will be given of the tether model. Secondly, the aerodynamics of the tether elements will be discussed, followed by an explanation of the reeling implementation. Finally the dynamic implementation will be covered.

The tether consists of a series of interconnected rigid bodies. The distances between the bodies are fixed and the connection between the bodies is flexible through the use of a joint where all rotational axes are free to move. Reeling is performed through the control of a distance constraint between the first tether element and the origin. The last tether element is the one attached to the KCU.

The masses of each tether element are defined as follows (Equation 4.13):

$$
m_e = \begin{cases} \rho l_{s_n} + 1/2\rho l_{s_{n+1}} & \text{for } n = 1 \\ \rho l_{s_n} & \text{for } 1 < n < n_{max} \\ 1/2\rho l_{s_n} & \text{for } n = n_{max} \end{cases}
\tag{4.13}
$$

Here l_{s_n} is the length of the nth tether segment and ρ_t the linear density of the tether (Table F.2). Since all tether elements are implemented as rigid bodies, an inertia tensor needs to be associated with each element. Since in a lumped-mass tether model the rotational inertia of each element is zero, a rotational inertia for each element is set to be small (but nonzero). The inertia of each element is equal to the inertia of a uniform sphere with a diameter of $d = 0.1$ [m] with a mass equal to the element's mass.

A distinction is made between tether segments and elements. A tether element is a rigid body element, whereas a tether segment is the connection between the tether elements. The numbering of the elements and segments is such that the first tether segment connects the first tether element to the groundstation and the second tether segment connects the tether elements one and two (Figure 4.6).

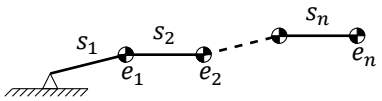

Figure 4.6: Numbering of tether elements (e_*) and segments (s_*).

The aerodynamic drag of the first segment is determined differently than for the other elements. The drag of the first segment (s_1) is applied directly to the first element (e_1). The drag of the first element (Equation 4.14) is based on the analytical result of Equation 2.22 and by using the perpendicular apparent velocity instead.

$$
\begin{aligned}
\mathbf{F}_{d,s_1} &= 1/8\rho l d C_D^t \|\mathbf{v}_a^\perp\| \mathbf{v}_a^\perp \\
\mathbf{v}_a^\perp &= \mathbf{v}_{a,1} - \mathbf{v}_{a,1} \cdot \mathbf{e}_{t,1} \\
\mathbf{e}_{t,n} &= \mathbf{p}_{t,1} - \mathbf{p}_{t,0} \\
\mathbf{p}_{t,0} &= [0,0,0]^T
\end{aligned}
\tag{4.14}
$$

$\mathbf{v}_a^\perp$ is the apparent velocity perpendicular to the nth tether segment, perpendicular to the first tether segment. $\mathbf{p}_{t,n}$ is the position of the nth tether element. $\mathbf{e}_{t,n}$ is the unit vector pointing from element e_n to e_{n-1}. The tether drag coefficient is $C_D^t = 0.96$ [38].

For the following tether segments ($s_{n>1}$) we have the following expression [103]:

$$\bar{\mathbf{v}}_{a,n} = (\mathbf{v}_{a,n-1}\mathbf{v}_{a,n})/2 \tag{4.15}$$

$$\mathbf{F}_{d,s_n} = 1/2\rho l d C_D^t \|\bar{\mathbf{v}}_{a,n}^{\perp}\| \bar{\mathbf{v}}_{a,n}^{\perp} \tag{4.16}$$

This force gets distributed over the neighboring tether elements, resulting in the following expression for the force per tether element:

$$F_{d,e_n} = \begin{cases} F_{d,s_n} + 0.5F_{d,s_{n+1}} & \text{for } n = 1 \\ 0.5F_{d,s_n} + 0.5F_{d,s_{n+1}} & \text{for } 1 < n < n_{max} \\ 0.5F_{d,s_{n+1}} & \text{for } n = n_{max} \end{cases} \tag{4.17}$$

The parameters used for this tether model can be found in Table F.2. In subsection 2.3.1 it was found that no more than 10 elements are required to capture the tether shape within a 5% error and no more than 20 elements are required to accurately model the tether drag, therefore the tether will consist of 20 segments.

Initially the goal was to implement a reeling method with a variable amount of tether elements as described. The implementation was troublesome and therefore an alternative reeling method has been employed. In this reeling method, the length and the change in length over time of the first segment (s_1) are used as constraints. The constraint force is determined by Nvidia Physx, the constraint stiffness and damping are parameters that can be used to tune the constraint behavior. The stiffness is $k = 1e^{10}$ [Nm^{-1}] and the damping is $\xi = 1e^{6}$ [Nsm^{-1}]. Since no tether elements can be removed or added, the minimal length of the first segment is as least the required length that is reeled in and out each cycle.

The connections between the individual tether elements and the KCU are ensured through the use of a minimal coordinate Lagrangian description. The connection of the first element to the ground-station as well as the connection between the kite and KCU use a Newtonian constraint, this makes it possible to query the constraint force.

The static behavior of the tether model has been verified in section I.1 by comparing the tether with the catenary curve. The maximum positional error found was 0.11%. The drag of the tether has been verified in section I.2.

4.3. KCU Model

This section shortly describes the model employed for the simulation of the KCU. The KCU model consists of two components, namely a dynamic and an aerodynamic model.

The KCU is modeled as a point mass, therefore it carries no rotational inertia. The KCU dynamics are incorporated in the tether model by the addition of the mass of the KCU to the mass of the last tether element such that $m_{e,n_{max}} = 1/2\rho l_{s_n} + m_{KCU}$ in Equation 4.13. The mass of the KCU, among other parameters, is tabulated in Table F.3.

The KCU aerodynamic model only knows drag, no lift or side forces are applied. The drag of the KCU is independent of the angle of attack and sideslip and is defined as follows:

$$F_{D,KCU} = 1/2\rho \mathbf{v}_a^2 C_D A_{KCU} \hat{\mathbf{v}}_a \tag{4.18}$$

The drag coefficient (C_D) has been based on a value often found for cubes (1.05) facing the flow with a flat face. The frontal surface area has been determined through the use of technical drawings, with the assumption that the onboard turbine blades simply add to the total surface area.

4.4. Groundstation Model

In this section the groundstation model and controller will be discussed. A groundstation model was required since during simulation it was found that the direct application of the reeling velocities led to large tether force peaks. The groundstation model (Equation 4.19) and controller are based on [17]. The groundstation controller uses velocity setpoints provided by Kitepower. The groundstation dynamics model the drum radial acceleration ($\dot{\omega}$ [rad/s^2]) as a function of the total applied torque (T_a [Nm]) and the drum's moment of inertia (J). The total applied torque is the sum of the tether force (F_t [N]) times the drum radius (r) minus a friction coefficient (c_w) times the radial velocity (ω [rad/s]) minus the gearbox ration (k) times the motor torque (T_m [Nm]) as shown in Equation 4.19.

$$\begin{aligned} \dot{\omega} &= T_a/J \\ T_a &= F_t \cdot r - c_w \cdot \omega - k \cdot T_m \end{aligned} \tag{4.19}$$

The drum inertia and radius are considered constant even though in reality mass is added and removed to the outside of the drum during reeling operations while also small changes in radius occur.

Table 4.2: Parameters of the tether model.

Parameters	Value	Unit
r	0.43	m
J	200	$Nm \cdot s^2 \cdot rad^{-1}$
k	9.99	-
c_w	200	$Nm \cdot s \cdot rad^{-1}$
k_F	0.005	$Nm \cdot rad$
k_V	90	$Nm \cdot s \cdot rad^{-1}$

Depending on whether the tether force is within limits, a velocity ($*^v$) or force ($*^F$) controller is used. The controller is given in discrete time, hence the square bracket notation '[k]' and '[k+1]', which indicate a parameter value at the current time step and next time step respectively. The groundstation model is implemented in discrete time with the assumption of very small time steps.

The controller normally operates in velocity control mode and provides a motor torque to the drum $T_m^v[k+1]$ depending on its current torque $T_m^v[k]$ and a gain velocity gain k_v multiplied with the time step dt and the error in radial velocity δ_ω. If the tether force is outside the tether force limits, the force controller torque $T_m^F[k+1]$ will be applied to the drum. This torque depends on its current torque $T_m^F[k]$ and a gain F multiplied by a force delta δ_F (and not with the time stap). The force delta is the difference between the tether force and the reference force. The reference force is either the upper or the lower force limit, depending on whether the tether force is over the maximum force, or under the minimum force. The force limits (F_{min}, F_{max}) as well as the reference reeling velocity (v_{ref}) are generated by groundstation controller provided by Kitepower. Generally speaking $v_{ref} = -1$ [m/s] for reel out and $v_{ref} = 3$ [m/s] for reel in, $F_{min} = 1000$ [N] and $F_{max} = 9000$ [N] are generally fixed for the whole duration of the flight.

$$T_m[k+1] = \begin{cases} T_m^F[k+1] & \text{if } F_T < F_{min}, \text{ or if } F_t > F_{max} \\ T_m^v[k+1] & \text{else} \end{cases} \tag{4.20}$$

$$\delta_\omega = \omega - v_{ref}/r \tag{4.21}$$

$$T_m^v[k+1] = T_m[k] + k_V \delta_\omega dt \tag{4.22}$$

$$F_r = \begin{cases} F_{t,min} & \text{if } F_t < F_{min} \\ F_{t,max} & \text{if } F_t > F_{max} \end{cases} \tag{4.23}$$

$$\delta_F = F_r - F_t \tag{4.24}$$

$$T_m^F[k+1] = T_m[k] + k_F \delta_F \tag{4.25}$$

5

System Identification

In this chapter, the parameters from the two kite models described in chapter 4 will be identified from simulated flight data generated by using the simulation framework. Here, the method will be described that is part of the thesis sub-goal, which is repeated below:

"*To provide Kitepower with a model and method to use experimental flight data for system identification*"

The system identification of both models provides means to compare the identified models and determine which model has a best match, this has never been done before for these kite models. Firstly the equations for the system identification step will be presented, followed by it's results.

The altered kite model equations (Equation 4.12) in combination with the aerodynamic models of Ruppert (Equations 4.3, and 4.6) and Fechner (Equations 4.7, and 4.10) allow for parameter identification through least squares regression (Equation 5.1).

$$\begin{aligned} \boldsymbol{\theta}_F^a &= \left[\mathrm{M}_F^a\right]^{-1} \left(\mathrm{I}\ddot{\mathbf{x}}_G - \mathbf{F}_G^a - \mathbf{F}_G^t - \mathbf{F}_G^g\right) \\ \boldsymbol{\theta}_T^a &= \left[\mathrm{M}_F^a\right]^{-1} \left(\mathrm{J}_k\dot{\boldsymbol{\omega}}_k + \boldsymbol{\omega}_k \times \mathrm{J}_k \cdot \boldsymbol{\omega}_k - \mathbf{T}_G^a - \mathbf{T}_G^t - \mathbf{r} \times \mathbf{F}_G^t\right) \end{aligned} \tag{5.1}$$

For the definition of $\boldsymbol{\theta}_*^a$ and $\mathbf{M}_*^a$ the reader is kindly referred to the Equations M.5 and M.4 for Ruppert's model, and to Equations K.34 and K.57 for Fechner's model.

Method The flight data has been generated by performing flights in the simulation environment with Rupperts model. Figure 5.1 shows the employment of the two different models. Ruppert's model has been implemented in the simulation environment and is used for generating flight data. The parameters for both Ruppert's and Fechners model are identified in by system identification.

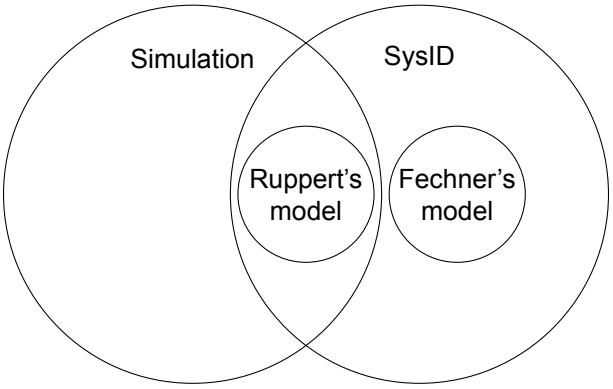

Figure 5.1: Venn diagram of the application of the two kite model types.

Five minutes of flight data is used for the system identification. Considering a logging rate of 1000 Hz, this results in 300.000 data points that can be used for system identification. These points are randomly split in 10 equal groups. One of the groups is kept apart for determining the estimation errors, and 19 of these are used for parameter estimation. The parameters are then identified 19 times such that the mean and variance of each parameter estimate can be determined. This procedure has been performed for both kite models and the results are presented in Figure 5.2 and Figure 5.3. The tabulated parameters in addition to statistical data can be found in Appendix N, this is also where the errors between the estimated and true aerodynamic coefficient curves are shown. Figure 5.4 shows the true and estimated curves for the aerodynamic coefficients.

Results The error curve in Figure N.1 shows a trend and suggests that the errors of the aerodynamic force coefficients can be reduced by adding a fourth order to the parametrization. Adding a fourth order greatly increased the variance of the parameter estimates, therefore the parametrization is limited to the third order. The errors in the estimated aerodynamicforce coefficients curves are small ($< 1\%$). With the assumption that the underlying kite model is identical to Ruppert's model, it can be concluded that the aerodynamic force coefficients for Ruppert's model can be correctly estimated by using data from power generation cycles. The correctness of the estimated parameters cannot be guaranteed for system states that lie outside the flight envelope for normal power cycles. Figure 5.2 shows the identified coefficients for the aerodynamic torque in compared with the actual (known) coefficients. The figure shows that by approximation the estimated errors are correct, however it is expected that the parameters can be perfectly estimated since the system has no noise. The cause of these errors can be introduced by rounding errors in the logged data, but since the rounding error is generally random, this is not a likely cause. Another cause can be an implementation error in the simulation environment which is most likely. A third cause could be an error in the system identification procedure, which seems also unlikely since the aerodynamic force coefficient curves have been estimated through the same procedure with a high accuracy, but it is plausible still. Given the variances of the estimated parameters it seems unlikely that generating additional flight data will improve the estimates.

A similar procedure has been performed for Fechner's modified model. The dataset is split in four sets where for each subset the parameters have been identified. A smaller number of subsets is chosen to reduce the variance of the estimated parameters.

Since the underlying model is that of Ruppert the variances of the parameter estimates are expected to be smaller for Ruppert's model than Fechners model. For the same reason the parameters of Fechner's model cannot be compared with a ground truth as has been done for the aerodynamic coefficients of Ruppert's model.

Figure 5.3 shows that the parameter values and variances of Fechners model. Parameters corresponding to the depower ($C_3^{L,t}$, $C_4^{L,t}$) are low with a low variance. Furthermore it can be observed that the depower does affect the lift and drag of the top more than the sides.

The identified steering coefficients ($C_3^{L,s}$, $C_4^{L,s}$, $C_3^{D,s}$, $C_4^{L,s}$ are all identified to be zero with low parameter

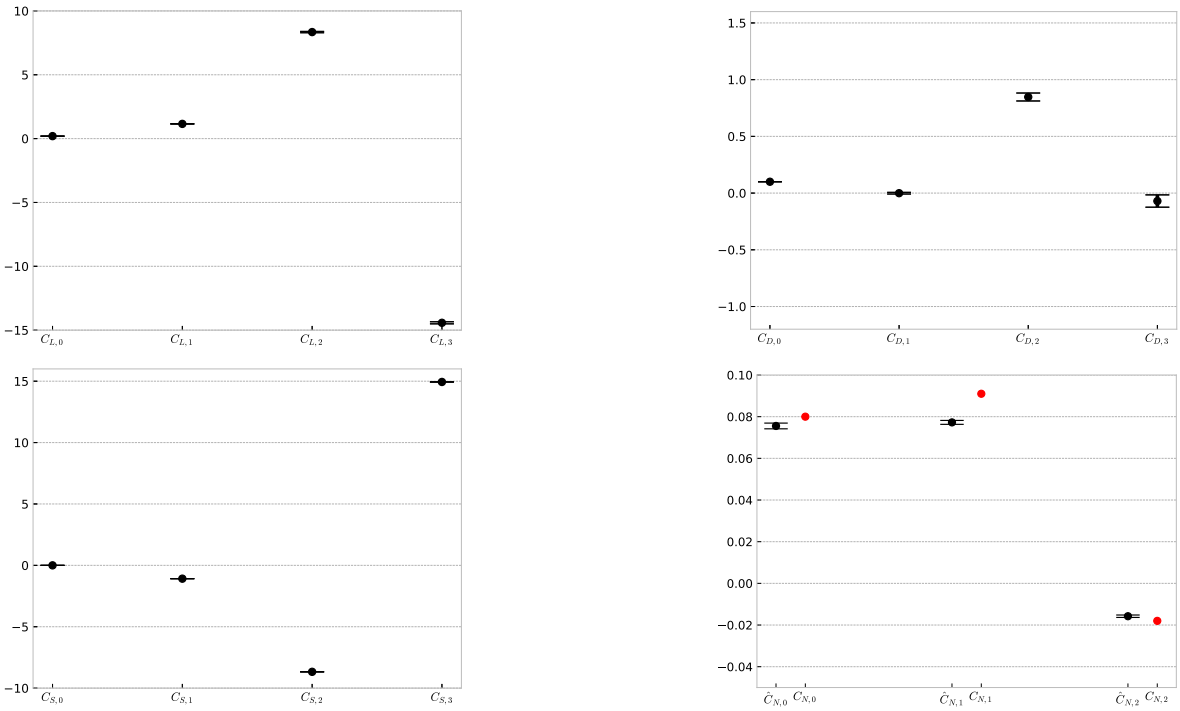

Figure 5.2: Estimated parameters and standard errors for the identified parameters of Ruppert's model. For the meaning of the parameters the reader is referred to subsection 4.1.1.

variance. Since the steering $\delta_s \in [0, 1]$ these values are expected to be visibly nonzero.

A high parameter variance means low certainty, the parameter might be redundant and possibly fits to noise. Additionally a low parameter value with low variance, means the parameter value certainty is high, however it's contribution is low, therefore the parameter can be considered to be dropped. Before dropping a parameter from the model, one needs to take a look at the effective contribution in the resulting aerodynamic coefficient, e.g. by multiplying the depower parameters by the average depower value.

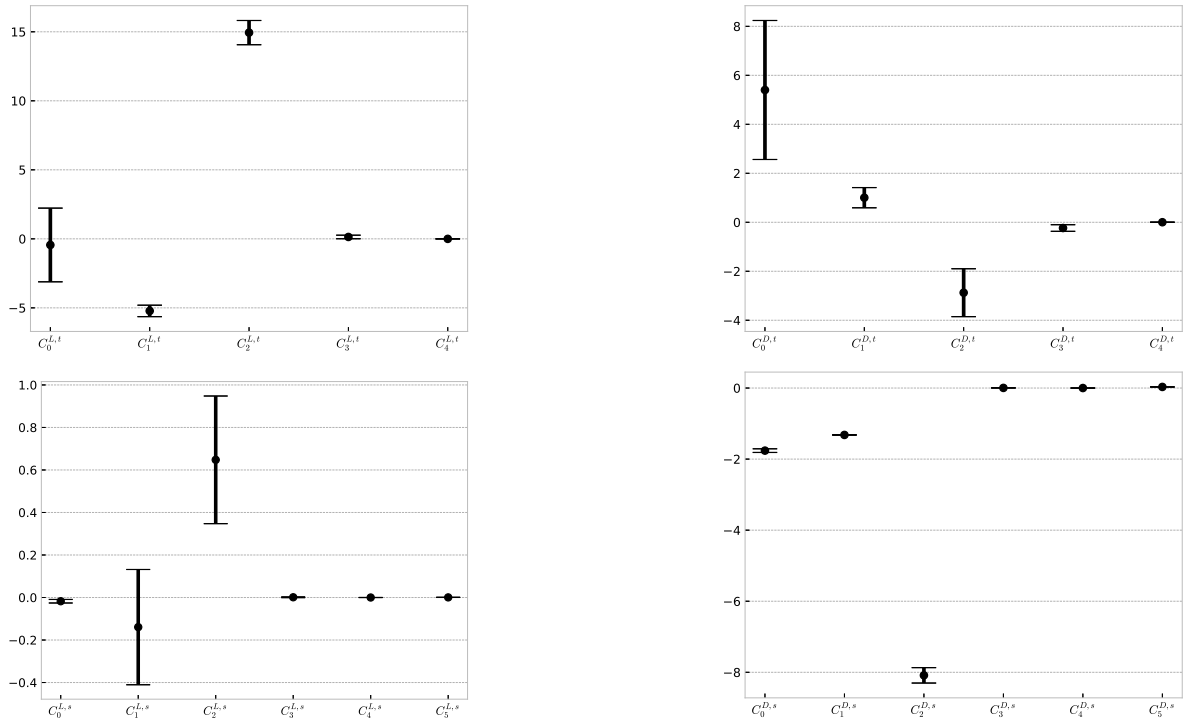

Figure 5.3: Estimated parameters and standard errors for the identified parameters of Fechner's model. For the meaning of the parameters the reader is referred to subsection 4.1.2.

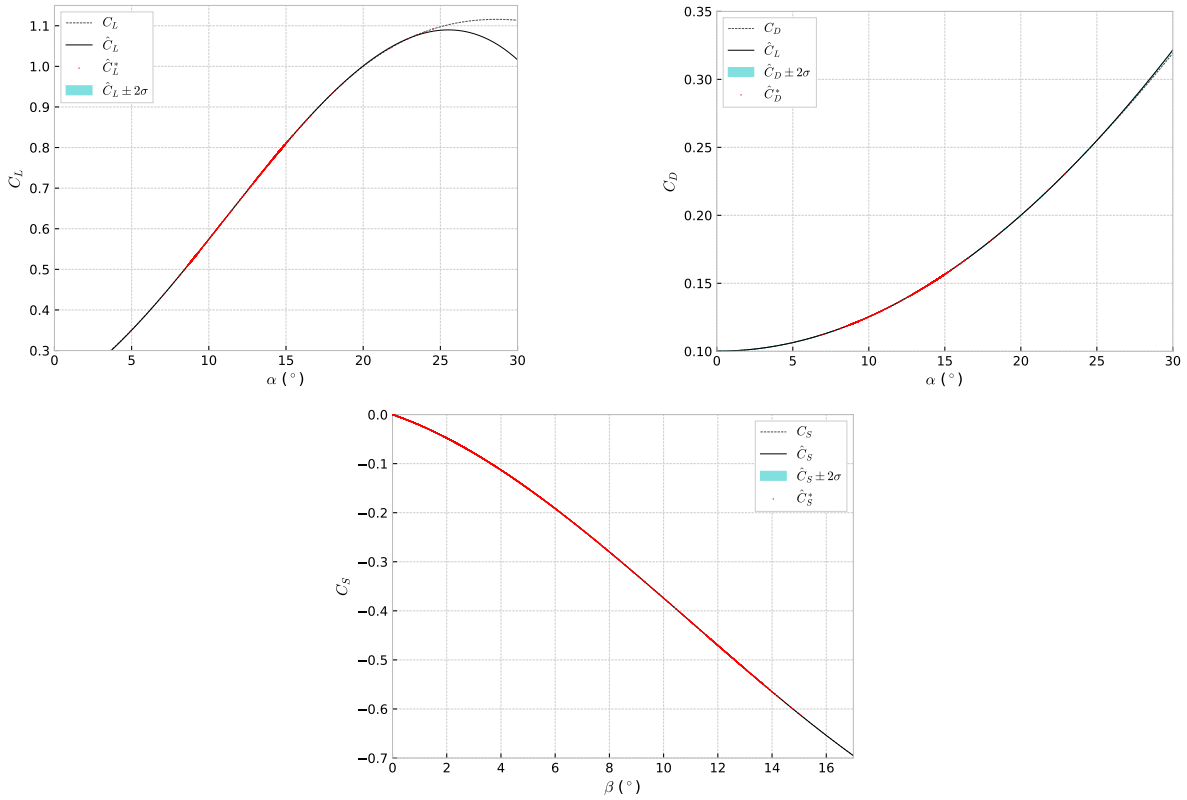

Figure 5.4: Estimated aerodynamic coefficient (solid line), true aerodynamic coefficient (dashed), instantaneous estimate (red dot) and 2σ bound of the aerodynamic coefficients identified for Ruppert's kite model for varying α and β. From top left, top right to bottom: Lift force, drag force, side force coefficient. The 2σ bound is not visible due its narrowness compared to the linewidth and size of the plotted dots.

6

Investigation of the Effect of the Mass and Drag of the KCU

The previous chapters all contain preliminary work that was required in order to be able to perform experiments in a simulation environment. This chapter will first restate the goal of the experiments. Then the four different experiments will be explained that inspect different values for the mass and drag of the KCU for two different wind speeds. In order to facilitate the comparison of flight data between experiments, the average cycle needs to be determined for each experiment. This cycle averaging method will be explained followed by a comparison between the averaged cycles of the experiments.

For the readers' convenience, the research question will be repeated:

"*What are the effects of mass and drag of the kite control unit on the flight behavior of a flexible airborne wind energy system kite during flight?*"

Additionally, in the motivation of this research (subsection 2.4.2) the following hypotheses have been proposed:

- Kite roll caused by the outward motion of the KCU due to centrifugal forces positively contributes to the steering.
- Additionally, it has been observed in experimental flights that added drag induced by an on-board turbine reduces the angle of attack of the kite.
- The aerodynamic drag of the KCU might play a role in the hypothesized outward motion as well.

6.1. Experiment Description and Cycle Flight Data Averaging

Two experiments have been performed at two different wind speeds. Each experiments consists of a number of simulated flights. Each flight lasts at least 20 minutes (1200 seconds). An overview of the experiment and the experiment parameters is provided in Table P.1. The system behavior of a traction-based AWE system is cyclical, therefore one flight consists of several cycles. The flight data from the experiments is averaged over the cycles and the average cycles are then compared.

During each simulated flight, several cycles have been flown. For most flights, the flight paths show no more convergence after three cycles, therefore the first three cycles of each flight are discarded and the remainder are used for analysis. The flight data is split in cycles such that the average cycle can be determined. The flight data is then subsampled to a period of 100 ms through period averaging. This method provides information about the standard deviations of any measured paramter at each point

in time. Figure 6.1 shows the results of this procedure. The topright figure also shows a distinction between the traction and retraction phase, where the traction phase is often called the power production phase. It can be observed that the mean flight path (and power) show a gap between start and end, this is an effect of the above described procedure since one can only average over the duration of the shortest recorded cycle such that cycles with a larger duration are truncated.

When comparing signals it is important to take the variance into consideration. The selection of the point of alignment (in the cycle averaging procedure) has an influence on the variance of the signals. The variance during the traction phase will be larger when the cycles are aligned at the start of the retraction phase. This causes the traction phase to follow after the retraction phase and any delays that occurred during the retraction phase will leak into the traction phase as well, therefore increasing the variance.

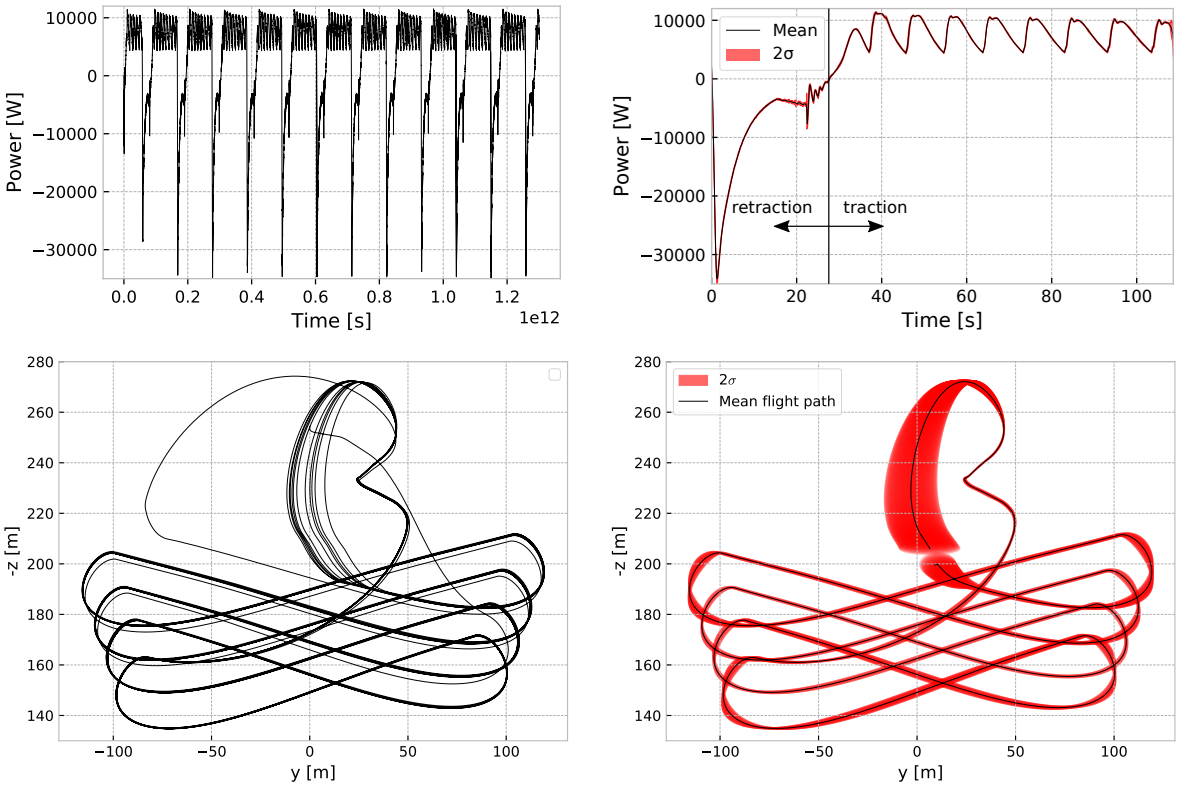

Figure 6.1: Top left: Mechanical power over time for one complete flight. Top right: Average mechanical power per cycle for the same flight with 2σ in red. Bottom left: recorded flight path. Bottom right: average cycle flight path with 2σ bounds in red.

6.2. Results for Increasing KCU Drag Experiments

The experiments discussed in this section show the effects of increasing the KCU drag for a wind speed of $v_w = 6$ [m/s] and $v_w = 10$ [m/s] respectively. Conclusions will be drawn per wind velocity. The mass of the KCU is $m_{KCU} = 8$ [kg] for both experiments.

Firstly, it can be observed that the average cycle power remains the same when increasing the drag of the KCU from 0 to 1.5 (Figure 6.2, Figure 6.3). A closer look shows that in both phases (traction) and retraction the power also shows no significant variations even though the drag ratio does increase to a maximum 5% (Figure 6.5). The retraction phase shows quite a large variance, the cause of this lies in the flight paths which for a low wind condition show less convergence (and thus larger variance) than the high wind condition, as can be seen in Figure 6.6 which shows the YZ coordinates of kite for the two different wind conditions. It is expected that the angle of attack during retraction shows a decrease with increasing KCU drag. Figure 6.4 shows the angle of attack during retraction (0-20s), except for

the shift in time, the magnitude of angle of attack is not significantly different for different values for the drag of the KCU.

An important remark needs to be made regarding Figure 6.2. Since the duration of the traction phase and retraction phase are different, the average cycle power is not simply the mean of the two. For this reason, changes in traction power have more influence in the average cycle power than changes in the retraction power.

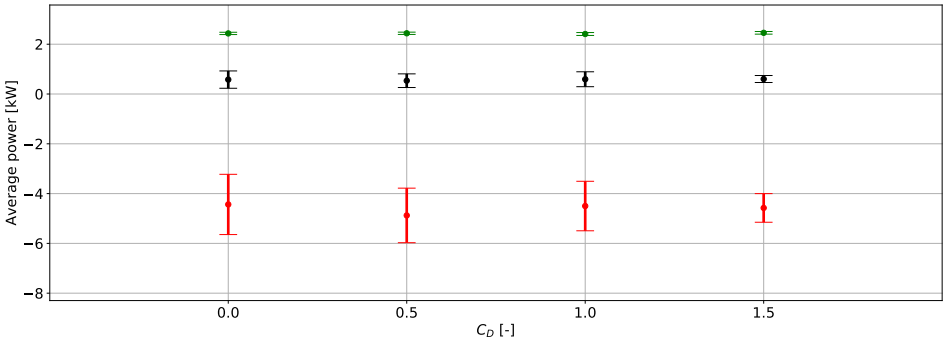

Figure 6.2: Average cycle power for increasing $C_{D,KCU}$ at $v_w = 6$ [m/s]. Green (top): average traction power; Black (center): average cycle power; Red (bottom): average traction power.

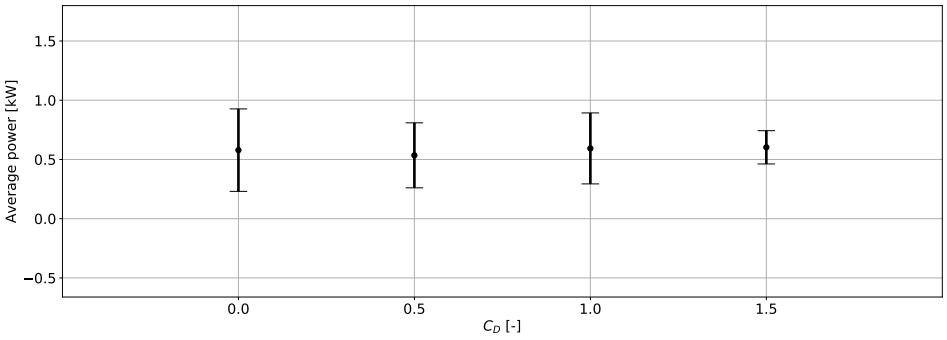

Figure 6.3: Average cycle power for increasing $C_{D,KCU}$ at $v_w = 6$ [m/s].

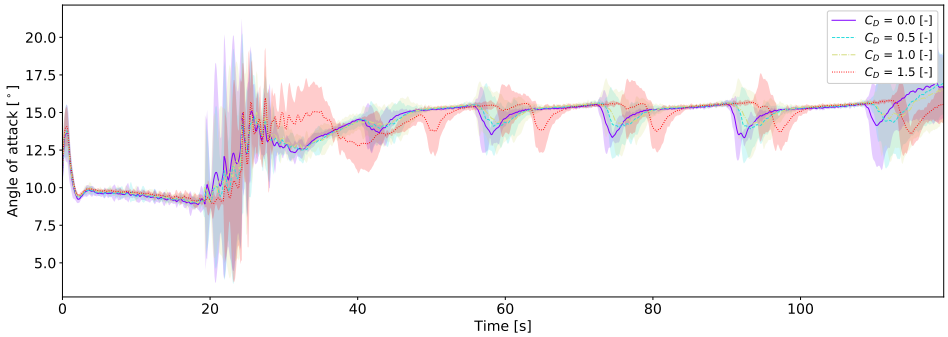

Figure 6.4: Average angle of attack $C_{D,KCU}$ at $v_w = 6$ [m/s]. The shaded region indicates the 2σ bounds.

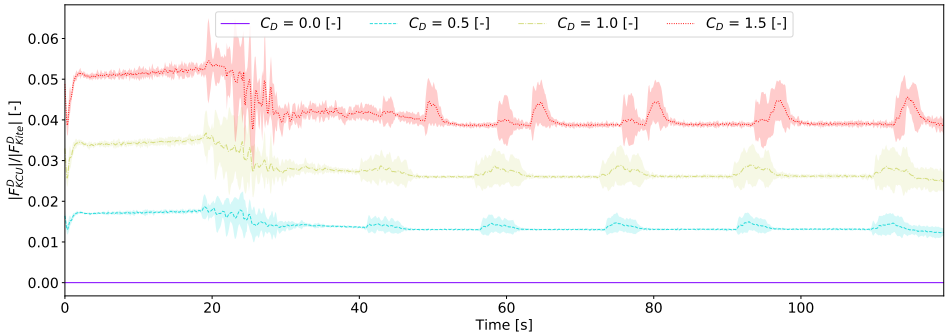

Figure 6.5: Average drag ratio of the drag forces of the KCU and Kite for increasing $C_{D,KCU}$ at $v_w = 6$ [m/s]. The shaded region indicates the 2σ bounds.

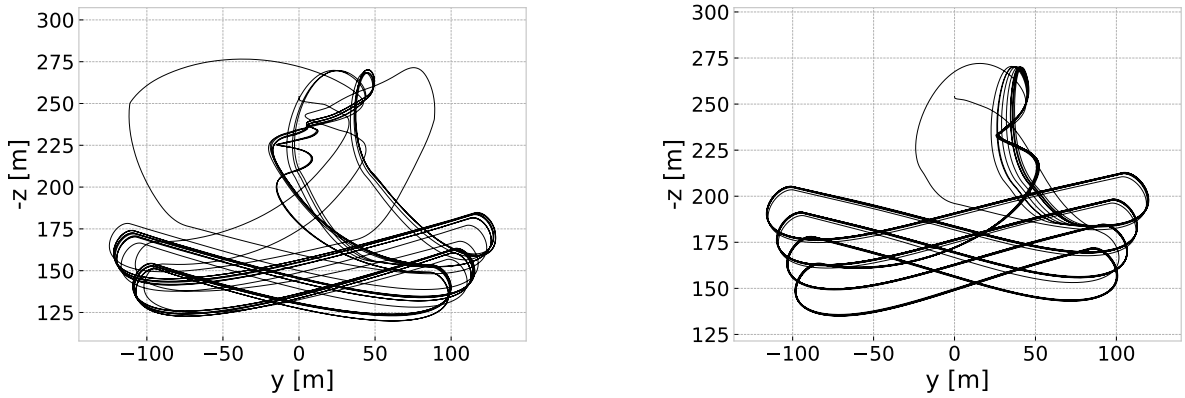

Figure 6.6: YZ position of the kite for identical KCU mass and drag for $v_w = 6$ [m/s] (left) and $v_w = 10$ [m/s] (right).

The same experiment at a wind speed $v_w = 10$ [m/s] shows us that a decrease in the average total cycle power ($\approx 7\%$, 250 [W]) can be observed (Figure 6.7), for $C_{D,KCU} = 0$ to $C_{D,KCU} = 1.5$. Figure 6.8 shows that this is caused by a reduction of generated power during the traction phase, since the power in the retraction phase does not change (much). Figure 6.9 confirms this since it clearly shows a lower instantaneous power during the traction phase (>30s), where during the retraction phase no big differences can be observed.

Looking further into the cause of this decrease in generated power, Figure 6.11 shows a decrease in the apparent wind velocity with an increase in tether force as result (Figure 6.12). Since the reeling velocity in Figure 6.29 does not show such changes in magnitude and the flight paths during traction are very similar (Figure 6.10), it can be concluded that the reduction in power is definitely caused by

the increased KCU drag which leads to lower kite velocities during the traction phase and thus a lower power output.

Additionally it is interesting to see (Figure 6.14), that the drag ratio of the KCU drag over the kite drag is around 3% for a C_D of 1.0 which shows that with the small surface of the KCU, quite a large drag force contribution is caused due to the large value of the drag coefficient C_D.

Finally, Figure 6.15 shows a change in angle of attack of <0.5° for traction and retraction, with an increase for both traction and retraction. It was thought that the angle would decrease during retraction, but the reverse is shown. Considering that the apparent wind speed during retraction is lower, this is thought to be the cause of the increase in angle of attack. The reasoning behind this is as follows: a reduced velocity of the kite leads to an increase in angle of attack (in retraction) due to a lower contribution of the kite speed to the apparent wind speed.

So, concluding for this experiment the reduction in average cycle power ($\approx 7\%$) can be attributed to a reduction in power production due to a reduction velocity as a direct result from the increase in KCU drag from 0 to 1.5 Additionally, no decrease in angle of attack has been observed during retraction, the opposite effect has been observed however quite small (<0.5°).

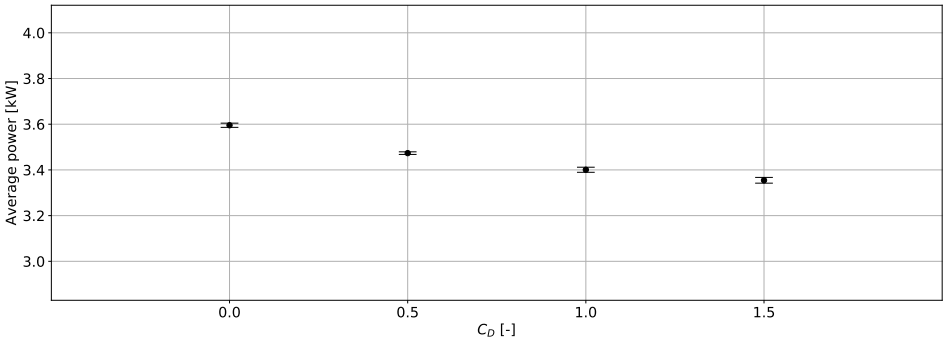

Figure 6.7: Average total cycle power for increasing $C_{D,KCU}$ at $v_w = 10$ [m/s].

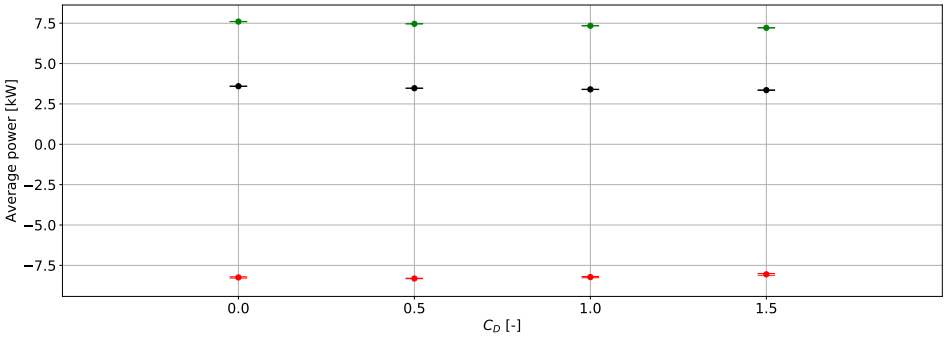

Figure 6.8: Average cycle power for increasing $C_{D,KCU}$ at $v_w = 10$ [m/s]. Green (top): average traction power; Black (center): average cycle power; Red (bottom): average traction power.

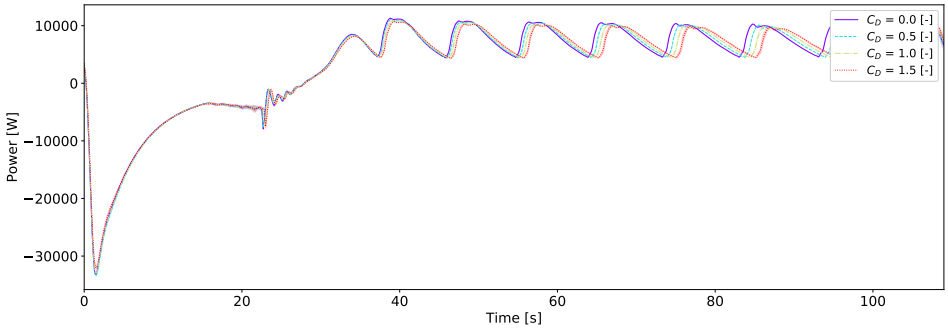

Figure 6.9: Average instantaneous power for increasing $C_{D,KCU}$ at $v_w = 10$ [m/s]. The shaded region indicates the 2σ bounds.

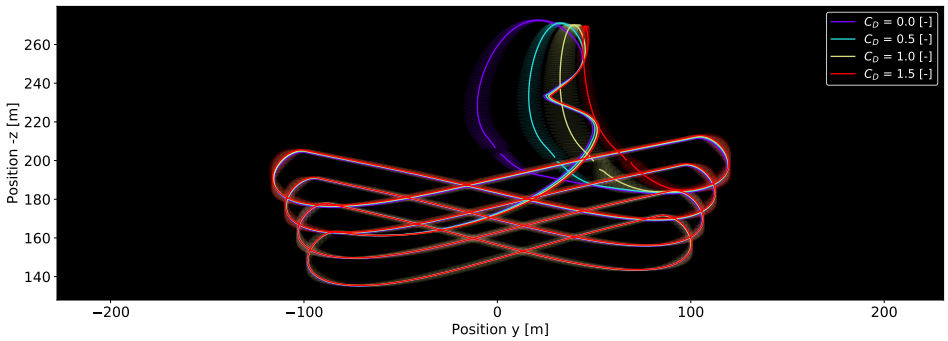

Figure 6.10: Average y-z flight paths for increasing $C_{D,KCU}$ at $v_w = 10$ [m/s]. The shaded region indicates the 2σ bound. The shaded region indicates the 2σ bounds.

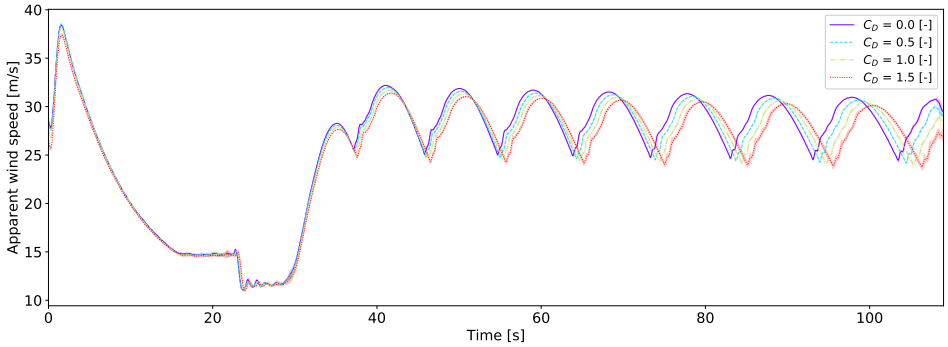

Figure 6.11: Average apparent wind speed for increasing $C_{D,KCU}$ at $v_w = 10$ [m/s]. The shaded region indicates the 2σ bounds.

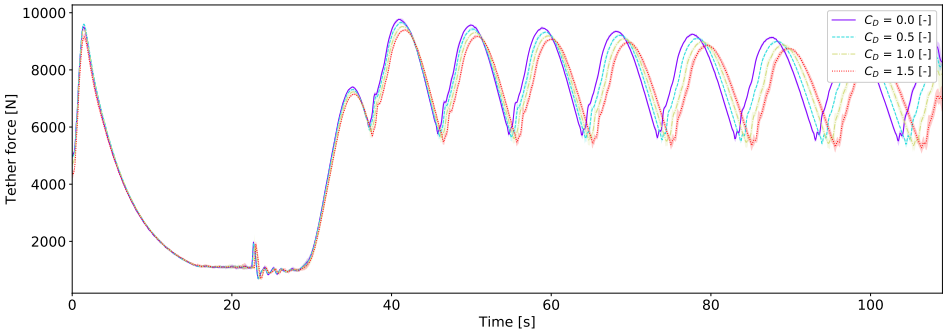

Figure 6.12: Average tether force (near groundstation) for increasing $C_{D,KCU}$ at $v_w = 10$ [m/s]. The shaded region indicates the 2σ bounds.

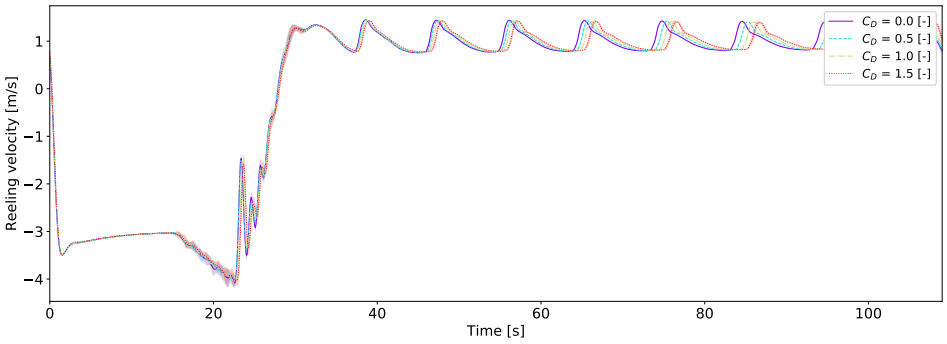

Figure 6.13: Average reeling velocity force for increasing $C_{D,KCU}$ at $v_w = 10$ [m/s]. The shaded region indicates the 2σ bounds.

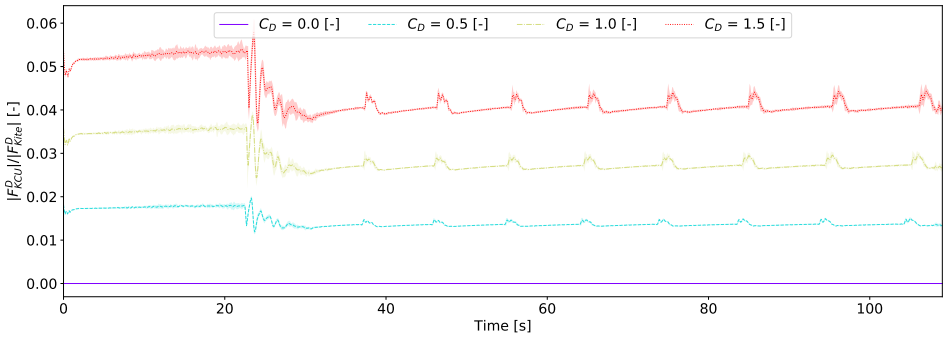

Figure 6.14: Average drag ratio of the drag forces of the KCU and Kite for increasing $C_{D,KCU}$ at $v_w = 10$ [m/s]. The shaded region indicates the 2σ bounds.

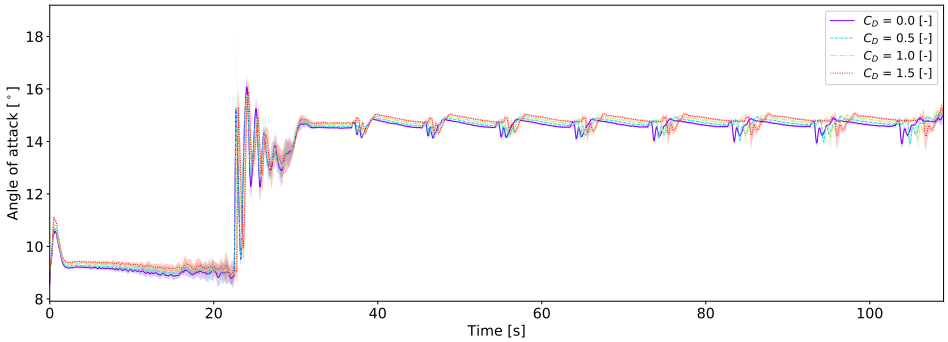

Figure 6.15: Average angle of attack for increasing $C_{D,KCU}$ at $v_w = 10$ [m/s]. The shaded region indicates the 2σ bounds.

6.3. Results for Increasing KCU Mass

6.3.1. Results for Increasing KCU Mass at $v_w = 6$ [m/s]

The experiment showed that the average cycle power is increasing with increasing mass, this is counter intuitive since one expects the power to decrease with increasing KCU (and kite) mass due to a reduction in effective lift available for power production.

This experiment consists of two parts, one for increasing KCU mass and one for increasing kite mass (as a reference):

- $m_{KCU} \in [0, 2, 4, 6, 8, 10, 12, 14, 16, 18, 20, 22, 26]$ [kg], $m_{kite} = 10.5$ [kg].
- $m_{kite} \in [2.5, 4.5, 6.5, 8.5, 10.5, 12.5, 14.5, 16.5, 18.5]$ [kg], $m_{KCU} = 8$ [kg].

Figure 6.16 shows that for an increasing KCU mass, the average total cycle power output is increasing (with a 150% maximum). Not only does the required power during retraction decrease, the power generated during power production is improved.

Following these observations, the question can be asked whether this increase in power can be attributed to the placement of the mass at the KCU, or that an increase of the kite mass will show a similar effect. Figure 6.17 provides an answer to this question and shows that with an increasing kite mass, the average cycle power is increased as well.

In the same figure (Figure 6.17) can be seen that when the kite mass is varied instead of the KCU mass, the power starts at roughly zero [kW]. One reason for this low cycle power could be the unrealistic ratio between the kite mass and KCU mass where the kite is 2.5 [kg] and the KCU is 8 [kg].

Figure 6.18 shows a comparison between the two experiments. The results for an increasing KCU mass is shown in black and the results for an increasing kite mass in red (which is slightly offset to the right in order to prevent overlap). The figure shows two things: 1) For an increasing mass the average cycle power increases, and 2) For the same total weight of kite and KCU, if the kite mass is lower than that of the KCU, the cycle power is lower.

The figure also shows a green and red region. For the experiment where the kite's mass is increased, strange retraction behavior started to occur for a kite mass of 18.5 [kg] and a total mass of 26.5 [kg]. The kite could not remain airborne for a total mass of 28.5 [kg] or higher. Therefore this region ($m_{total} \geq 26.5$ [kg]) is considered incomparable. In the case where the kite mass is constant and the KCU mass was increased, the kite crashed at a total weight of 40.5 [kg]. This difference in total mass that leads to a crash can be explained by the observed behavior that the KCU mass causes the lift vector to be pointed more upward when the kite is on the side of the wind window, therefore increasing the ability to remain airborne.

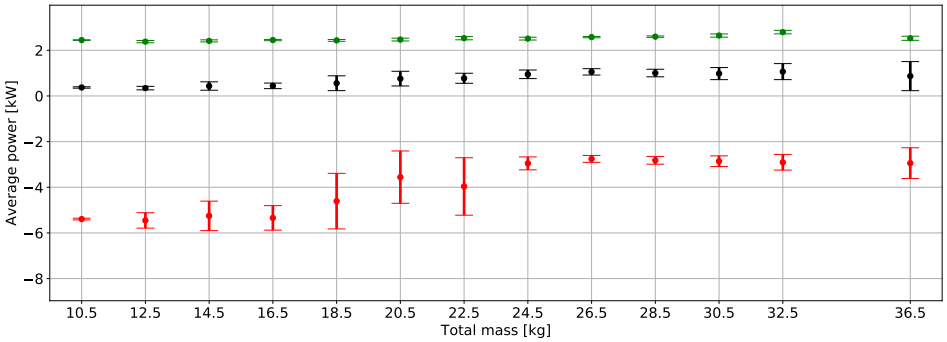

Figure 6.16: Average cycle power for increasing m_{KCU} at $v_w = 6$ [m/s]. The horizontal axis shows the total mass ($m_{KCU} + m_{kite}$). Green (top): average traction power; Black (center): average cycle power; Red (bottom): average traction power.

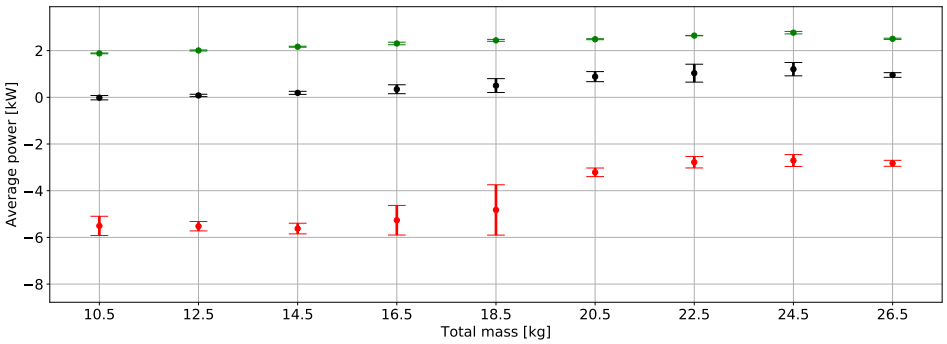

Figure 6.17: Average cycle power for increasing m_{kite} at $v_w = 6$ [m/s]. The horizontal axis shows the total mass ($m_{KCU} + m_{kite}$). Green (top): average traction power; Black (center): average cycle power; Red (bottom): average traction power.

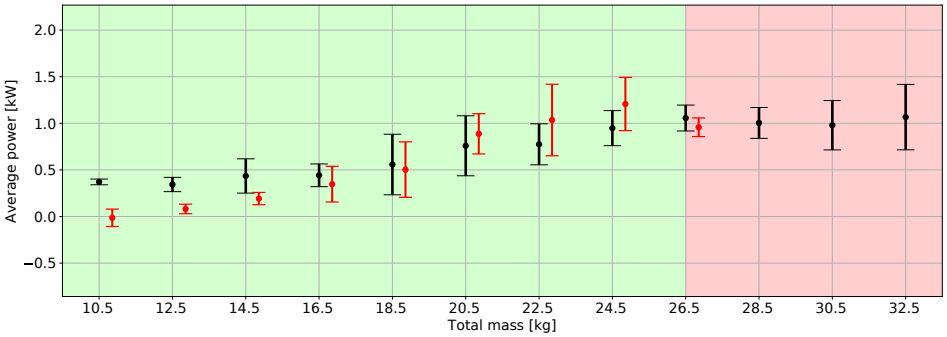

Figure 6.18: Average cycle power for increasing m_{KCU} (black) and m_{kite} (red) at $v_w = 6$ [m/s]. The horizontal axis shows the total mass ($m_{KCU} + m_{kite}$).

For a selection of kite masses $m_{kite} \in [2.5, 4.5, 6.5, 8.5, 10.5, 12.5]$ [kg] (with fixed KCU mass $m_{KCU} = 8$ [kg]), a further look is taken into the cause of the power increase. Figure 6.19 shows that for an increasing kite mass, the tether force increases during traction (>35 s) and is reduced during the first part of the retraction phase (< 20 s). During these phases the reeling velocity shows only small changes during the beginning of the retraction phase and almost no change in magnitude during the traction phase. Therefore the increase in tether force during traction is the main cause of the power increase which is a direct result of the increase in the apparent wind speed (Figure 6.21). The increased apparent wind speed can only be increased by an increase in the kite speed since the wind speed is constant. The increased kite velocity during traction is thought to be caused by one (or both) of the following

two things: 1) During the downward turns the velocity of the kite is higher due to the increased mass with a resulting increase in gravitational force leading to a higher downward velocity; 2) A lower overall altitude of the kite (and thus elevation angle) (Figure 6.22) resulting in a higher apparent wind speed projected on the kite's local xz-plane. The increase in kite speed will be further inspected after the next set of experiments, since for the higher wind speed the kite trajectories show more convergence therefore easing the analysis.

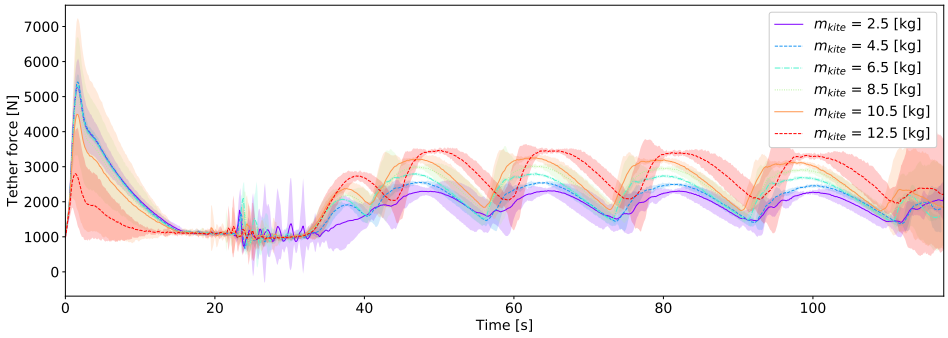

Figure 6.19: Average tether force for increasing m_{kite} and fixed KCU mass $m_{KCU} = 8$ and wind speed $v_w = 6$ [m/s]. The shaded region indicates the 2σ bounds.

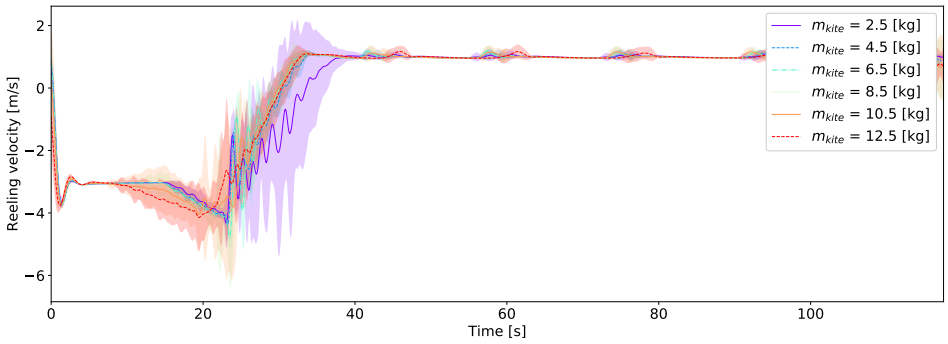

Figure 6.20: Average reeling velocity for increasing m_{kite} and fixed KCU mass $m_{KCU} = 8$ and wind speed $v_w = 6$ [m/s]. The shaded region indicates the 2σ bounds.

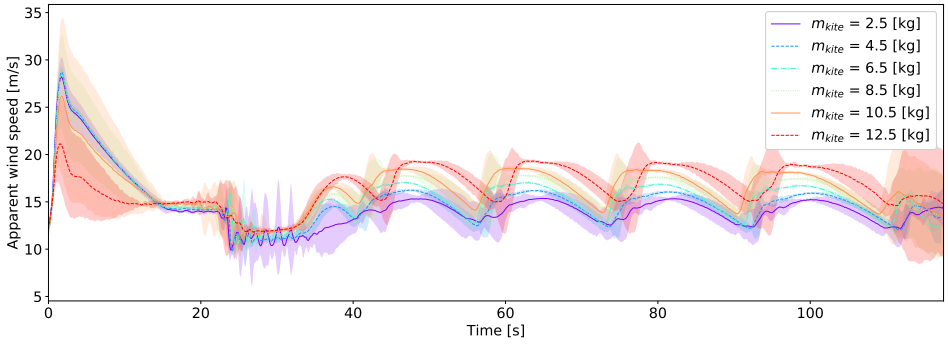

Figure 6.21: Average apparent wind speed for increasing m_{kite} and fixed KCU mass $m_{KCU} = 8$ and wind speed $v_w = 6$ [m/s]. The shaded region indicates the 2σ bounds.

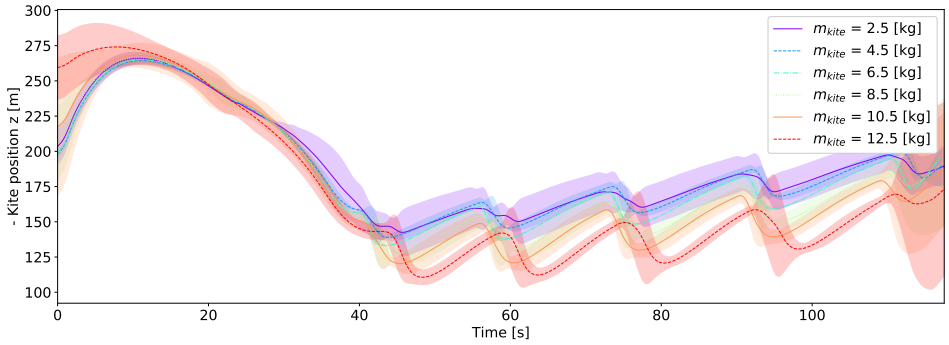

Figure 6.22: Average z-position of the kite ($-z$ =altitude) for increasing m_{kite} and fixed KCU mass $m_{KCU} = 8$ and wind speed $v_w = 6$ [m/s]. The shaded region indicates the 2σ bounds.

The hypothesis that the KCU swings outward with increasing mass and therefore possibly contributing to an aerodynamic lift force pointing inward to the turn will now be discussed. The outward KCU swing behavior is shown in Figure 6.24. A simplified projection of the kite and tether on the yz plane shows the difference between non-outward swing and outward swing. In the case of outward swing, the y-position of the KCU is expected get closer to the kite or 'overtake' the kite in the y-position during turns.

Figure 6.23 shows the difference in the y-position between the kite and KCU. For an outward swing to be observed, the difference in y-position between the KCU and the kite is expected to be reduced to zero or even change sign at the outer sides of the turn, which does not occur. In the figure, the turns occur during the minima and maxima in y-position, so at approximately 42, 58, 70 and 90 seconds. Outward swing is expected to be larger when the tether tension is lower as a result of a lower wind speed resulting in more tether slack. However, due to the path variance, it is hard to draw any conclusions regarding the outward swing behavior of the KCU for the windspeed of $v_w = 6$ [m/s].

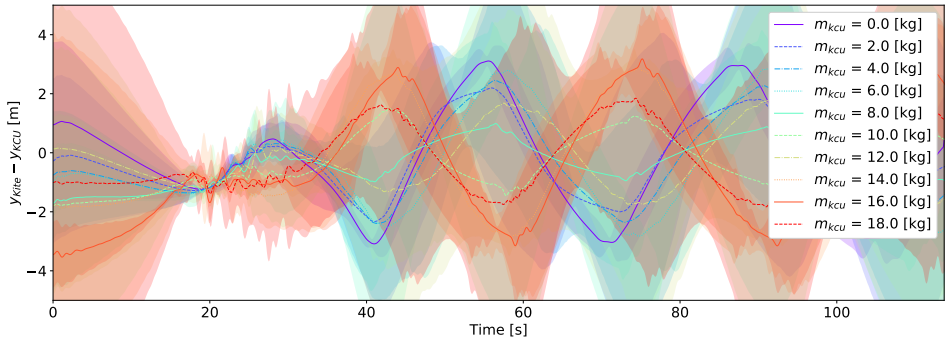

Figure 6.23: Difference between KCU and kite y-coordinate for increasing $m_{D,KCU}$ at $v_w = 6$ [m/s]. The shaded region indicates the 2σ bounds.

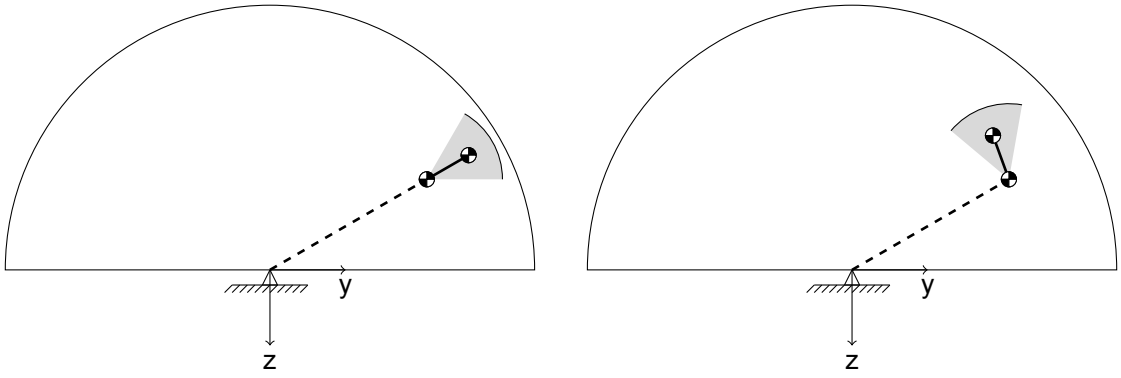

Figure 6.24: An exaggerated visualization of the expected outward swing behavior of the KCU. A projection of the kite and tether on the yz-plane is shown. The encompassing circle shows the reachable space projected on the yz plane. The KCU is represented by the lower blocked circle, whereas the kite's center of mass is represented by the upper blocked circle.

6.3.2. Results for Increasing KCU Mass at $v_w = 10$ [m/s]

This experiment has been split into two experiments as has been done in the previous section. This time the mass of the kite and KCU are as follows:

- $m_{KCU} \in [0, 2, 4, 6, 8, 10, 12, 14, 16, 18, 20, 22, 26, 30, 34, 38, 42]$ [kg], $m_{kite} = 10.5$ [kg];
- $m_{kite} \in [2.5, 4.5, 6.5, 8.5, 10.5, 12.5, 14.5, 16.5, 18.5, 20.5, 24.5, 28.5, 32.5]$ [kg], $m_{KCU} = 8$ [kg]

Figure 6.25 shows that, for a wind speed of 10 [m/s], an increase in mass leads to an increase in the produced power (by 40 - 100 %). It also shows that the system power output will be higher when the kite mass is larger then the mass of the KCU. The green region in the figure indicates the region where the results will be compared since for this region the kite did not crash or show any strange deviations in the flight path. The kite was unable to stay airborne for a total weight of 42.5 [kg] with a kite mass of $m_{kite} = 34.5$ [kg]. When the mass of the KCU is varied and the total mass is increased beyond 52.5 [kg] the simulation is required to stop due to a very large peak force in the retraction phase which the numerical solver is unable to deal with, resulting in a crash of the kite.

The flight paths show low variance (Figure 6.26) which enables further investigation into the cause of the increased power output. The data for an increasing kite mass will be used for this analysis since this shows the most promising gains in power and it is expected that the underlying cause of the increase in cycle power is identical.

Figure 6.27 shows that the average power of the retraction phase varies very little and therefore the increase in cycle power can be attributed to an increase of power during the traction phase. Figure 6.28 shows that during the traction phase (>25 [s]), the tether force is increasing with increasing kite mass. What can also be observed is that the tether force is limited to the tether force limit set by the ground station controller. It is at the times the tether force limit is reached that the reeling velocity is increased, which can be observed in Figure 6.29. For the cases where the tether force does not reach the force limit, no big differences can be observed in the reeling velocity. So the increase in power is caused by the increase in tether force in combination with an increase in reeling speed where the tether force hits the force limits.

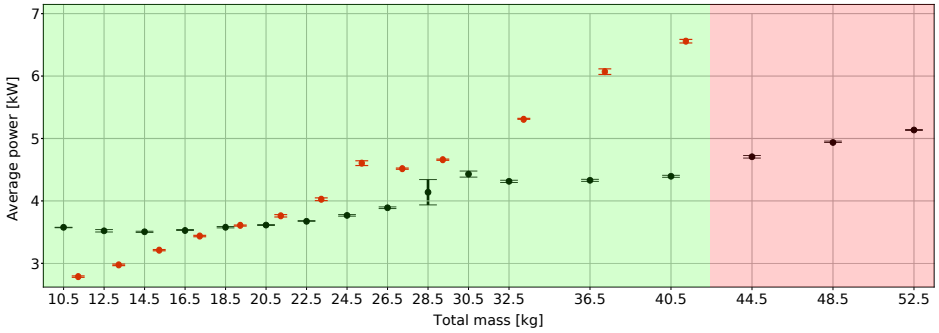

Figure 6.25: Average cycle power for increasing m_{KCU} (black) and m_{kite} (red) at $v_w = 10$ [m/s]. The horizontal axis shows the total mass ($m_{KCU} + m_{kite}$).

As discussed in the previous section, the increase in tether force is a result of an increase in the apparent wind velocity which is a result from an increase in kite velocity. Inspection of Figure 6.31 shows that the velocity in the z-direction of the kite (in the global frame) shows changes in the velocity of both the upward movement of the kite as well as the downward movement of the kite (negative z is the upward). In the downward movement, the acceleration seems quite constant and it does not look like velocity saturation occurs before the velocity sharply declines again. The speed at which saturation is expected is when the vertical lift and drag components of the kite are in equilibrium with the gravitational force acting on the kite's mass. For an increasing kite mass this will result in a higher saturation speed. Since saturation of the downward vertical speed cannot be observed in Figure 6.31, the cause of the increase in kite velocity must be the result of a lower altitude leading to differently oriented aerodynamic forces and therefore a higher velocity and tether force. The increase in the kite's velocity in the y-direction (perpendicular to the wind) also shows an increase in absolute kite speed, which confirms this conclusion since the velocity in the y-direction is much less dependent on the kite's mass since the gravitational component does not directly influence the acceleration (and therefore the velocity) in the y-direction. Figure 6.32 very clearly shows the effect of an increasing mass on the altitude of the kite during traction. A reduction in altitude corresponds to a reduction in elevation angle.

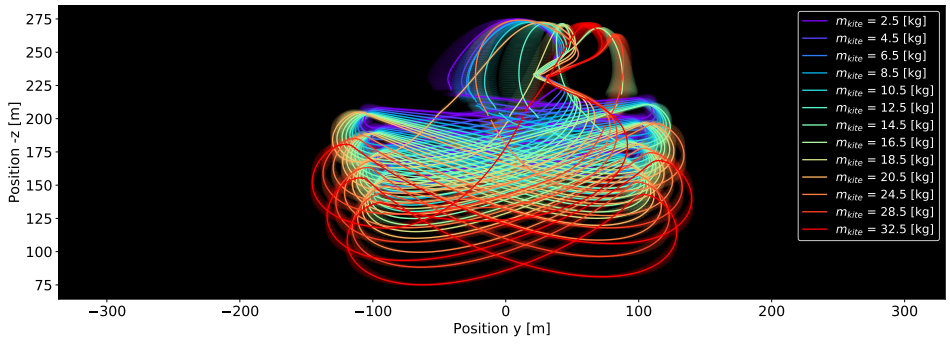

d

Figure 6.26: Average cycle path for increasing m_{kite} at $v_w = 10$ [m/s]. The shaded region indicates the 2σ bounds.

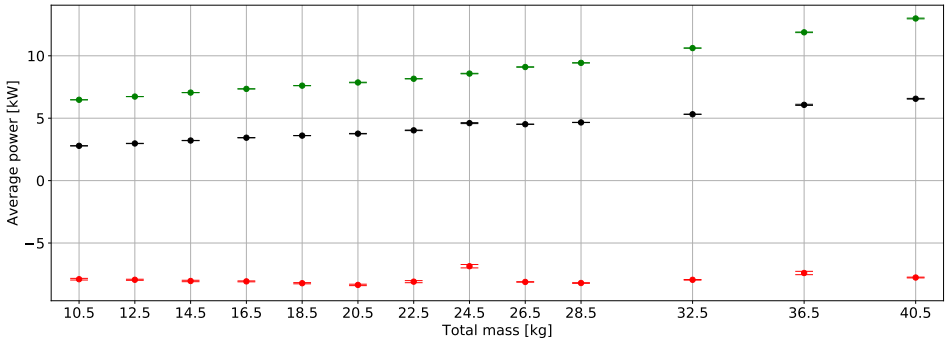

Figure 6.27: Average cycle power for increasing m_{kite} at $v_w = 10$ [m/s]. The horizontal axis shows the total mass ($m_{KCU} + m_{kite}$). Green (top): average traction power; Black (center): average cycle power; Red (bottom): average traction power.

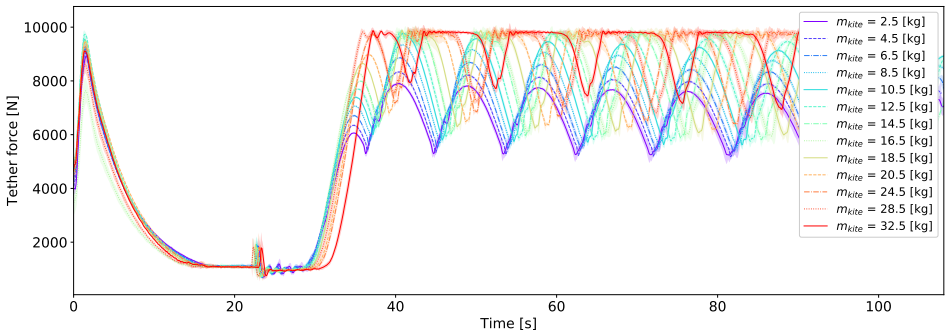

Figure 6.28: Average tether force for increasing m_{kite} at $v_w = 10$ [m/s]. The shaded region indicates the 2σ bounds.

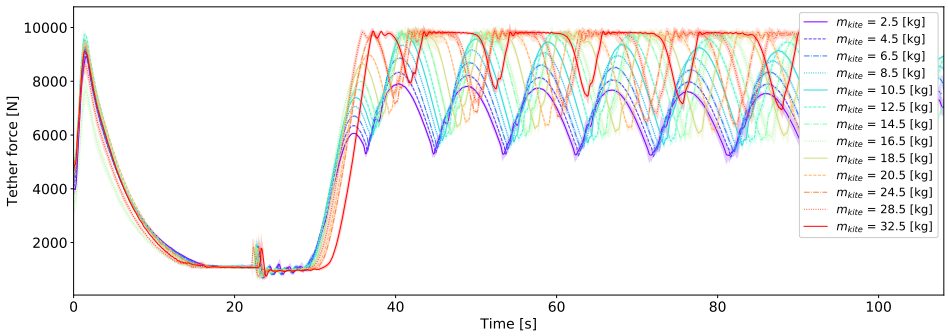

Figure 6.29: Average reeling velocity for increasing m_{kite} at $v_w = 10$ [m/s]. The shaded region indicates the 2σ bounds.

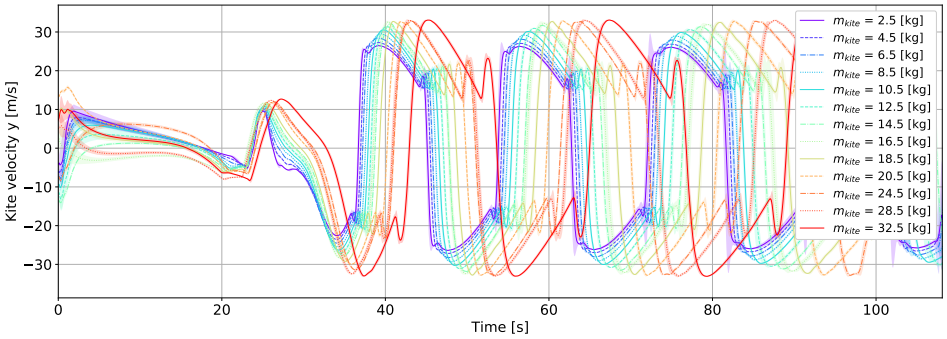

Figure 6.30: Average kite velocity in y direction for increasing m_{kite} at $v_w = 10$ [m/s]. The shaded region indicates the 2σ bounds.

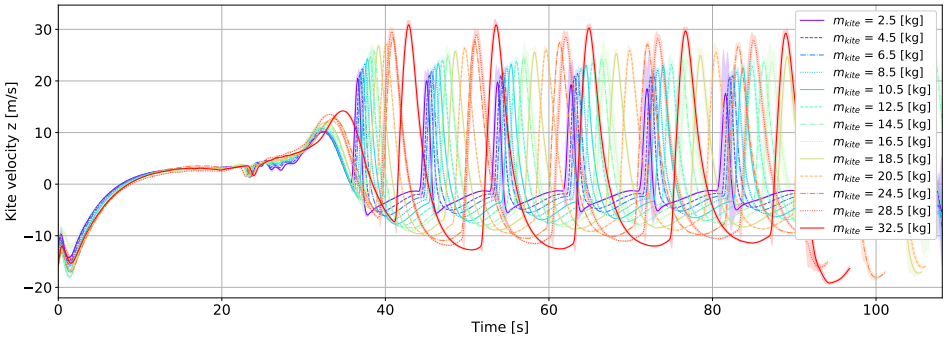

Figure 6.31: Average kite velocity in z direction for increasing m_{kite} at $v_w = 10$ [m/s]. The shaded region indicates the 2σ bounds.

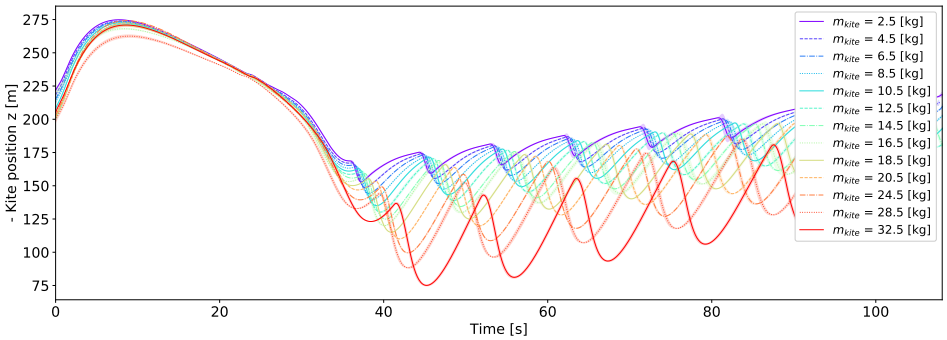

Figure 6.32: Average kite position in z direction for increasing m_{kite} at $v_w = 10$ [m/s]. The shaded region indicates the 2σ bounds.

As a side note, generally the addition of the KCU mass leads to oscillations in the system states, e.g. roll and pitch rate, angle of attack, sideslip and reeling velocity.

This concludes this inspection of the cause of the power increase in the power production phase. Now, continuing with the research question, a look will be taken at the outward swing of the KCU. Figure 6.33 and Figure 6.34 show the difference in y-position between the kite and KCU as described before. In Figure 6.33, it can be seen that for increasing KCU masses, fluctuations at the turns start appearing. The turns can be identified by the minima and maxima of the saw-tooth-like plot. For a regular KCU mass of $m_{KCU} = 8$ [kg] in combination with a kite mass of $m_{kite} = 10.5$ [kg], this fluctuation has a magnitude smaller than 10 [cm] (Figure 6.34). Given the bridle length $l_{bridle} = 8$ [m] and a small angle approximation, this corresponds to a fluctuation around the local x axis (roll) of $\approx 4.5°$.

Finally, when comparing the angle of attack for both scenarios (Figure 6.36 and Figure 6.35), the following observations can be made:

- Retraction: For an increasing KCU mass, the angle of attack increases. For an increasing kite mass, the angle of attack decreases.
- Traction: For an increasing KCU mass, the angle of attack has the same maxima, but lower minima. For an increasing kite mass, the angle of attack has lower maxima and minima.
- Traction: For an increasing KCU mass, oscillations start to appear in the angle of attack, this is most likely the cause of the KCU temporarily overtaking the kite during the downward motion.

No conclusions can be drawn with respect to the effect of the KCU weight on the angle of attack. The angle of attack depends on the speed of the kite, which has been shown to vary between the different experiments. Additionally, the kite path is not constant which also affects the angle of attack. Possibly the angle of attack is not the right measure to investigate and the orientation of the kite with respect to a fixed wind frame or with respect to a plane defined tangential to the dome of the wind window are better measures.

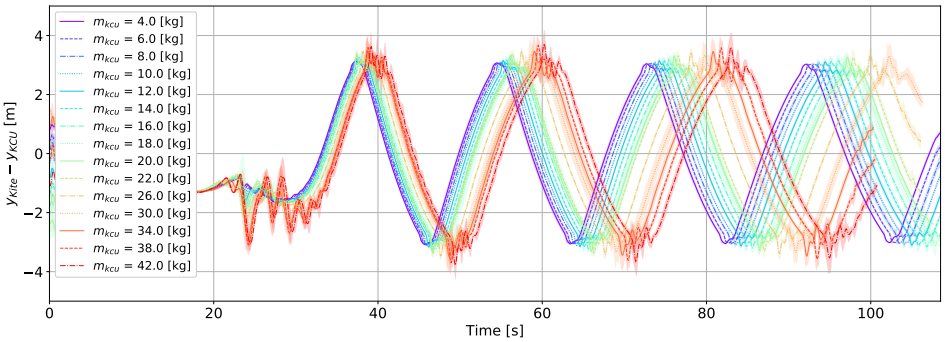

Figure 6.33: Average difference in y position between the kite and KCU for increasing m_{KCU} at $v_w = 10$ [m/s]. The shaded region indicates the 2σ bounds.

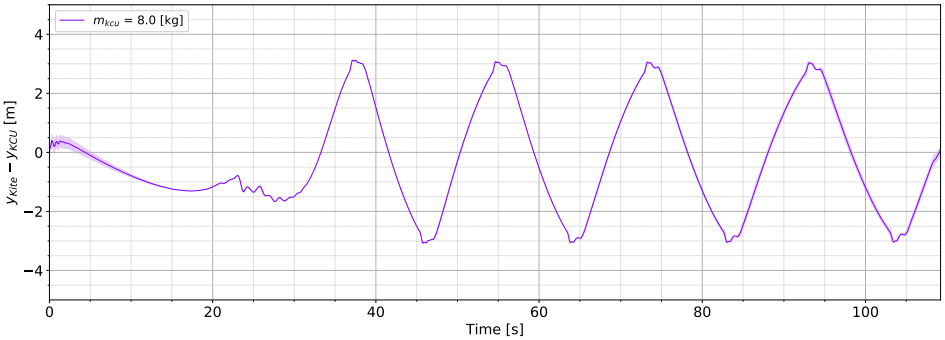

Figure 6.34: Average difference in y position between the kite and KCU for $m_{KCU} = 8$ [kg] and $m_{kite} = 10.5$ [kg] at $v_w = 10$ [m/s]. The shaded region indicates the 2σ bounds.

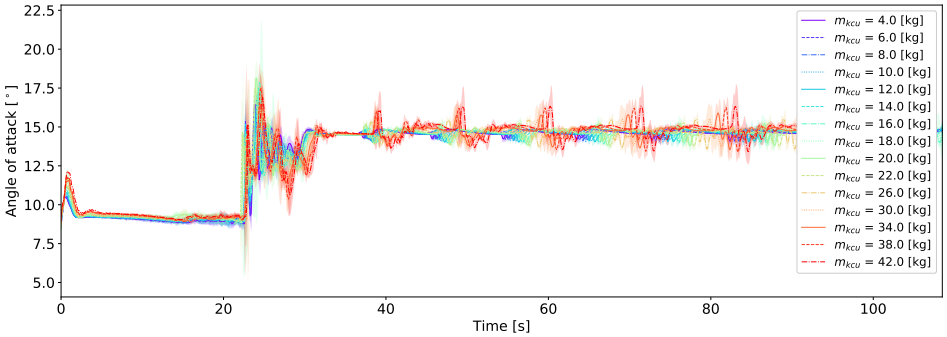

Figure 6.35: Average angle of attack for increasing m_{KCU} at $v_w = 10$ [m/s]. The shaded region indicates the 2σ bounds.

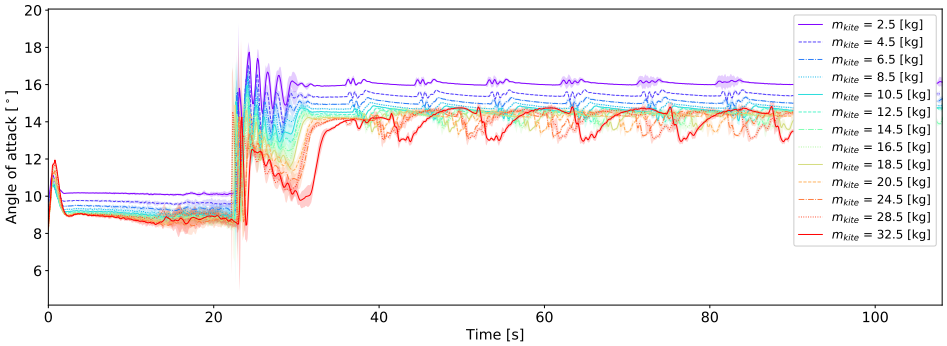

Figure 6.36: Average angle of attack for increasing m_U at $v_w = 10$ [m/s]. The shadedkite region indicates the 2σ bounds.

7

Conclusions and Recommendations

This is the final chapter of this thesis. In the first section, the main findings from the experiments will be summarized. In the second and final section several recommendations will be provided for further research and for Kitepower.

7.1. Conclusions

The findings from the experiments are summarized in Table 7.1 in order to provide a structured overview. The findings are then condensed further below the table after finishing off with a final remark regarding the modeling assumptions and the validity of the outcome.

Table 7.1: Summary of the observations found in the experiments.

Action	Observation for $v_w = 6$ [m/s]	Observation for $v_w = 10$ [m/s]
Increasing KCU drag from 0 to 1.5	• No significant change in cycle power. • Angle of attack does not significantly change. • KCU drag is between 1.5 and 5 percent of the kite drag, for $C_{D,KCU} = 0.5$ and $C_{D,KCU} = 1.5$ respectively.	• 7 % decrease in cycle power caused by lower traction kitespeed. • KCU drag is between 1.5% and 5% of the kite drag, for ($0.5 < C_{D,KCU} < 1.5$. • Angle of attack increases by $< 0.5°$, likely caused by a reduction in kite speed.
Increasing KCU mass	• Increase in cycle power production by >150% for KCU mass increasing from 0 through 26 [kg]. • Increase in cycle power production by >150% for kite mass increasing from 2.5 through 18.5 [kg]. • The increase in average cycle power has two possible causes: 1. Increased velocity in turns, 2. Overall elevation angle of flight path is lower. • No conclusion regarding KCU swing and and kite angle of attack due to too large path variance. • Average cycle power is larger for $m_{kite} \geq m_{KCU}$.	• Increase in cycle power by 40% for a KCU mass increasing from 0 to 42 [kg]. • Increase in cycle power by 100% for a kite mass increasing from 2.5 to 32.5 [kg]. • The increase in power is caused by an reduced elevation angle. • KCU swing observed of $\approx 4.5°$ for $m_{KCU} = 8$ [kg], $m_{kite} = 10.5$ [kg]. • Changes in angle of attack observed, but cause is unclear due to changed flight path and kite speed. • Average cycle power is larger for $m_{kite} \geq m_{KCU}$.

Overall the above table can be further condensed:

- A 7% decrease in overall cycle power is observed for a KCU drag of $C_{D,KCU} = 1.5$.
- Increasing the mass of the KCU or kite has resulted a flight path with a lower altitude (and elevation angle) during traction. This lower flight path generates significantly more energy ($> 40\%$).
- An outward swing has been observed with a magnitude of $\approx 4.5°$, therefore the effect on kite steering will be small.
- The average cycle power is larger for $m_{kite} \geq n_{KCU}$.

Note on the results The results of the experiments rely heavily on the behavior of the flight controller and ground station controller. Furthermore, the kite is assumed to be rigid, which in reality is not the case. The wind field is assumed to be flat where in reality the wind speed is increasing with altitude. The kite model has not been matched with experimental data but parameters have been used that are found in other research. Also, the quantities depend very much on the kite size, therefore for a bigger kite size the effect of e.g. KCU drag is expected to be smaller. Finally, the deformation of the kite and the effects on the aerodynamic forces are not taken into consideration due to the rigid body assumption. All of the above are possible sources for modeling inaccuracies and may influence the conclusion.

7.2. Recommendations

This section provides points of action that can be distilled from the conclusions in the previous section and general findings during the research.

The following topics can be considered as follow-up topics for further research:

- Investigate the effect of increasing kite and KCU mass in a scenario where the effect of elevation angle does not influence the results.
- Currently it is assumed in the kite model that the depower angle adds directly to the angle of attack. It is suggested that to inspect the inclusion of the depower (control input) as linear terms (similar to the angle of attack and sideslip) in the aerodynamic model for the forces and the torque of Ruppert's model by using experimental data.
- Compare the the Ruppert's and Fechner's models (with the modifications described in this report and the above point) through the use of experimental data.
- At the time of writing, the author is unaware of any research regarding the optimal altitude for traction-based AWE systems considering varying wind field, tether drag, elevation angle and system component dynamics. It is suggested to perform research in this direction if this has not already been done.

From a more practical point of view, the following recommendations can be made for Kitepower:

- Support the research suggested above by the placement of the sensor that measures the angle of attack, sideslip and apparent wind speed at a location that is suitable for system identification.
- Instead of using the reference reeling velocity (v_{ref}) provided by the winch controller to determine the motor torque as in section 4.4, instead use the motor torque which is also provided by the winch controller.
- Following the above point, it is interesting to investigate into reducing the power required by retraction since the ground station controller has a large influence on the cost of retraction, especially at the start of the retraction phase.
- During the retraction phase it seems beneficial to steer the kite to the side of the wind window (Appendix O), it is suggested to inspect this to possibly find a less energy consuming retraction path.
- Implement a non-flat wind field instead of the flat wind field that is currently used, since this is expected to have a significant effect on tether force (and power output).

In conclusion The question: 'What are the effects of mass and drag of the kite control unit on the flight behavior of a flexible airborne wind energy system kite during flight?' does not know a straightforward answer. KCU swing has been observed but is small. The drag of the KCU leads to a measurable decrease in cycle power and the average cycle power will be larger if the kite mass is similar or larger than the mass of the KCU. An increasing mass of kite and KCU will lead to an increase in average cycle power under the assumption of a flat wind profile. To more accurately determine the effects of increasing KCU and kite mass, the effect of increasing power due to a lower elevation angle needs to be eliminated.

In order to obtain these results a simulation framework has been built in which Kitepower's flight and groundstation controls have been integrated. Fechner's kite model has been cast into a rigid body description and Ruppert's aerodynamic model is now linear in the parameters. The method with which to identify both Fechner's and Rupperts model parameters with experimental flight data has been laid out. Future research to improve the aerodynamic accuracy of the rigid body kite model should start with gathering experimental flight data and matching Ruppert's and Fechners models, followed by a comparison.

A

Integration of the Tether Drag over a Straight Tether

This appendix is motivated by the definition of drag in [63, equation 43]. In the respective paper it is posed that the tether drag 'is calculated by integrating the incremental torque created by the tether drag over the length of the tether'. However no derivation has been given.

Tether element drag depends on the apparent wind speed which consists of two elements: 1) the sweeping motion of the kite, and 2) the wind speed. Since the wind speed (and direction) is assumed to be constant along the tether, the direction of the drag at different locations along the tether is not equal to that of the drag of the kite. The reason for this is that the velocity of the sweeping motion is linearly reduced when moving radially from the kite towards the ground station over the tether. The wind velocity remains the same, thus the total apparent velocity does not reduce linearly when moving towards the anchor point. An assumption will be made in the following analysis, and the correspondence of the results will show that in [63] the wind speed is not correctly considered in the calculation of the tether drag. The assumption is as follows: *the apparent wind speed reduces linearly with the radial position on the tether.*

Considering a straight tether, the drag experienced by the tether at location x by the aerodynamic load is:

$$D_T(x) = 1/2\rho(2r)(v_a(x))^2 C_{D,T} \tag{A.1}$$

$$v_a(x) = (x/R)v_{a,k} \tag{A.2}$$

Here:

ρ = Density of the air
$v_a(x)$ = The locally experienced apparent wind speed
$v_{a,k}$ = The apparent wind speed experienced by the kite
$C_{D,T}$ = The drag coefficient for the tether
x = The position on the tether
R = The tether length

The torque produced by the aerodynamic load, around the anchor point is:

$$M_{D,T} = \int_0^R D(x)x dx \tag{A.3}$$

$$M_{D,T} = \int_0^R \rho r C_{D,T}(x^3/R^2)v_{a,k}^2 dx \tag{A.4}$$

$$M_{D,T} = 1/4\rho r C_{D,T}(x^4/R^2)v_{a,k}^2\Big]_0^R \tag{A.5}$$

$$M_{D,T} = 1/4\rho r C_{D,T} R^2 v_{a,k}^2 \tag{A.6}$$

The corresponding force at the location of the kite is then determined by dividing by the tether length:

$$D_T = M_{D,T}/R \tag{A.7}$$

$$D_T = 1/4\rho r R v_{a,k}^2 C_{D,T} \tag{A.8}$$

In the paper the following result is obtained (here the assumption is made that the apparent wind speed of the kite is used for V_A):

$$D_{T,Loyd} = 1/2\rho C_{D,T} R\sqrt{T/\sigma} v_{a,k}^2 \tag{A.9}$$

Equating A.8 and A.9 gives, and using $A = 2rR$:

$$D_T = 1/8\rho A v_{a,k}^2 C_{D,T} \tag{A.10}$$

$$1/8\rho A v_{a,k}^2 C_{D,T} = 1/2\rho C_{D,T} R\sqrt{T/\sigma} v_{a,k}^2 \tag{A.11}$$

$$1/4A = R\sqrt{T/\sigma} \tag{A.12}$$

$$A = 4R\sqrt{T/\sigma} \tag{A.13}$$

A is assumed to be equal to the tether reference area. Mr. Loyd states that the tether reference area is equal to $4R\sqrt{A_T}$, where $A_T = T/\sigma$. This corresponds with A.13. Due to the correspondence of the results, it is most likely that Mr. Loyd considered a linear relation between the apparent wind speed and the location of the tether.

B

Wind Field Parameters for the Power Law and Logarithmic Wind Profile Law

Table B.1: Friction coefficient for a variety of landscapes. Adopted from [18], [66].

Landscape type	Friction coefficient, α
Lakes, ocean and smooth hard ground	0.10
Grasslands (ground level)	0.15
Tall crops, hedges and shrubs	0.20
Heavily forested land	0.25
Small town with some trees and shrubs	0.30
City areas with high rise buildings	0.40

Table B.2: Roughness classes and lengths. Adopted from [18], [66].

Roughness class	Description	Roughness length, z_0 (m)
0	Water surface	0.0002
1	Open areas dotted with a handful of windbreaks	0.03
2	Farmland dotted with some windbreaks more than 1km apart	0.1
3	Urban districts and farmland with many windbreaks	0.4
4	Densely populated urban or forest areas	1.6

C

Aerodynamic Models, Reeling Methods and Parameters for Flexible Tethers

C.1. Reeling Methods for Flexible Tethers

Table C.1: An overview of the encountered reeling methods for flexible tether models. An empty entry with a 'based on' reference indicates that it is identical to it's reference. * Most likely

Source	Reeling	Reeling implementation	Based on
[38]	Y	Control of initial tether element length. fixed number of particles	[42]
[68]	Y	Only change length of first element	
[68]	Y	Only change length of first element	
[21]			[22]
[86]	Y	Change tether lengths simultaneously	
[30]	Y	Add new tether element at start with initially zero or very small length	
[62]			[72]
[103]	Y	Two methods: 1. Direct control of the reel-out speed. 2) Direct control of tether tension.	
[22]	N	Fixed length	
[101]	Y	Cable length adjusts by changing the length of the first element.	
[81]	N	Fixed length (laddermill)	
[41]	N	Fixed length	
[19]	N	Fixed length	
[57]			[38]
[42]			[43]
[104] [4]	N	Fixed-length	
[107]	Y	Change rest length of first element. Split when threshold length is reached. Variable state vector	
[14]	Y		[107]
[103]	Y		[107]
[72]	Y		[30]
[13]	Y		[107]*
[109]	N		[107]
[84]	Y		[107]

C.2. Aerodynamic Models for Flexible Tethers

Table C.2: An overview of the encountered aerodynamic models for flexible tethers. An empty entry with a 'based on' reference indicates that it is identical to it's reference. All units are directly taken over from the source papers.

Source	Aerodynamical model	Based on
[38]	average segment drag of neighboring segments.	[42]
[68]	$F_\perp$ integrated over segment length (assuming varying wind field). Forces are distributed over the nodes according to the distribution moment.$C_D = 1.2$	
[68]	$F_\perp$ integrated over segment length (assuming varying wind field). Forces are distributed over the nodes according to the distribution moment.$C_D = 1.2$	
[21]		[22]
[86]	$F_\perp$ drag determined at particle location. $D_\perp = 1$	
[30]	F_D halfway the tether segment. Drag depends on angle of attack. possibly in line with apparent wind velocity (not normal to tether segment) $C_D = 1.056$	
[62]	F_D at particle location, $C_D = 1.1$	[72]
[103]	$F_\perp$, through taking the perpendicular component of the apparent wind speed of the point mass on the element from the point mass to the next point mass.	
[22]	$F_{\perp,x} + F_{\perp,y} + F_{\parallel,z}$, $C_D = 1.065$ $C_F = 0.0017$ [48] Aerodynamic force applied to center of elements	
[101]	$F_\perp + F_\parallel$, fixed $C_\perp$ and $C_\parallel$. Calculated at center of element and distributed over masses.	
[81]		
[41]	$F_\perp + F_\parallel$, $C_{D,\perp} = 0.55$ $C_{D,\parallel} = 0.01$	
[19]	yes	
[57]		[38]
[42]		[43]
[104]	$F_\perp + F_\parallel$ (cross-flow principle), determined at element's center. Varying Cn and Ct depending on Reynolds number.	
[4]		
[107]	$F_\perp + F_\parallel$. Average tether element velocity and fixed C_D. Averaged over 2 tether elements and lumped at node. $C_D = 1.2$	
[14]	F_D at lumped mass location, $C_D = 1.22$	[107]
[103]		[107]
[72]		[30]
[13]	$C_D = 1.22$	[107]*
[109]	$C_{D_\perp} = 1.2$	[107]
[84]	$F_\perp + F_\parallel$. Apparent wind speed at point mass	[107]

C.3. Parameters for Flexible Tethers

Table C.3: An overview of the encountered parameters for flexible tether models. Empty entires either inherited the parameters from the 'based on' reference, or no parameters could be found.

Source	Stiffness	Damping	Diameter	Density	Segments	Based on
[38]	$k_0 = 614600$	$c_0 = 473$ Ns	4mm	$0.013kg/m$		[42]
[68]	$E = 100$ GPa, $k = 500$ Ns/m^2				2	
[68]	$E = 100$ GPa, $k = 500$ Ns/m^2				28	
[21]						[22]
[86]			2mm	970 kg/m^3	$1, ..., 50$	
[30]	$E = 53$ GPa		4mm	700 kg/m^3	300	
[62]	$E = 48.910$ GPa, $k = 6.1462 \times 10^5$ N/m	$c_0 = 473$ Ns				[72]
[103]	$EA = 490.874$ N	$c = 500N/s$	2.5mm	0.004761 kg/m	30	
[22]					50	
[101]						
[81]						
[41]						
[19]						
[57]						[38]
[42]						[43]
[104]						
[4]						
[107]			1mm	1000kg/m^3	15	
[14]	$E = 55$GPa	$c_0 = 30000$ Ns	4mm	960 kg/m^3	25	[107]
[103]	$EA = 490.874$ N	$c = 500N/s$	2.5mm	0.004761 kg/m		[107]
[72]						[30]
[13]	$E = 55$ GPa	$c_0 = 30000$ Ns	4mm	960 kg/m^3		[107]*
[109]			5mm	19.63kg/km	40	[107]
[84]	$E = 55$ GPa, $k_0 = 6.1462 \times 10^5$ N	$c_0 = 473$ Ns	4mm			[107]

D

Definition of the Aerodynamic Angles

The determination of the angle of attack (α) and sideslip (β) angles is described here. All vectors are in the world frame ($*_G$). Figure D.1 shows how the angles are defined.

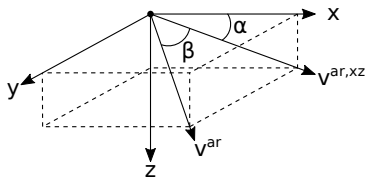

Figure D.1: Definition of the aerodynamic angles α (angle of attack) and β (sideslip).

The aerodynamic angles can be calculated through the orientation of the kite, the velocity of the kite and the windvelocity. The aerodynamic velocity ($\mathbf{v}_G^{ar}$) (not to be confused with the apparent wind speed $\mathbf{v}_G^a$)) is defined as follows:

$$\mathbf{v}_G^{ar} = \mathbf{v}_G^k - \mathbf{v}_G^w \tag{D.1}$$

Calculation of the angle of attack that is valid for all four quadrants and protected against division by zero:

$$\alpha = \begin{cases} \operatorname{atan2}(n,d), \text{ where } \quad n = \mathbf{v}_G^{ar} \cdot \mathbf{e}_G^{z,k}, \quad d = \mathbf{v}_G^{ar} \cdot \mathbf{e}_G^{x,k}, \quad \text{if } \|\mathbf{v}_G^{ar}\| \neq 0 \\ 0 \quad \text{if } \|\mathbf{v}_G^{ar}\| = 0 \end{cases} \tag{D.2}$$

Calculation of the sideslip angle that is valid for $-90° \leq \beta \leq 90°$ and protected against division by zero:

$$\beta = \begin{cases} \operatorname{atan2}(n,d), \text{ where } \quad n = \mathbf{v}_G^{ar} \cdot \mathbf{e}_G^{y,k}, \quad d = \|\mathbf{v}_G^{ar,xz}\|, \quad \mathbf{v}_G^{ar,xz} = \mathbf{v}_G^{ar} - \mathbf{v}_G^{ar} \cdot \mathbf{e}_G^{y,k} \quad \text{if } \|\mathbf{v}_a\| \neq 0 \\ 0 \quad \text{if } \|\mathbf{v}_G^{ar}\| = 0 \end{cases} \tag{D.3}$$

E

Vector Definitions and Transformations

Notation For any vector, the subscript indicates the frame of the vector. The following subscripts are used:

- Global frame: $*_G$
- Kite frame: $*_k$
- Aerodynamic frame: $*_a$

Vector subscripts are used as identifiers. Additionally, the can indicate the original frame of a vector, once a vector has been transformed from one frame to another. The following superscripts are used:

- x, y, z, directional indicators
- L, D, S: directional indicators (Lift, Drag, Side)
- $*_*^{*,G}$ Vector originally expressed in the global frame
- $*_*^{*,k}$ Vector originally expressed in the kite frame
- $*_*^{*,a}$ Vector originally expressed in the aerodynamic frame

Base vectors have unit length and perpendicular to one another. We have the following base vectors:

- Global (inertial) frame: $\mathbf{e}_G^x, \quad \mathbf{e}_G^y, \quad \mathbf{e}_G^z$
- Local (kite) frame: $\mathbf{e}_k^x, \quad \mathbf{e}_k^y, \quad \mathbf{e}_k^z$
- Aerodynamic frame: $\mathbf{e}_a^L, \quad \mathbf{e}_a^D, \quad \mathbf{e}_a^S$

Coordinate transformations are performed by premultiplication by a transformation matrix. The following shows a transformation from the kite frame to the global frame:

$$*_G = {}_G\mathrm{T}_k *_k \tag{E.1}$$
$$\tag{E.2}$$

As an example of the use of the superscripts the kite base vectors expressed in the global frame are as follows:

$$\mathbf{e}_G^{x,k} = {}_G\mathrm{T}_k \mathbf{e}_k^x \tag{E.3}$$
$$\mathbf{e}_G^{x,k} = {}_G\mathrm{T}_k \mathbf{e}_k^y \tag{E.4}$$
$$\mathbf{e}_G^{x,k} = {}_G\mathrm{T}_k \mathbf{e}_k^z \tag{E.5}$$

Furthermore a shorthand notation for a normalized vector is introduced:

$$\hat{\mathbf{x}} = \frac{\mathbf{x}}{\|\mathbf{x}\|} \tag{E.6}$$

The dot notation for a quantity derived with respect to time is used:

$$\dot{x} = \frac{d}{dt}x \tag{E.7}$$

$$\ddot{x} = \frac{d^2}{dt^2}x \tag{E.8}$$

Frame definitions Each frame is spanned by three base vectors.

The kite frame base vectors are $\mathbf{e}_K^x, \mathbf{e}_K^y, \mathbf{e}_K^z$, where the x-direction points forward, the z-direction downward and consequently the y-direction points to the right side of the kite.

The global frame base vectors are $\mathbf{e}_G^x, \mathbf{e}_G^y, \mathbf{e}_G^z$. A location on the surface of the earth is assumed where the x-direction points north, the y-direction points east and the z-direction points to the center of the earth (perpendicularly down to the surface).

The aerodynamic base vectors expressed in the global frame are:

$$\mathbf{e}_G^L = \hat{\mathbf{v}}_G^a \times \mathbf{e}_G^{y,k} \tag{E.9}$$

$$\mathbf{e}_G^D = \hat{\mathbf{v}}_G^a \tag{E.10}$$

$$\mathbf{e}_G^S = \mathbf{e}_k^L \times \mathbf{e}_k^D \tag{E.11}$$

F

Model Parameters

Table F.1: Kite model parameters

Parameter	Value	Description	Source
Kite type	V3B	Kite type indicator	Kitepower
m_k	10.5 [kg]	Kite mass	[84]
$A_{k,t}$	18.18 [m^2]	Projected area of the kite on the xy-plane	[84]
$A_{k,s}$	2.38 [m^2]	Projected area of the kite on the xz-plane	[84]
l_b	8.08 [m]	Bridle length	Figure L.1
δ_d^{max}	45	Maximum depower input	
α_d^{min}	-60	Minimum depower angle	
α_d^{max}	5	Maximum depower angle	
h_k	3.13 [m]	Kite height	Figure L.1
w_k	8.23 [m]	Kite width	Figure L.1
J_k	$\begin{bmatrix} 84.79 & 0.00 & 0.66 \\ 0.00 & 13.23 & 0.00 \\ 0.66 & 0.00 & 83.01 \end{bmatrix}$	Kite inertia tensor	Appendix H

Table F.2: Tether model parameters

Parameter	Value	Description	Source
C_D^t	0.96 [-]	Tether drag coefficient	[38]
n_{max}	20 [-]	Amount of tether segments	
l	5 [m]	Tether segment length	
d	0.004 [m]	Tether diameter	[84]
ρ_t	0.013 [kg/m]	Tether weight per unit length	[42]

Table F.3: KCU model parameters

Parameter	Value	Description	Source
m_{KCU}^t	8.4 [kg]	Mass	[77]
$C_{D,KCU}$	1 [-]	Drag coefficient	
A_{KCU}	0.08 [m^2]	Frontal surface area	

G

Rigid Body Models

Table G.1: An overview of the different definition of the aerodynamic coefficients for the aerodynamic models of rigid-body kite models.

	Ruppert	Knappskog	Williams	Breukels
$c_a^{L,F}$	$c_L(\alpha)$	$c_{l,\max}\sin(c_{ls}\alpha_a)$	$c_{L_0} + c_{L_\alpha}\alpha + c_{L_\delta}(0.5(\delta_L+\delta_R)-\delta_{ac}) + c_{L_q}\frac{\omega_y \bar{c}}{2\lvert v_{\text{rel}}\rvert}$	
$c_a^{D,F}$	$c_D(\alpha)$	$k_d c_l^2 + c_{dm}$	$c_{D_0} + c_{D_\alpha}\alpha + c_{D_{\alpha^2}}\alpha^2 + c_{D_\delta}(0.5(\delta_L+\delta_R)-\delta_{ac}) + c_{D_q}\frac{\omega_y \bar{c}}{2\lvert v_{\text{rel}}\rvert}$	
$c_a^{S,F}$	$A_{k,s}/A_{k,p}c_S(\beta)$	$A_{k,s}/A_{k,p}c_\beta\beta$		
$c_k^{x,F}$			$c_D\cos\alpha - c_L\sin\alpha$	$c_{X_0} + c_{X_\alpha}\alpha + c_{X_{\hat{x}}}\frac{\hat{x}_{\text{baL}}}{\bar{c}}$
$c_k^{y,F}$			$c_{Y_\beta}\beta + c_{Y_\delta}(\delta_R-\delta_L) + c_{Y_r}\frac{\omega_z b}{2\lvert v_{\text{rel}}\rvert} + c_{Y_p}\frac{\omega_x b}{2\lvert v_{\text{rel}}\rvert}$	$c_{Y_\beta}\beta + c_{Y_{\dot{\beta}}}\dot{\beta} + c_{Y_r}\frac{rb}{2V_a} + c_{Y_{x_L}}\frac{\hat{x}_{\text{baL}}}{b} + c_{Y_{x_R}}\frac{\hat{x}_{\text{baR}}}{b}$
$c_k^{z,F}$			$c_L\cos\alpha + c_D\sin\alpha$	$c_{Z_0} + c_{Z_\alpha}\alpha + c_{Z_q}\frac{q\bar{c}}{V_a} + c_{Z_{\hat{x}}}\frac{\hat{x}_{\text{ba}}}{\bar{c}}$
$c_k^{x,T}$			$c_{l_0} + c_{l_\beta}\beta + c_{l_p}\frac{\omega_x b}{2\lvert v_{\text{rel}}\rvert} + c_{l_r}\frac{\omega_z b}{2\lvert v_{\text{rel}}\rvert} + c_{l_S}(\delta_R-\delta_L)$	$c_{l_\beta}\beta + c_{l_r}\frac{rb}{2V_a} + c_{l_{x_L}}\frac{\hat{x}_{\text{baL}}}{b} + c_{l_{x_R}}\frac{\hat{x}_{\text{baR}}}{b}$
$c_k^{y,T}$			$c_{m_0} + c_{m_\alpha}\alpha + c_{m_q}\frac{\omega_y \bar{c}}{2\lvert v_{\text{rel}}\rvert} + c_{m_\delta}(0.5(\delta_L+\delta_R)-\delta_{ac})$	$c_{m_0} + c_{m_\alpha}\alpha + c_{m_q}\frac{q\bar{c}}{V_a} + c_{m_{\hat{x}}}\frac{\hat{x}_{\text{ba}}}{\bar{c}}$
$c_k^{z,T}$	$c_{z,\delta_s}\delta_s + c_{z,\beta}\beta + c_{z,r}\frac{br}{\lvert v_a\rvert} + c_{z,g}\frac{2h\mathbf{F}_G^g\cdot\mathbf{e}_k^y}{\rho A_{k,t} b\lvert v_a\rvert^2}$	$-c_{ks}\beta_s + c_{k,\delta c}\delta_l - c_{kd}\beta_b/\left(\frac{1}{2}\rho_{air}w_e^2 bA\right)$	$c_{n_0} + c_{n_\beta}\beta + c_{n_p}\frac{\omega_x b}{2\lvert v_{\text{rel}}\rvert} + c_{n_r}\frac{\omega_z b}{2\lvert v_{\text{rel}}\rvert} + c_{n_\delta}(\delta_R-\delta_L)$	$c_n = c_{n_\beta}\beta + c_{n_r}\frac{rb}{2V_a} + c_{n_{x_L}}\frac{\hat{x}_{\text{baL}}}{b} + c_{n_{x_R}}\frac{\hat{x}_{\text{baR}}}{b}$

H

Determination of the Inertia Tensor

The method for obtaining an estimate of the inertia tensor will be described here. The method uses 3D drawings of the kite, known values for material weight and a measurement of the kite weight. The kite consists of a leading edge, several struts and the canopy (Figure H.1) which in turn are made of materials tabulated in Table H.1.

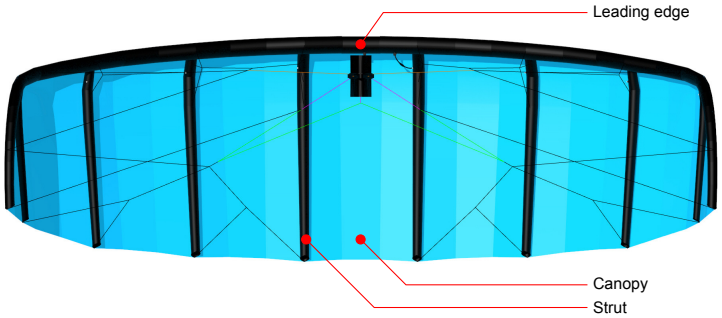

Figure H.1: Kite components. Leading edge: continuous tube from left tip to right at the front of the kite. Canopy: canvas placed connected to the leading edge and covering the struts. Struts: Tubes placed along the longitudinal axis of the kite, connected in the front to the leading edge.

Table H.1: Kite components, materials and material weights. The leading edge and the struts consist of two types of materials.

	Weight $[kg/m^2]$	Canopy	Leading edge	Struts
Ripstop	0.05	X		
Dacron	0.16		X	X
TPU	0.12		X	X

The total surface area per component has been determined with the aid of Rhino CAD software [12] (Table H.1). The component weights can be determined from the material weights combined with the component surface areas. since the component weights did not add up to the total kite weight, a correction factor of 2.21 has been applied. The results are shown in Table H.2.

Table H.2: Component surface area and weight.

	Area	Weight $[kg]$	Corrected weight $[kg]$
Canopy	25.5	1.276	2.82
Leading edge	5.5	1.544	3.41
Struts	7.7	2.156	4.77
Total		4.98	11.00

The second moment of inertia ([kgm^2]) of each component around its own center of mass equals the area moment of inertia [m^4] multiplied by the corrected specific material weight [kg/m^2]. The area moments of inertia have also been determined with the aid of Rhino CAD software [12] and are shown in Table H.3 alongside the resulting component moments of inertia.

Table H.3: Area moments and second moments of inertia per component around the component center of mass.

	A_{xx} [m^4]	A_{yy} [m^4]	A_{zz} [m^4]	I_{xx} [kgm^2]	I_{yy} [kgm^2]	I_{zz} [kgm^2]
Canopy	191.14	27.06	187.43	21.13	2.99	20.72
Leading edge	33.94	1.78	32.37	21.01	1.10	20.03
Struts	68.33	9.93	64.03	42.29	6.15	39.63
Sum	-	-	-	84.43	10.24	80.63

To obtain the total inertia tensor, the inertia's of the individual components will be combined using the parallel axis theorem, using (Equation H.1) and knowledge of the locations of the component center of masses with respect to the total center of mass (Table H.4). The added inertias due to the displaced component centers of mass can be found in Table H.5. The resulting total inertia tensors is shown in Equation H.2.

$$\begin{aligned} Ixx &= m(dy^2 + dz^2) \\ Iyy &= m(dx^2 + dz^2) \\ Izz &= m(dx^2 + dy^2) \\ Ixy &= m(dx \cdot dy) \\ Ixz &= m(dx \cdot dz) \\ Iyz &= m(dy \cdot dz) \end{aligned} \tag{H.1}$$

Table H.4: Component distances to kite center of mass.

	x [m]	y [m]	z [m]
Canopy	-0.34	0.00	-0.12
Leading edge	0.73	0.00	-0.19
Struts	-0.32	0.00	-0.20

Table H.5: Additional inertia's due to distance of components with respect to the total center of mass.

	I_{xx} [kgm^2]	I_{yy} [kgm^2]	I_{zz} [kgm^2]	I_{xy} [kgm^2]	I_{xy} [kgm^2]	I_{yz} [kgm^2]
Canopy	0.04	0.36	0.32	0.00	0.11	0.00
Leading edge	0.12	1.93	1.81	0.00	-0.46	0.00
Struts	0.20	0.70	0.50	0.00	-0.31	0.00
Total	0.36	2.99	2.63	0.00	-0.66	0.00

$$\mathbf{J} = \begin{bmatrix} I_{xx} & -I_{xy} & -I_{xz} \\ -I_{xy} & I_{yy} & -I_{yz} \\ -I_{xz} & -I_{yz} & I_{zz} \end{bmatrix} = \begin{bmatrix} 84.79 & 0.00 & 0.66 \\ 0.00 & 13.23 & 0.00 \\ 0.66 & 0.00 & 83.01 \end{bmatrix} \tag{H.2}$$

Tether Model Verification

I.1. Static Catenary Curve

In this section a simulated tether is attached to the origin and a horizontal force is applied to the free end of the tether. It is expected that tether elements lie on the catenary curve (Equation I.2). The results are visualized in Figure I.1. Additionally, the error in vertical displacement of the final element together with error statistics are provided.

The tether is initialized vertically. Due to the force the tether will start to move. In order to minimize the effects of tether dynamics on the results, a convergence criterion has been specified and velocity damping in the form of aerodynamic drag is applied to each element to improve convergence speed.

The convergence criterion dictates that the sum of the absolute position changes (Equation I.1) per time step of each element must be smaller than a given threshold ϵ. Experiment specific parameters can be found in Table I.1.

$$\delta = \sum_{i=1}^{i=n} \left((x_i[k-1] - x_i[k])^2 + (y_i[k-1] - y_i[k])^2 \right)^{1/2} \tag{I.1}$$

k = Time step [-]
n_s = Number of tether segments [-]
i = Tether element index [-]
$x_i[k]$ = Element number i, position in x direction at timestep k [m]
$y_i[k]$ = Element number i, position in y direction at timestep k [m]
δ = Sum of absolute position changes [m]
ϵ = Threshold [m]

Table I.1: Experiment parameters for the catenary tether verification.

Parameter	Value	Unit
dt	0.0083	[s]
ϵ	$5e^{-5}$	[m]
n_s	40	[-]
l_t	20	[m]
ρ_t	2.0	[kg/m]
g	9.81	[ms^{-2}]

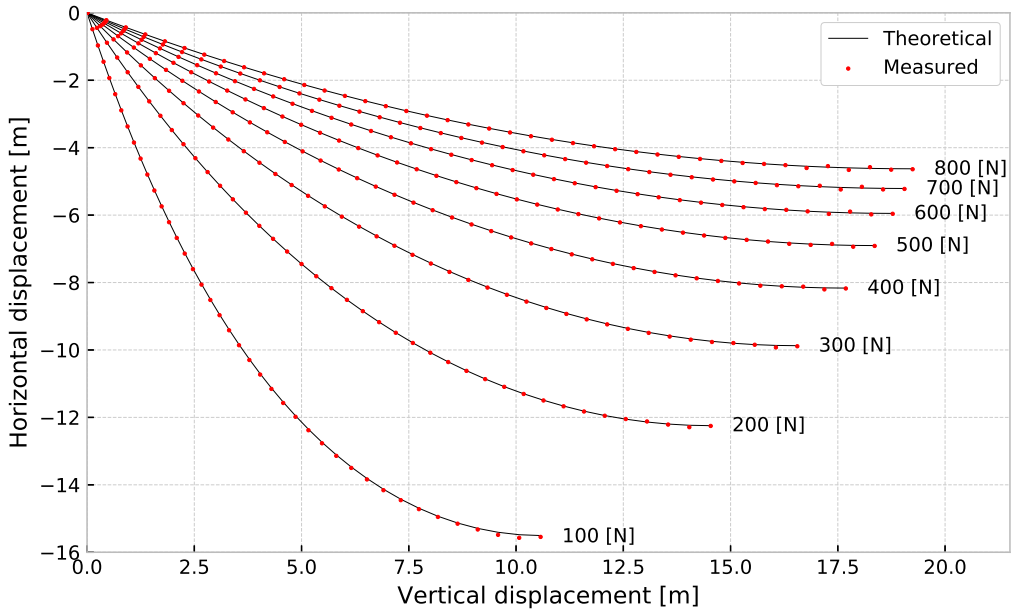

Figure I.1: Comparison between the analytical catenary curve and the measured positions of the tether elements.

In order to compare the results with the catenary curve, a horizontal and vertical transformation has been applied. This leads to the following modified catenary equation

$$\begin{aligned} y &= a\cosh\left(\frac{x - x_m}{a}\right) - a\cosh\left(\frac{x_m}{a}\right) \\ a &= \frac{F_t}{gw} \\ w &= \left(\frac{m_s}{l_s}\right) \end{aligned} \tag{I.2}$$

a = Catenary coefficient [ms^{-4}]
x = Position in the x direction [m]
x_m = X position of last tether element [m]
F_t = Applied tether force in the x-direction [N]
g = Gravitational acceleration
w = Tether unit length element weight
m_s = Tether segment mass [kg]
l_s = Tether segment length [m]

The curve formed by the locations of the tether elements corresponds to that of the analytical catenary curve as can be seen in Figure I.1. Table I.2 show the absolute and percentage-wise errors in vertical displacement. Part of the error can be attributed to the remaining movement of the elements. The percentage-wise error is determined with respect to the expected vertical displacement corresponding to the analytical catenary curve. It can be observed that the error found in this experiment is maximally 0.11%. The standard deviation indicates that the results show no big fluctuations between different input forces.

Table I.2: List of vertical displacement errors for different horizontally applied forces. The vertical displacement error is absolute. The percentage is determine with respect to the true vertical displacement determined via the analytical catenary curve.

Force [N]	Vertical displacement error [m]	Vertical displacement error [%]
50	0.019	0.110
100	0.009	0.058
200	0.003	0.022
300	0.001	0.012
400	0.001	0.008
500	0.000	0.004
600	0.000	0.002
700	0.000	0.003
800	0.000	0.002
900	0.000	0.000

Table I.3: Statistics for Table I.2. This table shows the mean absolute error, maximal absolute error and the standard deviation of the errors.

Statistic	Absolute error [m]	Absolute error [%]
mean	0.003	0.022
max	0.019	0.110
std	0.006	0.035

I.2. Aerodynamic Drag

The goal of this section is to explain the method used for the verification of the aerodynamic drag in the tether model. For this experiment the tether is divided up into 63 tether segments which are rigidly connected such that the tether is one straight rod. The tether is constrained at one and and the other end is free. The tether is initialized horizontally and then released in order to swing freely.

For an increasing amount of tether segments, the tether drag is evaluated for each segment according to Equation 4.16. The total torque caused by the aerodynamic drag is determined by the multiplication of the drag force per segment multiplied by its distance to the attachment point. The total torque is then compared with the theoretical torques which is determined analytically through the integration of the drag over the length of the tether and is shown in Equation 4.14.

During this procedure the forces are not applied to the tether and the inertia of the tether remains constant. Therefore the swinging behavior of the tether is not influenced by changing the evaluation of the drag over the tether.

This experiment is performed for an increasing number of groups and thus an increasing number of segments, since the number of segments is a logical consequence of the group size. The group size is the amount of tether segments that are considered to be one. For example, a group size of one means that all segments act as individual segments, resulting in the maximum number of segments. A group size of two means that two segments together form a group, resulting in half the amount of segments. A group size of 63 means that all segments act as one group and thus the total number of segments is one. Groups are formed from the end of the tether towards the attachment, the remaining segments that form an incomplete group form a final group. As a final example, a group size of 50 results in two groups: one of 50 segments and one of the remaining 13 segments.

Figure I.2 shows that for an increasing amount of segments, the solution converges to the analytical solution.

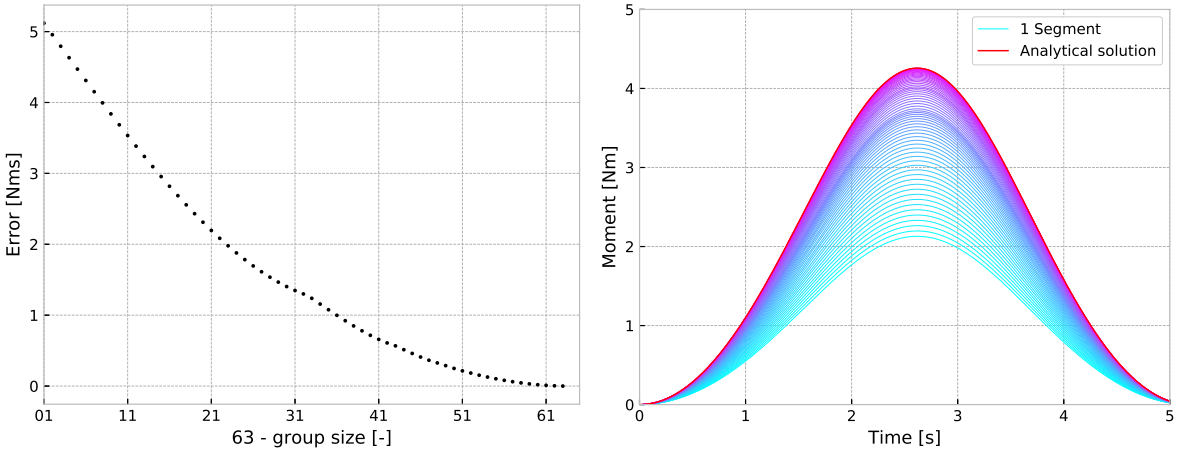

Figure I.2: Left: Error in integral torque between the analytical solution and the segmented drag evaluation. Right: Instantaneous drag induced torque over time for an increasing number of segments. Here the lowest light blue curve represents the drag induced torque when one element is used for the evaluation of the torque and the topmost (red) curve is the analytical solution. The number of segments increases with the color changing from light blue to red.

J

Dynamic Engine Verification

In order to built trust in the physical correctness of the Nvidia PhysX, an experiment has been performed. In this experiment a compound pendulum is swung with a low amplitude. The smaller the starting angle, the closer the results should be to the natural frequency. If the frequency is near the expected frequency, this provides trust in the physical correctness of the physics engine.

The natural frequency of a compound pendulum, using a small angle approximation can be determined via Equation J.1. The compound pendulum exists of one mass which is displaced from the center of rotation. The total inertia of a compound pendulum around the axis of rotation can be determined through the parallel axis theorem (Equation J.2).

$$\omega = \sqrt{\left(\frac{mgl}{I_t}\right)} \quad [rad/s] \tag{J.1}$$

$$I_t = I_G + ml^2 \tag{J.2}$$

Here I_G is the moment of inertia of the sphere around its local axis of rotation, m is the mass of the sphere and l is the distance of the sphere to the point of rotation.

The compound pendulum is given an impulse at initialization, resulting in a small maximum angle (θ_{max}). From the time response the peak locations are located and the average period length is determined. The frequency is derived from the average period length.

The measured frequency is 0.4970 [Hz], whereas the expected frequency: 0.4965 [Hz] corresponding to a percentage wise error of 0.1007%, which is though to be sufficiently small to trust the physical correctness of the physics simulation engine.

Table J.1: Pendulum experiment parameters.

Parameter	Value	Unit
g	9.810	[ms^{-2}]
m	1.000	[kg]
l	1.000	[m]
I_G	0.004	[kgm^2]
dt	0.005	[s]
θ_{max}	0.032	[rad]

K

Rigid Body Model Description of Fechner's Kite Model

The rigid body description of Fechner's 5P model is derived in this appendix. Knowledge of Fechners model is assumed.

Aerodynamic forces Starting with the forces, the forces shown below are a direct copy from the model paper with the exception of k_D, which has been removed since it is a redundant variable and its effects can be incorporated in the lift and drag coefficients .In the equations below it is important to mind the different order of the multiplication (cross product) for points C and D.

$$\mathbf{F}_L^B = \frac{1}{2}\rho(\mathbf{v}_{a,B}^{xz})^2 A C_L(\alpha_B)\frac{\mathbf{v}_{a,B}\times\mathbf{e}_G^{k,y}}{\|\mathbf{v}_{a,B}\times\mathbf{e}_G^{k,y}\|} \tag{K.1}$$

$$\mathbf{F}_L^C = \frac{1}{2}\rho(\mathbf{v}_{a,C}^{xy})^2 A_s C_L(\alpha_C)\frac{\mathbf{v}_{a,C}\times\mathbf{e}_G^{k,z}}{\|\mathbf{v}_{a,C}\times\mathbf{e}_G^{k,z}\|} \tag{K.2}$$

$$\mathbf{F}_L^D = \frac{1}{2}\rho(\mathbf{v}_{a,D}^{xy})^2 A_s C_L(\alpha_D)\frac{\mathbf{e}_G^{k,z}\times\mathbf{v}_{a,D}}{\|\mathbf{e}_G^{k,z}\times\mathbf{v}_{a,D}\|} \tag{K.3}$$

$$\mathbf{F}_D^B = \frac{1}{2}\rho(\mathbf{v}_{a,B})^2 A C_D(\alpha_B)\frac{\mathbf{v}_{a,B}}{\|\mathbf{v}_{a,B}\|} \tag{K.4}$$

$$\mathbf{F}_D^C = \frac{1}{2}\rho(\mathbf{v}_{a,C})^2 A C_D(\alpha_C)\frac{\mathbf{v}_{a,C}}{\|\mathbf{v}_{a,C}\|} \tag{K.5}$$

$$\mathbf{F}_D^D = \frac{1}{2}\rho(\mathbf{v}_{a,D})^2 A C_D(\alpha_D)\frac{\mathbf{v}_{a,D}}{\|\mathbf{v}_{a,D}\|} \tag{K.6}$$

Aerodynamic torques The aerodynamic torques can be determined through the cross product of the location of the respective points and the aerodynamic force:

$$\mathbf{T} = \mathbf{r}\times\mathbf{F} \tag{K.7}$$

$$\mathbf{T}_L^B = \mathbf{r}_B \times \mathbf{F}_L^B \tag{K.8}$$
$$\mathbf{T}_L^C = \mathbf{r}_C \times \mathbf{F}_L^C \tag{K.9}$$
$$\mathbf{T}_L^D = \mathbf{r}_D \times \mathbf{F}_L^D \tag{K.10}$$
$$\mathbf{T}_D^B = \mathbf{r}_B \times \mathbf{F}_D^B \tag{K.11}$$
$$\mathbf{T}_D^C = \mathbf{r}_C \times \mathbf{F}_D^C \tag{K.12}$$
$$\mathbf{T}_D^D = \mathbf{r}_D \times \mathbf{F}_D^D \tag{K.13}$$

The center of gravity is chosen as the origin. For the total aerodynamic torque ($\mathbf{T}_G^a$) we have :

$$\mathbf{T}_G^a = \sum \mathbf{T} = \mathbf{T}_L^B + \mathbf{T}_L^C + \mathbf{T}_L^D + \mathbf{T}_D^B + \mathbf{T}_D^C + \mathbf{T}_D^D \tag{K.14}$$

(K.15)

Local apparent wind velocities The results of the previously described forces and torques depend on the local apparent wind velocities. The local apparent wind velocities at points B, C and D are equal to the velocity of the kite center P_c superimposed with the rotational rates multiplied with the distances of the points. Instead of using P_c as origin (as in the paper), the center of gravity will function as origin. This leads to the following expressions for the apparent wind velocities of points B, C and D: Motion of a body:

$$\mathbf{v}_p = \mathbf{v}_c + \boldsymbol{\omega} \times \mathbf{r}_B \tag{K.16}$$

$\mathbf{v}_c$ is velocity of body center. $\mathbf{v}_p$ is velocity of point on body. This gives the following apparent wind velocities:

$$\mathbf{v}_{a,B} = \mathbf{v}_w - \mathbf{v}_O - \boldsymbol{\omega} \times \mathbf{r}_B \tag{K.17}$$
$$\mathbf{v}_{a,C} = \mathbf{v}_w - \mathbf{v}_O - \boldsymbol{\omega} \times \mathbf{r}_C \tag{K.18}$$
$$\mathbf{v}_{a,D} = \mathbf{v}_w - \mathbf{v}_O - \boldsymbol{\omega} \times \mathbf{r}_D \tag{K.19}$$

Beware: $\mathbf{r}_B, \mathbf{r}_C$ and $\mathbf{r}_D$ are defined differently than in Fechner's paper and have been determined in Appendix L.

Local angles of attack The aerodynamic coefficients in the above described forces and torques depend on the local angle of attack. The definition of the local angle of attack has been simplified. The steering influences and angle offsets are incorporated elsewhere in the aerodynamic model. The local aerodynamic angles are shown in Equation K.20. Figure K.1 can be used as a reference.

$$\begin{aligned} \mathbf{v}_{ae} &= -\mathbf{v}_a \\ \alpha_B &= \arctan_2(\mathbf{v}_{ae,B}^{xz} \cdot \mathbf{e}_G^{k,z}, \mathbf{v}_{ae,B}^{xz} \cdot \mathbf{e}_G^{k,x}) \\ \alpha_C &= \arctan_2(-\mathbf{v}_{ae,C}^{xy} \cdot \mathbf{e}_G^{k,y}, \mathbf{v}_{ae,C}^{xy} \cdot \mathbf{e}_G^{k,x}) \\ \alpha_D &= \arctan_2(\mathbf{v}_{ae,D}^{xy} \cdot \mathbf{e}_G^{k,y}, \mathbf{v}_{ae,D}^{xy} \cdot \mathbf{e}_G^{k,x}) \end{aligned} \tag{K.20}$$

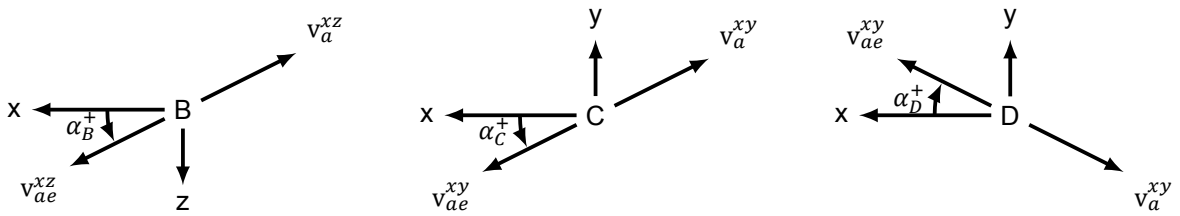

Figure K.1: Definition of the angles of attack in points A, B and C.

Total aerodynamic model

$$\begin{bmatrix}\mathbf{F}_G^a\\ \mathbf{T}_G^a\end{bmatrix} = \frac{1}{2}\rho\begin{bmatrix}\mathbf{v}_{00} & \mathbf{v}_{01} & \mathbf{v}_{02} & \mathbf{v}_{03} & \mathbf{v}_{04} & \mathbf{v}_{05}\\ \mathbf{v}_{06} & \mathbf{v}_{07} & \mathbf{v}_{08} & \mathbf{v}_{09} & \mathbf{v}_{10} & \mathbf{v}_{11}\end{bmatrix}\begin{bmatrix}C_L(\alpha_B,\delta_D)\\ C_L(\alpha_C,\delta_D)\\ C_L(\alpha_D,\delta_s,\delta_D)\\ C_D(\alpha_B,\delta_s,\delta_D)\\ C_D(\alpha_C,\delta_s,\delta_D)\\ C_D(\alpha_D,\delta_s,\delta_D)\end{bmatrix} \tag{K.21}$$

With:

$$\mathbf{v}_{00} = (\mathbf{v}_{a,B}^{xz})^2 A\frac{\mathbf{v}_{a,B}\times\mathbf{e}_G^{k,y}}{\|\mathbf{v}_{a,B}\times\mathbf{e}_G^{k,y}\|} \qquad \mathbf{v}_{01} = (\mathbf{v}_{a,C}^{xy})^2 A_s\frac{\mathbf{v}_{a,C}\times\mathbf{e}_G^{k,z}}{\|\mathbf{v}_{a,C}\times\mathbf{e}_G^{k,z}\|} \tag{K.22}$$

$$\mathbf{v}_{02} = (\mathbf{v}_{a,D}^{xy})^2 A_s\frac{\mathbf{e}_G^{k,z}\times\mathbf{v}_{a,D}}{\|\mathbf{e}_G^{k,z}\times\mathbf{v}_{a,D}\|} \qquad \mathbf{v}_{03} = (\mathbf{v}_{a,B})^2 A\frac{\mathbf{v}_{a,B}}{\|\mathbf{v}_{a,B}\|} \tag{K.23}$$

$$\mathbf{v}_{04} = (\mathbf{v}_{a,C})^2 A_s\frac{\mathbf{v}_{a,C}}{\|\mathbf{v}_{a,C}\|} \qquad \mathbf{v}_{05} = (\mathbf{v}_{a,D})^2 A_s\frac{\mathbf{v}_{a,D}}{\|\mathbf{v}_{a,D}\|} \tag{K.24}$$

$$\mathbf{v}_{06} = (\mathbf{v}_{a,B}^{xz})^2 A\frac{\mathbf{r}_B\times(\mathbf{v}_{a,B}\times\mathbf{e}_G^{k,y})}{\|\mathbf{v}_{a,B}\times\mathbf{e}_G^{k,y}\|} \qquad \mathbf{v}_{07} = (\mathbf{v}_{a,C}^{xy})^2 A_s\frac{\mathbf{r}_C\times(\mathbf{v}_{a,C}\times\mathbf{e}_G^{k,z})}{\|\mathbf{v}_{a,C}\times\mathbf{e}_G^{k,z}\|} \tag{K.25}$$

$$\mathbf{v}_{08} = (\mathbf{v}_{a,D}^{xy})^2 A_s\frac{\mathbf{r}_D\times(\mathbf{e}_G^{k,z}\times\mathbf{v}_{a,D})}{\|\mathbf{e}_G^{k,z}\times\mathbf{v}_{a,D}\|} \qquad \mathbf{v}_{09} = (\mathbf{v}_{a,B})^2 A\frac{\mathbf{r}_B\times\mathbf{v}_{a,B}}{\|\mathbf{v}_{a,B}\|} \tag{K.26}$$

$$\mathbf{v}_{10} = (\mathbf{v}_{a,C})^2 A_s\frac{\mathbf{r}_C\times\mathbf{v}_{a,C}}{\|\mathbf{v}_{a,C}\|} \qquad \mathbf{v}_{11} = (\mathbf{v}_{a,D})^2 A_s\frac{\mathbf{r}_D\times\mathbf{v}_{a,D}}{\|\mathbf{v}_{a,D}\|} \tag{K.27}$$

Reparametrized lift-drag equations for points C and D $\delta_s^C = -\delta_s^D$, depower contribution does not change sign, contribution to points C and D is equal.

$$C_L^B(\alpha_B,\delta_D) = C_0^{L,t} + C_1^{L,t}\alpha_B + C_2^{L,t}\alpha_B^2 + C_3^{L,t}\delta_D + C_4^{L,t}\delta_D^2 \tag{K.28}$$

$$C_D^B(\alpha_B,\delta_D) = C_0^{D,t} + C_1^{D,t}\alpha_B + C_2^{D,t}\alpha_B^2 + C_3^{D,t}\delta_D + C_4^{D,t}\delta_D^2 \tag{K.29}$$

$$C_L^C(\alpha_C,\delta_s,\delta_D) = C_0^{L,s} + C_1^{L,s}\alpha_C + C_2^{L,s}\alpha_C^2 + C_3^{L,s}\delta_s + C_4^{L,s}\delta_s^2 + C_5^{L,s}\delta_D \tag{K.30}$$

$$C_D^C(\alpha_C,\delta_s,\delta_D) = C_0^{D,s} + C_1^{D,s}\alpha_C + C_2^{D,s}\alpha_C^2 + C_3^{D,s}\delta_s + C_4^{D,s}\delta_s^2 + C_5^{D,s}\delta_D \tag{K.31}$$

$$C_L^D(\alpha_D,\delta_s,\delta_D) = C_0^{L,s} + C_1^{L,s}\alpha_D + C_2^{L,s}\alpha_D^2 - C_3^{L,s}\delta_s + C_4^{L,s}\delta_s^2 + C_5^{L,s}\delta_D \tag{K.32}$$

$$C_D^D(\alpha_D,\delta_s,\delta_D) = C_0^{D,s} + C_1^{D,s}\alpha_D + C_2^{D,s}\alpha_D^2 - C_3^{D,s}\delta_s + C_4^{D,s}\delta_s^2 + C_5^{D,s}\delta_D \tag{K.33}$$

Aerodynamic parameters for point C and D identical. 5 parameters for lift n point A, 5 for Drag 6 parameters for lift in point and 6 for drag. Same parameters for point D. Total 5*2 + 6*2 = 22 parameters. Parameter vector:

$$\boldsymbol{\theta} = \begin{bmatrix} C_0^{L,t} & C_1^{L,t} & C_2^{L,t} & C_3^{L,t} & C_4^{L,t} & C_0^{L,s} & C_1^{L,s} & C_2^{L,s} & C_3^{L,s} & C_4^{L,s} & C_5^{L,s} & \dots \\ C_0^{D,t} & C_1^{D,t} & C_2^{D,t} & C_3^{D,t} & C_4^{D,t} & C_0^{D,s} & C_1^{D,s} & C_2^{D,s} & C_3^{D,s} & C_4^{D,s} & C_5^{D,s} & \end{bmatrix}^T \tag{K.34}$$

$$a_{00} = \mathbf{v}_{00} \qquad = a_{22} = \mathbf{v}_{06} \tag{K.35}$$
$$a_{01} = \alpha_B \mathbf{v}_{00} \qquad = a_{23} = \alpha_B \mathbf{v}_{06} \tag{K.36}$$
$$a_{02} = \alpha_B^2 \mathbf{v}_{00} \qquad = a_{24} = \alpha_B^2 \mathbf{v}_{06} \tag{K.37}$$
$$a_{03} = \delta_D \mathbf{v}_{00} \qquad = a_{25} = \delta_D \mathbf{v}_{06} \tag{K.38}$$
$$a_{04} = \delta_D^2 \mathbf{v}_{00} \qquad = a_{26} = \delta_D^2 \mathbf{v}_{06} \tag{K.39}$$
$$a_{05} = \mathbf{v}_{01} + \mathbf{v}_{02} \qquad = a_{27} = \mathbf{v}_{07} + \mathbf{v}_{08} \tag{K.40}$$
$$a_{06} = \alpha_C \mathbf{v}_{01} + \alpha_D \mathbf{v}_{02} \qquad = a_{28} = \alpha_C \mathbf{v}_{07} + \alpha_D \mathbf{v}_{08} \tag{K.41}$$
$$a_{07} = \alpha_C^2 \mathbf{v}_{01} + \alpha_D^2 \mathbf{v}_{02} \qquad = a_{29} = \alpha_C^2 \mathbf{v}_{07} + \alpha_D^2 \mathbf{v}_{08} \tag{K.42}$$
$$a_{08} = \delta_S \mathbf{v}_{01} - \delta_S \mathbf{v}_{02} \qquad = a_{30} = \delta_S \mathbf{v}_{07} - \delta_S \mathbf{v}_{08} \tag{K.43}$$
$$a_{09} = \delta_S^2 \mathbf{v}_{01} + \delta_S^2 \mathbf{v}_{02} \qquad = a_{31} = \delta_S^2 \mathbf{v}_{07} + \delta_S^2 \mathbf{v}_{08} \tag{K.44}$$
$$a_{10} = \delta_D \mathbf{v}_{01} + \delta_D \mathbf{v}_{02} \qquad = a_{32} = \delta_D \mathbf{v}_{07} + \delta_D \mathbf{v}_{08} \tag{K.45}$$
$$a_{11} = \mathbf{v}_{03} \qquad = a_{33} = \mathbf{v}_{09} \tag{K.46}$$
$$a_{12} = \alpha_B \mathbf{v}_{03} \qquad = a_{34} = \alpha_B \mathbf{v}_{09} \tag{K.47}$$
$$a_{13} = \alpha_B^2 \mathbf{v}_{03} \qquad = a_{35} = \alpha_B^2 \mathbf{v}_{09} \tag{K.48}$$
$$a_{14} = \delta_D \mathbf{v}_{03} \qquad = a_{36} = \delta_D \mathbf{v}_{09} \tag{K.49}$$
$$a_{15} = \delta_D^2 \mathbf{v}_{03} \qquad = a_{37} = \delta_D^2 \mathbf{v}_{09} \tag{K.50}$$
$$a_{16} = \mathbf{v}_{04} + \mathbf{v}_{05} \qquad = a_{38} = \mathbf{v}_{10} + \mathbf{v}_{11} \tag{K.51}$$
$$a_{17} = \alpha_C \mathbf{v}_{04} + \alpha_D \mathbf{v}_{05} \qquad = a_{39} = \alpha_C \mathbf{v}_{10} + \alpha_D \mathbf{v}_{11} \tag{K.52}$$
$$a_{18} = \alpha_C^2 \mathbf{v}_{04} + \alpha_D^2 \mathbf{v}_{05} \qquad = a_{40} = \alpha_C^2 \mathbf{v}_{10} + \alpha_D^2 \mathbf{v}_{11} \tag{K.53}$$
$$a_{19} = \delta_S \mathbf{v}_{04} - \delta_S \mathbf{v}_{05} \qquad = a_{41} = \delta_S \mathbf{v}_{10} - \delta_S \mathbf{v}_{11} \tag{K.54}$$
$$a_{20} = \delta_S^2 \mathbf{v}_{04} + \delta_S^2 \mathbf{v}_{05} \qquad = a_{42} = \delta_S^2 \mathbf{v}_{10} + \delta_S^2 \mathbf{v}_{11} \tag{K.55}$$
$$a_{21} = \delta_D \mathbf{v}_{04} + \delta_D \mathbf{v}_{05} \qquad = a_{43} = \delta_D \mathbf{v}_{10} + \delta_D \mathbf{v}_{11} \tag{K.56}$$

$$\begin{bmatrix} \mathbf{F}_G^a \\ \mathbf{T}_G^a \end{bmatrix} = \frac{1}{2}\rho \begin{bmatrix} a_{00} & \dots & a_{21} \\ a_{22} & \dots & a_{43} \end{bmatrix} \boldsymbol{\theta} \tag{K.57}$$

Center of Mass Location in Fechner's Rigid Body Kite Model

The goal here is to find the relative positions of points B, C and D ($\mathbf{r}_B$, $\mathbf{r}_C$ and $\mathbf{r}_D$) with respect to the center of mass.

The position of the center of mass depends on the mass distribution over points A, B, C and D. The mass distribution should result in the same inertia tensor of for the kite, therefore the proposed mass distribution in [38] is invalid.

Originally, the y and z-position of point A (point 3 in Figure 4.3) are fixed. This leaves us with 7 unknowns. These are the x and z position of the center of mass, the masses of all points (4) and the x position of point 3.

The resulting inertia tensors must be identical. Since the inertia tensor is symmetric, this results in a set of four unique equations. Furthermore we know that $m_C = m_D$, and $m_k = m_A + m_B + m_C + m_D$. Finally, the location of the center of mass depends linearly on the locations of the other points: $p_O = m_A \mathrm{p}_A + m_B \mathrm{p}_B + m_C \mathrm{p}_C + m_D \mathrm{p}_D$ which leads to two more equations (only for the x and z coordinate, since the kite is assumed symmetric), resulting in a total of 8 equations and an over-constrained problem. Therefore and an additional free parameter is needed. Since the kite mass, height and width (Figure L.1) are properties that can be easily determined and have a direct physical meaning, these parameters remain fixed. For this reason z_A is chosen to be a free parameter, resulting in the following set of unknowns to be solved for:

$$x_O, z_O, m_A, m_B, m_C, m_D, x_A, z_A \tag{L.1}$$

The positions of the points B, C and D with respect to the center of mass are as follows:

$$\begin{aligned} \mathbf{r}_B &= \begin{bmatrix} -0.9107 & 0.0000 & -2.4626 \end{bmatrix}^T \\ \mathbf{r}_C &= \begin{bmatrix} -0.6564 & 4.1150 & 0.6571 \end{bmatrix}^T \\ \mathbf{r}_D &= \begin{bmatrix} -0.6564 & -4.1150 & 0.6571 \end{bmatrix}^T \end{aligned} \tag{L.2}$$

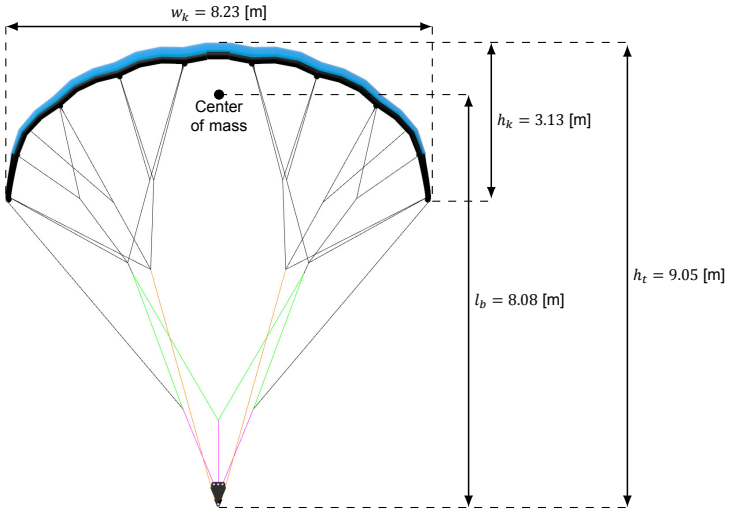

Figure L.1: Kite dimensions.

M

Rupperts Model Equations

This section describes how the matrix form of Rupperts' aerodynamic kite model is derived. From Equation 4.3 we can derive the following expression for the aerodynamic force and torque:

$$\mathbf{F}_G^a = 0.5\rho \mathbf{v}_a^2 A_{k,t} \left(C_a^L \mathbf{e}_G^L + C_a^D \mathbf{e}_G^D + C_a^S \mathbf{e}_G^S \right) \tag{M.1}$$

$$\mathbf{T}_G^a = 0.5\rho \mathbf{v}_a^2 A_{k,t} C_k^{z,T} b \left(C_k^{z,T} \mathbf{e}_G^{k,z} \right) \tag{M.2}$$

Recall from Equation 4.6 that we have the following expressions for the aerodynamic coefficients:

$$\begin{aligned} C_L^\alpha &= C_{L,0}^\alpha + C_{L,1}^\alpha \alpha + C_{L,2}^\alpha \alpha^2 + C_{L,3}^\alpha \alpha^3 \\ C_D^\alpha &= C_{D,0}^\alpha + C_{D,1}^\alpha \alpha + C_{D,2}^\alpha \alpha^2 + C_{D,3}^\alpha \alpha^3 \\ C_S^\beta &= \frac{A_{k,s}}{A_{k,p}} \left(\text{sgn}(\beta) C_{S,0}^\beta + C_{S,1}^\beta \beta + \text{sgn}(\beta) C_{S,2}^\beta \beta^2 + C_{S,3}^\beta \beta^3 \right) \\ C_k^{z,T} &= C_z^{\delta_s} \delta_s + C_z^\beta \beta + C_z^r \frac{br}{\|\mathbf{v}_a\|} \end{aligned} \tag{M.3}$$

From the above equations (Equation M.2 and Equation M.3) we can derive the following system of equations in matrix form:

$$\begin{aligned} \mathbf{F}_G^a &= \mathrm{M}_F \cdot \boldsymbol{\theta}_F \\ \mathbf{T}_G^a &= \mathrm{M}_T \cdot \boldsymbol{\theta}_T \end{aligned} \tag{M.4}$$

Where:

$$\begin{aligned} \mathrm{M}_F &= 0.5\rho \|\mathbf{v}_a\|^2 A_{k,p} \left[\mathbf{e}_G^L \quad \mathbf{e}_G^L \alpha \quad \mathbf{e}_G^L \alpha^2 \quad \mathbf{e}_G^D \alpha^3 \quad \mathbf{e}_G^D \quad \mathbf{e}_G^D \alpha \quad \mathbf{e}_G^D \alpha^2 \quad \mathbf{e}_G^D \alpha^3 + \quad \ldots \right. \\ &\quad \left. \frac{A_{k,s}}{A_{k,p}} \text{sgn}(\beta) \mathbf{e}_G^S \quad \frac{A_{k,s}}{A_{k,p}} \mathbf{e}_G^S \beta \quad \frac{A_{k,s}}{A_{k,p}} \text{sgn}(\beta) \mathbf{e}_G^S \beta^2 \quad \frac{A_{k,s}}{A_{k,p}} \mathbf{e}_G^S \beta^3 \right] \\ \boldsymbol{\theta}_F &= \left[C_{L,0}^\alpha \quad C_{L,1}^\alpha \quad C_{L,2}^\alpha \quad C_{L,3}^\alpha \quad C_{D,0}^\alpha \quad C_{D,1}^\alpha \quad C_{D,2}^\alpha \quad C_{D,3}^\alpha \quad C_{S,0}^\beta \quad C_{S,1}^\beta \quad C_{S,2}^\beta \quad C_{S,3}^\beta \right]^T \\ \mathrm{M}_T &= 0.5\rho \|\mathbf{v}_a\|^2 A_{k,t} b \left[\delta_s \quad \beta \quad \frac{br}{\|\mathbf{v}_a\|} \right] \\ \boldsymbol{\theta}_T &= \left[C_z^{\delta_s} \quad C_z^\beta \quad C_z^r \right]^T \end{aligned} \tag{M.5}$$

N

Additional System Identification Results

The tables in this appendix (N.1) show the statistics of the identified parameters for both kite models. The errors between the estimated and true aerodynamic coefficient curves are shown in Figure N.1.

Table N.1: Statistics of the parameters identified for Ruppert's model (left) and the modified model of Fechner (right).

Parameter	μ [-]	σ [-]
C_0^L	0.195	0.001
C_1^L	1.154	0.011
C_2^L	8.344	0.052
C_3^L	-14.426	0.081
C_0^D	0.100	0.001
C_1^D	-0.001	0.007
C_2^D	0.847	0.035
C_3^D	-0.070	0.054
C_0^S	0.000	0.000
C_1^S	-1.085	0.000
C_2^S	-8.672	0.000
C_3^S	14.938	0.001
$C_{n,0}$	0.075	0.002
$C_{n,1}$	0.077	0.001
$C_{n,2}$	-0.016	0.001

Parameter	μ [-]	σ [-]
$C_0^{L,t}$	-0.956	2.659
$C_1^{L,t}$	-5.164	0.704
$C_2^{L,t}$	14.843	1.460
$C_3^{L,t}$	0.160	0.129
$C_4^{L,t}$	-0.003	0.002
$C_0^{L,s}$	-0.016	0.013
$C_1^{L,s}$	-0.192	0.108
$C_2^{L,s}$	0.698	0.234
$C_3^{L,s}$	0.001	0.001
$C_4^{L,s}$	-0.000	0.000
$C_5^{L,s}$	0.001	0.000
$C_0^{D,t}$	6.955	7.017
$C_1^{D,t}$	0.823	0.725
$C_2^{D,t}$	-2.503	1.463
$C_3^{D,t}$	-0.306	0.334
$C_4^{D,t}$	0.003	0.004
$C_0^{D,s}$	-1.775	0.047
$C_1^{D,s}$	-1.316	0.016
$C_2^{D,s}$	-8.082	0.252
$C_3^{D,s}$	0.004	0.000
$C_4^{D,s}$	0.000	0.000
$C_5^{D,s}$	0.031	0.001

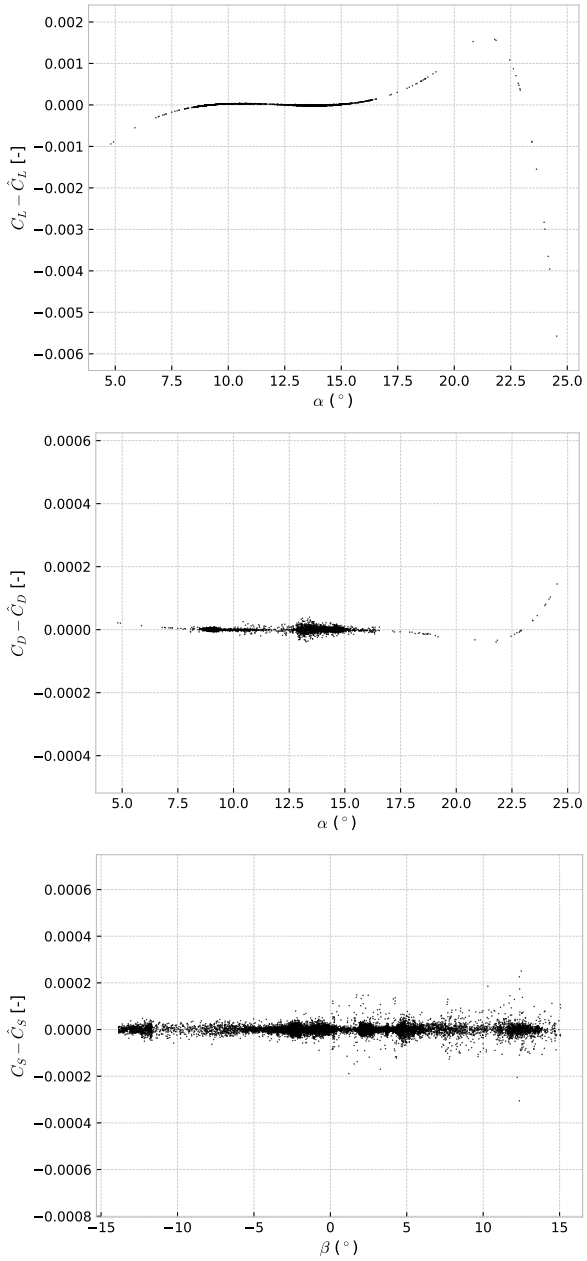

Figure N.1: Errors between the estimated and true curve for the lift, drag and side force coefficient. 1 out of 50 data points are shown.

Flight Path Suggestion for Kitepower

From the following figures it seems to be beneficial to use the side of the wind window for the retraction phase.

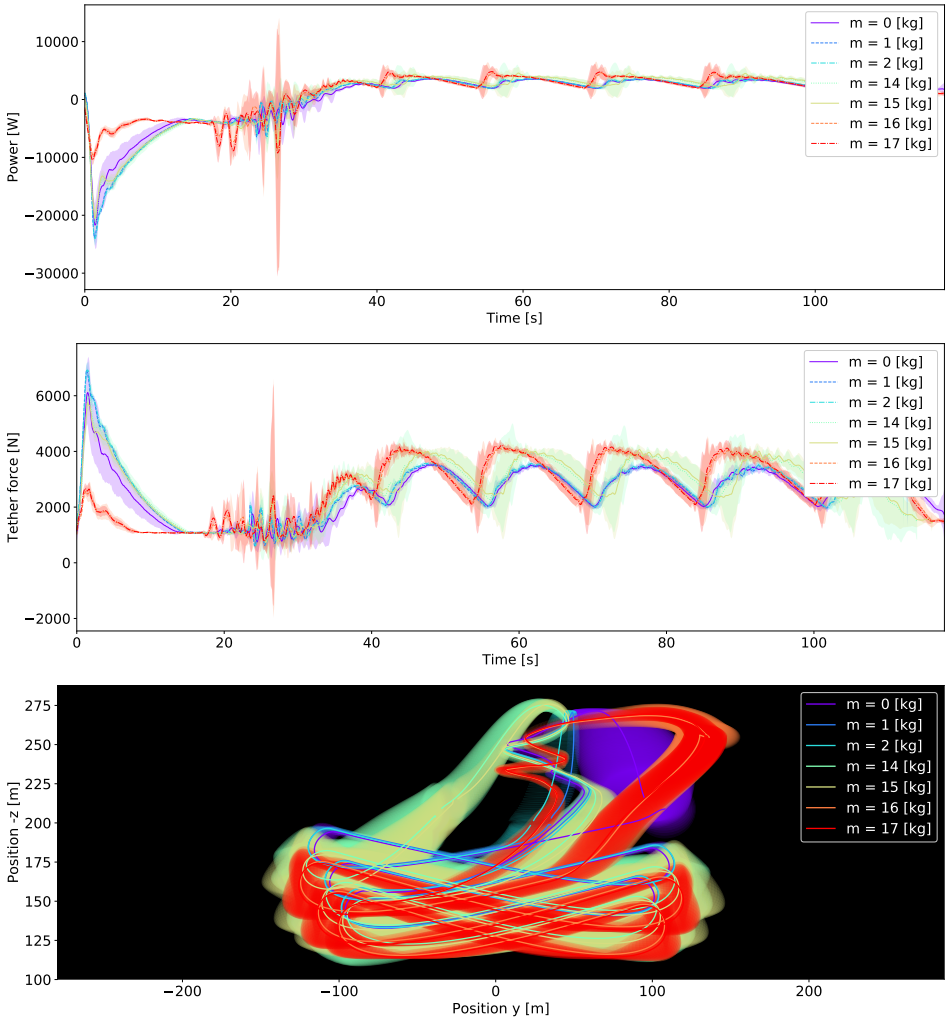

Figure O.1: Top to bottom: average cycle power, tether force and yz flight path for increasing KCU mass.

P

List of Experiments

Table P.1: Table with experiment parameters, filenames and duration.

Filename	v_w [m/s]	m_{KCU} [kg]	m_{kite} [kg]	$C_{D,KCU}$ [-]	$C_{D,tether}$ [-]	Duration [s]
mkcu_00_mkite_10.5_w_6_2019-09-04_11:29:12	6	0	10.5	0	0.96	1318.75
mkcu_02_mkite_10.5_w_6_2019-09-04_11:51:44	6	2	10.5	0	0.96	1320.35
mkcu_04_mkite_10.5_w_6_2019-09-04_12:14:28	6	4	10.5	0	0.96	1272.5
mkcu_06_mkite_10.5_w_6_2019-09-04_12:36:37	6	6	10.5	0	0.96	1300.0
mkcu_08_mkite_10.5_w_6_2019-09-04_13:02:52	6	8	10.5	0	0.96	1439.6
mkcu_8_mkite_10.5_w_6_2019-09-03_11:54:54	6	8	10.5	0	0.96	1284.85
mkcu_8_mkite_10.5_CD_0_w_6_2019-09-06_15:56:54	6	8	10.5	0	0.96	1269.0
mkcu_8_mkite_12.5_w_6_2019-09-03_12:17:13	6	8	12.5	0	0.96	1282.1
mkcu_8_mkite_18.5_w_6_2019-09-03_13:37:33	6	8	18.5	0	0.96	1316.9
mkcu_8_mkite_8.5_w_6_2019-09-03_11:33:28	6	8	8.5	0	0.96	1261.7
mkcu_8_mkite_14.5_w_6_2019-09-03_12:40:03	6	8	14.5	0	0.96	1300.0
mkcu_8_mkite_16.5_w_6_2019-09-03_13:06:52	6	8	16.5	0	0.96	1278.9
mkcu_8_mkite_2.5_w_6_2019-09-05_17:05:06	6	8	2.5	0	0.96	1268.9
mkcu_8_mkite_4.5_w_6_2019-09-03_10:40:35	6	8	4.5	0	0.96	1311.85
mkcu_8_mkite_6.5_w_6_2019-09-03_11:11:16	6	8	6.5	0	0.96	1284.25
mkcu_8_mkite_10.5_CD_0.5_w_6_2019-09-06_11:41:26	6	8	10.5	0.5	0.96	1270.0
mkcu_8_mkite_10.5_CD_1_w_6_2019-09-06_12:10:14	6	8	10.5	1	0.96	1273.45
mkcu_8_mkite_10.5_CD_1.5_w_6_2019-09-06_12:31:39	6	8	10.5	1.5	0.96	1260.3
mkcu_10_mkite_10.5_w_6_2019-09-04_13:27:48	6	10	10.5	0	0.96	1265.41
mkcu_12_mkite_10.5_w_6_2019-09-04_13:59:51	6	12	10.5	0	0.96	1261.25
mkcu_14_mkite_10.5_w_6_2019-09-04_14:21:44	6	14	10.5	0	0.96	1300.0
mkcu_16_mkite_10.5_w_6_2019-09-04_14:45:19	6	16	10.5	0	0.96	1362.95
mkcu_18_mkite_10.5_w_6_2019-09-06_10:05:54	6	18	10.5	0	0.96	1255.85
mkcu_20_mkite_10.5_w_6_2019-09-06_10:27:01	6	20	10.5	0	0.96	1271.75
mkcu_22_mkite_10.5_w_6_2019-09-06_10:48:31	6	22	10.5	0	0.96	1265.0
mkcu_26_mkite_10.5_w_6_2019-09-06_11:10:40	6	26	10.5	0	0.96	1307.35
mkcu_0_mkite_10.5_w_10_2019-09-03_21:07:49	10	0	10.5	0	0.96	1267.9
mkcu_2_mkite_10.5_w_10_2019-09-03_21:33:48	10	2	10.5	0	0.96	1300.0
mkcu_4_mkite_10.5_w_10_2019-09-03_22:02:24	10	4	10.5	0	0.96	1356.55
mkcu_6_mkite_10.5_w_10_2019-09-03_22:26:01	10	6	10.5	0	0.96	1267.15
mkcu_8_mkite_10.5_w_10_2019-09-03_18:48:03	10	8	10.5	0	0.96	1300.0
mkcu_8_mkite_10.5_w_10_2019-09-04_09:28:32	10	8	10.5	0	0.96	1356.55
mkcu_8_mkite_12.5_w_10_2019-09-03_19:23:51	10	8	12.5	0	0.96	1300.0
mkcu_8_mkite_10.5_CD_0_w_10_2019-09-06_15:33:24	10	8	10.5	0	0.96	1345.65
mkcu_8_mkite_14.5_w_10_2019-09-03_19:53:10	10	8	14.5	0	0.96	1277.5
mkcu_8_mkite_16.5_w_10_2019-09-03_20:15:23	10	8	16.5	0	0.96	1307.8
mkcu_8_mkite_18.5_w_10_2019-09-03_20:37:51	10	8	18.5	0	0.96	1258.35
mkcu_8_mkite_2.5_w_10_2019-09-05_17:38:58	10	8	2.5	0	0.96	1275.25
mkcu_8_mkite_20.5_w_10_2019-09-05_18:00:57	10	8	20.5	0	0.96	1292.3
mkcu_8_mkite_24.5_w_10_2019-09-05_18:23:05	10	8	24.5	0	0.96	1373.5
mkcu_8_mkite_28.5_w_10_2019-09-05_18:46:34	10	8	28.5	0	0.96	1318.9
mkcu_8_mkite_32.5_w_10_2019-09-05_19:09:29	10	8	32.5	0	0.96	1300.0
mkcu_8_mkite_4.5_w_10_2019-09-03_14:32:34	10	8	4.5	0	0.96	1264.95
mkcu_8_mkite_6.5_w_10_2019-09-03_14:54:04	10	8	6.5	0	0.96	1382.05
mkcu_8_mkite_8.5_w_10_2019-09-03_15:25:16	10	8	8.5	0	0.96	1322.15
mkcu_8_mkite_10.5_CD_0.5_w_10_2019-09-06_12:54:02	10	8	10.5	0.5	0.96	1253.55
mkcu_8_mkite_10.5_CD_1_w_10_2019-09-06_13:15:10	10	8	10.5	1	0.96	1295.65
mkcu_8_mkite_10.5_CD_1.5_w_10_2019-09-06_13:37:11	10	8	10.5	1.5	0.96	1391.95
mkcu_10_mkite_10.5_w_10_2019-09-04_09:52:12	10	10	10.5	0	0.96	1366.8
mkcu_12_mkite_10.5_w_10_2019-09-04_10:15:50	10	12	10.5	0	0.96	1290.6
mkcu_14_mkite_10.5_w_10_2019-09-04_10:38:01	10	14	10.5	0	0.96	1279.8
mkcu_16_mkite_10.5_w_10_2019-09-04_11:01:46	10	16	10.5	0	0.96	1300.0
mkcu_18_mkite_10.5_w_10_2019-09-05_21:01:16	10	18	10.5	0	0.96	1311.05
mkcu_20_mkite_10.5_w_10_2019-09-05_21:23:19	10	20	10.5	0	0.96	1280.35
mkcu_22_mkite_10.5_w_10_2019-09-05_21:44:56	10	22	10.5	0	0.96	1278.0
mkcu_26_mkite_10.5_w_10_2019-09-05_22:07:15	10	26	10.5	0	0.96	1300.0
mkcu_30_mkite_10.5_w_10_2019-09-05_22:37:21	10	30	10.5	0	0.96	1347.4
mkcu_34_mkite_10.5_w_10_2019-09-05_23:00:28	10	34	10.5	0	0.96	1263.6
mkcu_38_mkite_10.5_w_10_2019-09-05_23:22:24	10	38	10.5	0	0.96	1280.5
mkcu_42_mkite_10.5_w_10_2019-09-06_09:16:55	10	42	10.5	0	0.96	1265.35
mkcu_46_mkite_10.5_w_10_2019-09-06_09:39:01	10	46	10.5	0	0.96	1266.5

Bibliography

[1] Google Protobuf. URL https://developers.google.com/protocol-buffers/.

[2] ZeroMQ. URL https://zeromq.org/.

[3] Skysails on BBC charterers, 2011. URL https://www.skysails.info/fileadmin/user{_}upload/Presselounge/BBC{_}SkySails/010{_}BBC{_}SkySails{_}300dpi{_}rgb.jpg.

[4] C.M. Ablow and S. Schechter. Numerial Simulation of Undersea Cable Dynamics. *Ocean Engng*, 10(6):443–457, 1983.

[5] Uwe Ahrens, Moritz Diehl, and Roland Schmehl. *Airborne Wind Energy*. Green Energy and Technology. Springer Berlin Heidelberg, Berlin, Heidelberg, 2013 edition, 2013. ISBN 978-3-642-39964-0. doi: 10.1007/978-3-642-39965-7. URL http://www.springer.com/series/8059http://link.springer.com/10.1007/978-3-642-39965-7.

[6] Uwe Ahrens, Björn Pieper, and Clemens Töpfer. Combining kites and rail technology into a traction-based airborne wind energy plant. In Uwe Ahrens, Moritz Diehl, and Roland Schmehl, editors, *Green Energy and Technology*, chapter 25, pages 437–441. Springer-Verlag, Berlin, 2013. ISBN 978-3-642-39964-0. doi: 10.1007/978-3-642-39965-7_25.

[7] Christian Andersson, Claus Führer, and Johan Åkesson. Assimulo: A unified framework for ODE solvers. *Mathematics and Computers in Simulation*, 116:26–43, oct 2015. ISSN 03784754. doi: 10.1016/j.matcom.2015.04.007. URL https://linkinghub.elsevier.com/retrieve/pii/S0378475415000701.

[8] Joel Andersson, Joris Gillis, and Moritz Diehl. User Documentation for CasADi v3.4.4, 2018.

[9] Joel A E Andersson, Joris Gillis, Greg Horn, James B Rawlings, and Moritz Diehl. CasADi: a software framework for nonlinear optimization and optimal control. *Mathematical Programming Computation*, pages 1–36, jul 2018. ISSN 1867-2949. doi: 10.1007/s12532-018-0139-4. URL http://link.springer.com/10.1007/s12532-018-0139-4.

[10] Cristina L. Archer. An Introduction to Meteorology for Airborne Wind Energy. In Uwe Ahrens, Moritz Diehl, and Roland Schmehl, editors, *Airborne wind energy*, chapter 5, pages 81–94. Springer, Berlin, Heidelberg, Newark, United States, 2013. doi: 10.1007/978-3-642-39965-7_5. URL http://link.springer.com/10.1007/978-3-642-39965-7{_}5.

[11] I. Argatov and R. Silvennoinen. Energy conversion efficiency of the pumping kite wind generator. *Renewable Energy*, 2010. ISSN 09601481. doi: 10.1016/j.renene.2009.09.006.

[12] Robert McNeel & Associates. Rhino, 2019. URL https://www.rhino3d.com/download/Rhino/6.0/release.

[13] John H. Baajen. *Automatic trajectory tracking control of kites*. Master thesis, Delft University of Technology, 2011.

[14] J H Baayen. Modeling a kite on a variable length flexible tether. Technical Report January, 2011.

[15] Jorn H. Baayen. Vortexje - An Open-Source Panel Method for Co-Simulation. pages 1–12, 2012. ISSN 23346043. doi: 10.2298/YUJOR0701055H. URL http://arxiv.org/abs/1210.6956.

[16] Jorn H. Baayen and Wubbo J. Ockels. Tracking control with adaption of kites. 6(January 2011): 182–191, 2010. ISSN 17518644. doi: 10.1049/iet-cta.2011.0037. URL http://arxiv.org/abs/1011.0851.

[17] I.P. Bakker. *Kitepower ground station*. PhD thesis, Delft University of Technology, 2018.

[18] F. Bañuelos-Ruedas, C. Angeles-Camacho, and S. Rios-Marcuello. Analysis and validation of the methodology used in the extrapolation of wind speed data at different heights. *Renewable and Sustainable Energy Reviews*, 14(8):2383–2391, oct 2010. ISSN 13640321. doi: 10.1016/j.rser.2010.05.001. URL http://linkinghub.elsevier.com/retrieve/pii/S1364032110001309.

[19] Nedeleg Bigi, Alain Nême, Kostia Roncin, Jean-Baptiste Leroux, Guilhem Bles, Christian Jochum, and Yves Parlier. Analytical Tether Model for Static Kite Flight. In *Airborne Wind Energy II*, chapter 3, pages 57–78. 2018. ISBN 9789811019470. doi: 10.1007/978-981-10-1947-0_3. URL http://link.springer.com/10.1007/978-981-10-1947-0{_}3.

[20] H A Bosch. *Finite element analysis of a kite for power generation*. PhD thesis, 2012.

[21] J. Breukels. *An Engineering Methodology for Kite Design*. Phd thesis, Delft University of technology, 2011. URL http://resolver.tudelft.nl/uuid:cdece38a-1f13-47cc-b277-ed64fdda7cdf.

[22] J Breukels and W J Ockels. A multi-body dynamics approach to a cable simulation for kites, 2007.

[23] Antonello Cherubini, Andrea Papini, Rocco Vertechy, and Marco Fontana. Airborne Wind Energy Systems: A review of the technologies. *Renewable and Sustainable Energy Reviews*, 51: 1461–1476, nov 2015. ISSN 13640321. doi: 10.1016/j.rser.2015.07.053. URL https://linkinghub.elsevier.com/retrieve/pii/S1364032115007005.

[24] Antonello Cherubini, Rocco Vertechy, and Marco Fontana. Simplified model of offshore Airborne Wind Energy Converters. *Renewable Energy*, 2016. ISSN 18790682. doi: 10.1016/j.renene.2015.11.063.

[25] N J Cook. Designers guide to wind loading of building structures. Part 1.

[26] Erwin Coumans. Bullet physics simulation. In *ACM SIGGRAPH 2015 Courses*, page 7. ACM, 2015.

[27] George M. Dadd, Dominic A. Hudson, and R. A. Shenoi. Comparison of Two Kite Force Models with Experiment. *Journal of Aircraft*, 47(1):212–224, jan 2010. ISSN 0021-8669. doi: 10.2514/1.44738. URL http://arc.aiaa.org/doi/10.2514/1.44738.

[28] George M. Dadd, Dominic A. Hudson, and R.A. Shenoi. Determination of kite forces using three-dimensional flight trajectories for ship propulsion. *Renewable Energy*, 36(10):2667–2678, oct 2011. ISSN 09601481. doi: 10.1016/j.renene.2011.01.027. URL https://linkinghub.elsevier.com/retrieve/pii/S0960148111000498.

[29] S G C De Groot. *Modelling the Dynamics of an Arc-shaped Kite for Control Law Design*. PhD thesis, Delft University of Technology, 2010. URL https://repository.tudelft.nl/islandora/object/uuid{%}3A5f493a5d-da9c-457f-be28-799a63cb42d9.

[30] Asil Ethem Demir, Carel Verhoeff, Daan van der Wiel, Hanno Maljaars, Laura Uyttersprot, Leroy Siegers, Peter de Groote, Sille Kamoen, Stefan de Blok, and Wiereen Parag. The Kite Power System Simulator. Technical report, Faculty of Aerospace Engineering, Delft University of Technology, 2010.

[31] Moritz Diehl. *Real-Time Optimization for Large Scale Nonlinear Processes*. PhD thesis, Ruprecht-Karls-Universiy, 2001.

[32] Moritz Diehl, Hans Georg Bock, and Johannes P. Schlöder. A Real-Time Iteration Scheme for Nonlinear Optimization in Optimal Feedback Control. *SIAM Journal on Control and Optimization*, 43(5):1714–1736, jan 2005. ISSN 1095-7138. doi: 10.1137/S0363012902400713. URL http://ieeexplore.ieee.org/document/1583100/http://epubs.siam.org/doi/10.1137/S0363012902400713.

[33] Rick Driscoll and Meyer Nahon. Mathematical Modeling and Simulation of a Moored Buoy System. In *OCEANS 96 MTS/IEEE Conference Proceedings. The Coastal Ocean - Prospects for the 21st Century*, pages 517–523, Fort Lauderdale, Florida, 1996. IEEE. ISBN 0-7803-3519-8. doi: 10.1109/OCEANS.1996.572845. URL https://ieeexplore.ieee.org/document/572845.

[34] Michael Erhard and Hans Strauch. Control of towing kites for seagoing vessels. *IEEE Transactions on Control Systems Technology*, 21(5):1629–1640, sep 2013. ISSN 10636536. doi: 10.1109/TCST.2012.2221093. URL http://ieeexplore.ieee.org/document/6342904/.

[35] Michael Erhard, Greg Horn, and Moritz Diehl. A quaternion-based model for optimal control of an airborne wind energy system. *ZAMM - Journal of Applied Mathematics and Mechanics / Zeitschrift für Angewandte Mathematik und Mechanik*, 97(1):7–24, jan 2017. ISSN 00442267. doi: 10.1002/zamm.201500180. URL http://doi.wiley.com/10.1002/zamm.201500180.

[36] Lorenzo Fagiano. *Control of Tethered Airfoils for High-Altitude Wind Energy Generation*. Phd thesis, Politecnico di torino, 2009.

[37] U. Fechner and R. Schmehl. Flight path planning in a turbulent wind environment. *Green Energy and Technology*, (9789811019463), 2018. ISSN 0148-0227. doi: 10.1029/2009JC005844.

[38] Uwe Fechner, Rolf van der Vlugt, Edwin Schreuder, and Roland Schmehl. Dynamic model of a pumping kite power system. *Renewable Energy*, 83:705–716, 2015. ISSN 18790682. doi: 10.1016/j.renene.2015.04.028. URL http://dx.doi.org/10.1016/j.renene.2015.04.028.

[39] Allister Furey and Inman Harvey. Evolution of Neural Networks for Active Control of Tethered Airfoils. In *Advances in Artificial Life*, pages 746–755. Springer Berlin Heidelberg, Lisbon, Portugal, 2007. doi: 10.1007/978-3-540-74913-4_75. URL http://link.springer.com/10.1007/978-3-540-74913-4{_}75.

[40] M Gaunaa, P F P Carqueija, P-E E Réthoré, and N N Sørensen. A computationally efficient method for determining the aerodynamic performance of kites for wind energy applications. *EWEA 2011*, pages 2011–2011, 2011. URL http://orbit.dtu.dk/getResource?recordId=276109{&}objectId=1{&}versionId=4.

[41] J. S. Goela, N. Somu, R. Abedinzadeh, and R. Vijay Kumar. Wind loading effects on a catenary. *Journal of Wind Engineering and Industrial Aerodynamics*, 21(3):235–249, 1985. ISSN 01676105. doi: 10.1016/0167-6105(85)90038-8.

[42] Flavio Gohl and Rolf H Luchsinger. Simulation based wing design for kite power. In *Airborne Wind Energy*, pages 325–338. Springer, 2013.

[43] Flavo Gohl. *Towards Efficient Kites: Numerical study about aerodynamic efficiency, dynamic stability and controllability of kites*. PhD thesis, Swiss Federal Institute of Technology Zurich, 2011.

[44] Simon Greenwold. simong-particles, 2009. URL https://bitbucket.org/simong/simong-particles/src.

[45] S.G.C. De Groot, J. Breukels, R. Schmehl, and W.J. Ockels. Modeling Kite Flight Dynamics Using a Multibody Reduction Approach. *Journal of Guidance, Control, and Dynamics*, 34(6):1671–1682, 2011. ISSN 0731-5090. doi: 10.2514/1.52686. URL http://arc.aiaa.org/doi/10.2514/1.52686.

[46] Ernst Hairer and Gerhard Wanner. *Solving Ordinary Differential Equations II*, volume 14 of *Springer Series in Computational Mathematics*. Springer Berlin Heidelberg, Berlin, Heidelberg, second rev edition, 1996. ISBN 978-3-642-05220-0. doi: 10.1007/978-3-642-05221-7. URL http://link.springer.com/10.1007/978-3-642-05221-7.

[47] Alan C Hindmarsh, Peter N. Brown, Keith E. Grant, Steven L. Lee, Radu Serban, Dan E. Shumaker, and Carol S Woodward. SUNDIALS. *ACM Transactions on Mathematical Software*, 31(3):363–396, sep 2005. ISSN 00983500. doi: 10.1145/1089014.1089020. URL https://computation.llnl.gov/casc/sundials/main.htmlhttp://portal.acm.org/citation.cfm?doid=1089014.1089020.

[48] Sighard F. Hoerner. *Fluid-Dynamic Drag*. Sighard F. Hoerner, 1965.

[49] John D Holmes. *Wind loading of structures*. CRC press, 2015.

[50] Boris Hou and Moritz Diehl. Robustness and stability optimization of power generating kite systems in a periodic pumping mode. In *2010 IEEE International Conference on Control Applications*, pages 2172–2177, Yokohama, Japan, sep 2010. IEEE. ISBN 978-1-4244-5362-7. doi: 10.1109/CCA.2010.5611288. URL http://ieeexplore.ieee.org/document/5611288/.

[51] Boris Houska. *Robustness and Stability Optimization of Open-Loop Controlled Power Generating Kites*. PhD thesis, Ruprecht-Karls-Universität Heidelberg, 2007.

[52] Boris Houska and Moritz Diehl. Optimal Control of Towing Kites. In *Proceedings of the 45th IEEE Conference on Decision and Control*, number 3, pages 2693–2697. IEEE, 2006. ISBN 1-4244-0171-2. doi: 10.1109/CDC.2006.377210. URL http://ieeexplore.ieee.org/document/4177402/.

[53] Boris Houska and Moritz Diehl. Optimal control for power generating kites. In *2007 European Control Conference (ECC)*, pages 3560–3567, Kos, Greece, jul 2007. IEEE. ISBN 978-3-9524173-8-6. doi: 10.23919/ECC.2007.7068861. URL https://ieeexplore.ieee.org/document/7068861/.

[54] A. Ilzhöfer, B. Houska, and M. Diehl. Nonlinear MPC of kites under varying wind conditions for a new class of large-scale wind power generators. *International Journal of Robust and Nonlinear Control*, 17(17):1590–1599, nov 2007. ISSN 10498923. doi: 10.1002/rnc.1210. URL http://doi.wiley.com/10.1002/rnc.1210.

[55] Claudius Jehle. *Automatic Flight Control of Tethered Kites for Power Generation*. Master thesis, Technische Universität München, 2012.

[56] Claudius Jehle and Roland Schmehl. Applied Tracking Control for Kite Power Systems. *Journal of Guidance, Control, and Dynamics*, 37(4):1211–1222, 2014. ISSN 0731-5090. doi: 10.2514/1.62380. URL http://arc.aiaa.org/doi/10.2514/1.62380.

[57] Mustafa Can Karadayı. *Particle System Modelling and Dynamic Simulation of a Tethered Rigid Wing Kite for Power Generation*. PhD thesis, Delft University of Technology, 2016. URL http://resolver.tudelft.nl/uuid:d6a2fcf8-7fce-4eb8-857b-209b9faac755.

[58] Vladislav Klein and Eugene A. Morelli. *Aircraft System Identification: Theory and Practice*. American Institute of Aeronautics and Astronautics, Reston ,VA, jan 2006. ISBN 978-1-56347-832-1. doi: 10.2514/4.861505. URL http://arc.aiaa.org/doi/book/10.2514/4.861505.

[59] Gerhard Kramm, Gary Sellhorst, Hannah K. Ross, John Cooney, Ralph Dlugi, and Nicole Mölders. On the Maximum of Wind Power Efficiency. *Journal of Power and Energy Engineering*, 04(01):1–39, 2016. ISSN 2327-588X. doi: 10.4236/jpee.2016.41001. URL http://www.scirp.org/journal/doi.aspx?DOI=10.4236/jpee.2016.41001.

[60] Bas Lansdorp, Richard Ruiterkamp, Paul Williams, and Wubbo Ockels. Modeling, Simulation, and Testing of Surf Kites for Power Generation. In *AIAA Modeling and Simulation Technologies Conference and Exhibit*, Reston, Virigina, aug 2008. American Institute of Aeronautics and Astronautics. ISBN 978-1-62410-000-0. doi: 10.2514/6.2008-6693. URL http://arc.aiaa.org/doi/10.2514/6.2008-6693.

[61] Jeongseok Lee, Michael X Grey, Sehoon Ha, Tobias Kunz, Sumit Jain, Yuting Ye, Siddhartha S Srinivasa, Mike Stilman, and C Karen Liu. DART: Dynamic animation and robotics toolkit. *The Journal of Open Source Software*, 3(22):500, 2018.

[62] Rachel Leuthold. Java-Based Surf-Kite Flight Model for Application to a Kite-Surfing Simulator. Technical report, TU Delft, 2013.

[63] M.L. LOYD. Crosswind kite power (for large-scale wind power production). *Journal of Energy*, 4 (3):106–111, may 1980. ISSN 0146-0412. doi: 10.2514/3.48021. URL http://arc.aiaa.org/doi/10.2514/3.48021.

[64] Miles Macklin, Matthias Müller, Nuttapong Chentanez, and Tae-Yong Kim. Unified particle physics for real-time applications. *ACM Transactions on Graphics*, 33(4):1–12, jul 2014. ISSN 07300301. doi: 10.1145/2601097.2601152. URL http://dl.acm.org/citation.cfm?doid=2601097.2601152.

[65] Pierangelo Masarati, Marco Morandini, and Paolo Mantegazza. An efficient formulation for general-purpose multibody/multiphysics analysis. *Journal of Computational and Nonlinear Dynamics*, 9(4):41001, 2014.

[66] Gilbert M Masters. Renewable and Efficient Electric Power Systems. Technical report.

[67] MATLAB. version 9.5.0 (R2018b), 2018. URL https://nl.mathworks.com/.

[68] Milan Milutinović, Nenad Kranjčević, and Joško Deur. Multi-mass dynamic model of a variable-length tether used in a high altitude wind energy system. *Energy Conversion and Management*, 87:1141–1150, 2014. ISSN 01968904. doi: 10.1016/j.enconman.2014.04.013.

[69] J A Mulder, W H J J Van Staveren, J C Van Der Vaart, E De Weerdt, C C De Visser, A C In 't Veld, and E Mooij. Lecture Notes AE3202 Flight Dynamics, 2013.

[70] Matthias Müller, Bruno Heidelberger, Marcus Hennix, and John Ratcliff. Position based dynamics. *Journal of Visual Communication and Image Representation*, 18(2):109–118, apr 2007. ISSN 10473203. doi: 10.1016/j.jvcir.2007.01.005. URL http://linkinghub.elsevier.com/retrieve/pii/S1047320307000065.

[71] Peter Naaijen and Vincent Koster. Performance of auxiliary wind propulsion for merchant ships using a kite. In *2nd International Conference on Marine Research and Transportation*, pages 45–53, 2007. ISBN 0020868X (ISSN).

[72] M Noom. *Implementing a varying tether length into KiteSim, a JAVA-based kite power system simulator*. PhD thesis, Delft University of Technology, Delft, 2011.

[73] M.N. N Noom. *Theoretical Analysis of Mechanical Power Generation by Pumping Cycle Kite Power Systems*. PhD thesis, Delft University of Technology;, 2013. URL http://resolver.tudelft.nl/uuid:1c1a3e90-11e6-4fe7-8808-8c6a1227dadb.

[74] Nvidia. Flex. URL https://developer.nvidia.com/flex.

[75] Nvidia. NVIDIA PhysX SDK 4.1, 2018. URL https://github.com/NVIDIAGameWorks/PhysX.

[76] Wubbo J. Ockels. Laddermill, a novel concept to exploit the energy in the airspace. *Aircraft Design*, 4(2-3):81–97, jun 2001. ISSN 13698869. doi: 10.1016/S1369-8869(01)00002-7. URL http://linkinghub.elsevier.com/retrieve/pii/S1369886901000027.

[77] Johannes Oehler. *Measuring apparent flow vector on a flexible wing kite*. PhD thesis, University of Stuttgart, 2017.

[78] Johannes Oehler and Roland Schmehl. Aerodynamic characterization of a soft kite by in situ flow measurement. *Wind Energy Science*, 4(1):1–21, jan 2019. ISSN 2366-7451. doi: 10.5194/wes-4-1-2019. URL https://www.wind-energ-sci.net/4/1/2019/.

[79] Claudio Pedrazzi. Dog On Lead Minehhunting underwater cable simulation. In *12th European ADAMS Users' Conference*, Marburg, Germany, 1997.

[80] Faggiani Pietro. *Pumping Kites Wind Farm*. PhD thesis, Delft university of Technology, 2014. URL http://resolver.tudelft.nl/uuid:66cddbd2-5f50-4fc7-be0b-468853128f37.

[81] AR Podgaets and WJ Ockels. Problem of Pareto-optimal control for a high altitude energy system. *Proceedings of the 9th World Renweable Energy Congress, Florence, Italy*, (19 - 25 August):19–25, 2006. URL http://asset.lr.tudelft.nl/fileadmin/Faculteit/LR/Organisatie/Afdelingen{_}en{_}Leerstoelen/Afdeling{_}AEWE/Applied{_}Sustainable{_}Science{_}Engineering{_}and{_}Technology/Publications/doc/Laddermill{_}control{_}Alex.pdf.

[82] Benoit Python. *Methodology Improvement for Performance Assessment of Pumping Kite Power Wing*. PhD thesis, Ecole Polytechnique Federale de Lausanne, 2017.

[83] Moritz Diehl Rachel Leuthold, Jochem deSchutter, Elena Malz, Sebastien Gros. An Update on the AWEbox, 2017. URL https://www.syscop.de/files/users/Dang.doan/Leuthold{_}retreat{_}2017{_}AWEboxUpdate.pdf.

[84] M B Ruppert. *Development and validation of a real time pumping kite model*. PhD thesis, 2012. URL https://repository.tudelft.nl/islandora/object/uuid:56f1aef6-f337-4224-a44e-8314e9efbe83.

[85] G Sánchez-Arriaga, M. García-Villalba, and R Schmehl. Modeling and dynamics of a two-line kite. *Applied Mathematical Modelling*, 47:473–486, jul 2017. ISSN 0307904X. doi: 10.1016/j.apm.2017.03.030. URL https://linkinghub.elsevier.com/retrieve/pii/S0307904X17301798.

[86] Gonzalo Sanchez-Arriaga, A Pastor-Rodríguez, Manuel Sanjurjo-Rivo, and Roland Schmehl. A lagrangian flight simulator for airborne wind energy systems. *Applied Mathematical Modelling*, 2019. doi: 10.1016/j.apm.2018.12.016. URL https://www.researchgate.net/publication/323357689.

[87] C Santel and A Gäb. Numerical Simulation of Glider Winch Launches. *Technical Soaring*, 35(3):78–84, 2011. URL http://journals.sfu.ca/ts/index.php/ts/article/view/76.

[88] Roland Schmehl, editor. *Airborne Wind Energy*. Green Energy and Technology. Springer Singapore, Singapore, 2018. ISBN 978-981-10-1946-3. doi: 10.1007/978-981-10-1947-0. URL http://link.springer.com/10.1007/978-981-10-1947-0.

[89] L Schwab. Multibody Dynamics B. *Delft University of Technology, Delft, The Netherlands*, 1998.

[90] J.F.J.E.M Schwoll. *Finite Elements Analysis of Inflatable Structures Using Uniform Pressure*. PhD thesis, 2012.

[91] Russell Smith and Others. Open dynamics engine. 2005.

[92] MSC software. MSC Adams. URL http://www.mscsoftware.com/product/adams.

[93] J. Stevenson, K. Alexander, and P. Lynn. Kite performance testing by flying in a circle. *Aeronautical Journal*, 109(1096):269–276, 2005. ISSN 00019240. doi: 10.1017/S0001924000000725. URL http://www.scopus.com/inward/record.url?eid=2-s2.0-23144457848{&}partnerID=40{&}md5=8f533b22591acb8b10a3f605288e4a90.

[94] Alessandro Tasora, Radu Serban, Hammad Mazhar, Arman Pazouki, Daniel Melanz, Jonathan Fleischmann, Michael Taylor, Hiroyuki Sugiyama, and Dan Negrut. Chrono: An open source multi-physics dynamics engine. In *International Conference on High Performance Computing in Science and Engineering*, pages 19–49. Springer, 2015.

[95] E. J. Terink, J. Breukels, R. Schmehl, and W. J. Ockels. Flight Dynamics and Stability of a Tethered Inflatable Kiteplane. *Journal of Aircraft*, 48(2):503–513, 2011. ISSN 0021-8669. doi: 10.2514/1.C031108. URL http://arc.aiaa.org/doi/10.2514/1.C031108.

[96] R. van der Vlugt. *Aero- and Hydrodynamic Performance Analysis of a Speed Kiteboarder.* PhD thesis, 2009. URL https://repository.tudelft.nl/islandora/object/uuid:9e0c7a62-149c-4fab-8d27-afe15c1a8795?collection=education.

[97] Rolf van der Vlugt, Anna Bley, Michael Noom, and Roland Schmehl. Quasi-steady model of a pumping kite power system. *Renewable Energy*, 131:83–99, 2019. ISSN 18790682. doi: 10.1016/j.renene.2018.07.023.

[98] Jelte van Til, Marcelo De Lellis, Ramiro Saraiva, and Alexandre Trofino. Dynamic model of a C-shaped bridled kite using a few rigid plates. *Green Energy and Technology*, (9789811019463): 99–115, 2018. ISSN 18653537. doi: 10.1007/978-981-10-1947-0_5.

[99] Loup Verlet. Computer "Experiments" on Classical Fluids. I. Thermodynamical Properties of Lennard-Jones Molecules. *Journal of Physics D: Applied Physics*, 159 (1):98–103, jul 1967. ISSN 0031-899X. doi: 10.1103/PhysRev.159.98. URL https://link.aps.org/doi/10.1103/PhysRev.159.98https://journals.aps.org/pr/abstract/10.1103/PhysRev.159.98.

[100] Colonel Viney and George Pocock. Patent Charvolant. In *Arcana of science and art, or, An annual register of useful inventions and improvements, discoveries and new facts, in mechanics, chemistry, natural history, and social economy.*, chapter Mechanical, page 28. J. Limbird, London, 3 edition, 1828. URL https://hdl.handle.net/2027/umn.31951000744420y.

[101] Paul Williams. Optimal Wind Power Extraction with a Tethered Kite. In *AIAA Guidance, Navigation, and Control Conference and Exhibit*, number August, Reston, Virigina, aug 2006. American Institute of Aeronautics and Astronautics. ISBN 978-1-62410-046-8. doi: 10.2514/6.2006-6193. URL http://arc.aiaa.org/doi/10.2514/6.2006-6193.

[102] Paul Williams. Dynamic multibody modeling for tethered space elevators. *Acta Astronautica*, 65(3-4):399–422, aug 2009. ISSN 00945765. doi: 10.1016/j.actaastro.2008.11.016. URL http://dx.doi.org/10.1016/j.actaastro.2008.11.016https://linkinghub.elsevier.com/retrieve/pii/S0094576509001209.

[103] Paul Williams. Cable Modeling Approximations for Rapid Simulation. *Journal of Guidance, Control, and Dynamics*, 40(7):1779–1788, jul 2017. ISSN 0731-5090. doi: 10.2514/1.G002354. URL https://arc.aiaa.org/doi/10.2514/1.G002354.

[104] Paul Williams, Peter Lapthorne, and Pavel Trivailo. Circularly-Towed Lumped Mass Cable Model Validation from Experimental Data. *AIAA Modeling and Simulation Technologies Conference and Exhibit*, (August):1–29, 2006. doi: 10.2514/6.2006-6817.

[105] Paul Williams, Bas Lansdorp, and Wubbo Ockels. Flexible Tethered Kite with Moveable Attachment Points, Part I: Dynamics and Control. In *AIAA Atmospheric Flight Mechanics Conference and Exhibit*, Reston, Virigina, aug 2007. American Institute of Aeronautics and Astronautics. ISBN 978-1-62410-131-1. doi: 10.2514/6.2007-6628. URL http://arc.aiaa.org/doi/10.2514/6.2007-6628.

[106] Paul Williams, Bas Lansdorp, and Wubbo Ockels. Flexible Tethered Kite with Moveable Attachment Points, Part II: State and Wind Estimation. *Aerospace*, 2007. ISSN 07315090. doi: 10.2514/6.2007-6629.

[107] Paul Williams, Bas Lansdorp, and Wuboo Ockels. Modeling and Control of a Kite on a Variable Length Flexible Inelastic Tether. In *AIAA Modeling and Simulation Technologies Conference and Exhibit*, Hilton Head, South Carolina, US, 2007. AIAA. ISBN 978-1-62410-160-1. doi: 10.2514/6.2007-6705. URL http://arc.aiaa.org/doi/10.2514/6.2007-6705.

[108] Paul Williams, Bas Lansdorp, and Wubbo Ockels. Nonlinear Control and Estimation of a Tethered Kite in Changing Wind Conditions. *Journal of Guidance, Control, and Dynamics*, 31(3):793–799, may 2008. ISSN 0731-5090. doi: 10.2514/1.31604. URL http://arc.aiaa.org/doi/10.2514/1.31604.

[109] Paul Williams, Bas Lansdorp, and Wubbo Ockesl. Optimal Crosswind Towing and Power Generation with Tethered Kites. *Journal of Guidance, Control, and Dynamics*, 31(1):81–93, 2008. ISSN 0731-5090. doi: 10.2514/1.30089. URL http://arc.aiaa.org/doi/10.2514/1.30089.

[110] Xgerrmann and Lukehb. Reeling by element removal example. URL https://github.com/NVIDIAGameWorks/PhysX/issues/69.